The Dissertation Committee for Hojeong Kim
certifies that this is the approved version of the following dissertation:

Measurement of $|V_{ub}|$ using Inclusing Semileptonic B Meson Decays

Committee:

Roy F. Schwitters, Supervisor

Duane A. Dicus

Gerald W. Hoffman

Sacha Kopp

Charles Radin

Measurement of $|V_{ub}|$ using Inclusing Semileptonic B Meson Decays

by

Hojeong Kim, B.S.

DISSERTATION

Presented to the Faculty of the Graduate School of

The University of Texas at Austin

in Partial Fulfillment

of the Requirements

for the Degree of

DOCTOR OF PHILOSOPHY

THE UNIVERSITY OF TEXAS AT AUSTIN

December 2004

Dedicated to my parents.

Acknowledgments

First of all, I thank my supervisor Roy F. Schwitters for accepting me as his student and giving me good opportunities. I learned not only physics but also the way a physicist should be from him. I also would like to thank Reinhard Eckmann for teaching me a lot about High Energy Physics. I learned all the details of doing analysis from him.

I send many thanks to my officemates and tennis-mates; Joerg Stelzer, Nicolas Berger, Tatiana H'rynova and Erkcan Ozcan. My life at SLAC was so much fun because of them. I thank Rafe Schindler for letting me share the office with great officemates.

I thank Denis Dujmic, Johannes Bauer and Asish Satpathy for reading this thesis. I also thank many other people at SLAC including Vera Luth, Peter Kim, Judy Meo, Melodi Masaniai, Jong and Sandy Yi.

I also would like to thank Kendall Reeves, Norma Kotz, Linda Hollidy and Carol Noriega for their kindness and help.

I would like to thank my old friends who gave me energy by just thinking about the time we spent together; everybody from KUPHY93, Shin Dongcheol, Lee Taehee, Lee Seungwon, Roh Younjung and Yoon Eunhee.

I send special thanks to my best friend ever, Todd E. Tilma. Many thanks go to his parents Ted and Melanie Tilma. They gave me a great moral

support.

I thank my brother Kim Heedong. I am so proud of him. Just hope he quits smoking soon which I believe is the only flaw of him.

For the last, I thank my parents for their support. Before I realized how hard it was for parents to send their child to a far away foreign country for such a long time, I took their support for granted. In addition, they've always been the best role model for me as a responsible and upstanding citizen. This dissertation is dedicated to them.

Measurement of $|V_{ub}|$ using Inclusing Semileptonic B Meson Decays

Publication No. _____

Hojeong Kim, Ph.D.
The University of Texas at Austin, 2004

Supervisor: Roy F. Schwitters

This dissertation presents a measuremeunt of the CKM matrix element $|V_{ub}|$ made with a sample of 64 million $B\overline{B}$ events collected with the *BABAR* detector. Using Heavy Quark theory, we combine the observed yield of leptons from semileptonic B decay in the electron energy interval 2.1–2.6 GeV with a recent CLEO measurement of the $B \to X_s\gamma$ photon spectrum to find $|V_{ub}|$ $=(4.25\pm0.35\pm0.45\pm0.20)\times10^{-3}$, where the first uncertainty is experimental and the last two are from theory.

Table of Contents

List of Tables

List of Figures

Chapter 1

Introduction

This dissertation presents a measurement of the magnitude of Cabibbo-Kobayashi-Maskawa (CKM) matrix [1] element $|V_{ub}|$ using inclusive semileptonic B decay from data taken at the *BABAR* experiment. We measure electron energy spectrum of $B \to X_u e\nu$ decay to calculate the partial branching fraction $\Delta\mathcal{B}(B \to X_u e\nu)$ for a lower energy cut of 2.1 GeV. We calculate the total branching fraction $\mathcal{B}(B \to X_u e\nu)$ using theory [2] and $b \to s\gamma$ photon spectrum [3] and determine $|V_{ub}|$.

In the following sections, brief reviews over theoretical background on the CKM matrix, other $|V_{ub}|$ measurements and motivation of this analysis are given.

1.1 The Standard Model and the Cabibbo-Kobayashi-Maskawa matrix

There are four fundamental recognized forces in nature: the weak, the strong, the electromagnetic and the gravitational forces. Experimental and theoretical work has led us to the formulation of a theory that describes all the known particles in nature and three of the four fundamental forces, except

gravity. This theory is called the Standard Model (SM) [4, 5].

According to this model, all matter is built from fundamental fermions; the three lepton generations,

$$\begin{pmatrix} e \\ \nu_e \end{pmatrix}, \quad \begin{pmatrix} \mu \\ \nu_\mu \end{pmatrix}, \quad \begin{pmatrix} \tau \\ \nu_\tau \end{pmatrix}, \tag{1.1}$$

and the three quark generations,

$$\begin{pmatrix} u \\ d \end{pmatrix}, \quad \begin{pmatrix} c \\ s \end{pmatrix}, \quad \begin{pmatrix} t \\ b \end{pmatrix}. \tag{1.2}$$

In lepton generations, weak interactions only within a particular generation coupling to W boson have been observed: i.e. $e^- \to \nu_e + W^-$, $\mu^- \to \nu_\mu + W^-$ etc. However in quark generations, cross-generational interactions have been observed: i.e. $d \to u + W^-$ (the β decay), $s \to u + W^-$ (in the decay $\Lambda \to p + e + \nu_e$).

In 1963, when u, d, s were the only known quarks, Cabibbo introduced the idea that the weak eigenstates of d and s quarks are mixtures of their mass eigenstates through the mixing angle θ_c known as the Cabibbo angle [1]:

$$\begin{pmatrix} d' \\ s' \end{pmatrix} = \begin{pmatrix} \cos\theta_c & \sin\theta_c \\ -\sin\theta_c & \cos\theta_c \end{pmatrix} \begin{pmatrix} d \\ s \end{pmatrix}, \tag{1.3}$$

where the doublet (d', s') is the weak eigenstate and (d, s) is the mass eigenstate [1]. This theory predicted many of the light hadron decays but had a major flaw; it allowed strangeness-changing neutral currents at a much higher rate than observed.

[1]The origin of the Cabibbo angle is not explained in the Standard Model

To solve this problem, Glashow, Iliopoulos and Maiani (GIM) incorporated the charm quark [2] into the hadronic weak current originally proposed by Cabibbo. The weak charged current in the GIM model is [6]:

$$\mathbf{J}_{\alpha}^{CC} = \frac{g}{\sqrt{2}} \begin{pmatrix} \overline{u} & \overline{c} \end{pmatrix} \gamma_{\alpha} \begin{pmatrix} d' \\ s' \end{pmatrix}, \tag{1.4}$$

where g is a coupling constant and γ_{α} are the Dirac matrices.

The GIM mechanism faced a trouble when *CP* violation was observed in certain decays of neutral kaons in 1964 [7]. The *CP* violation could not be explained in the GIM mechanism. To solve this problem, Kobayashi and Maskawa (KM) introduced a third weak isospin quark doublet in 1973. The weak charged current in KM model is extended to include two additional quarks b and t:

$$\mathbf{J}_{\alpha}^{CC} = \frac{g}{\sqrt{2}} \begin{pmatrix} \overline{u} & \overline{c} & \overline{t} \end{pmatrix} \gamma_{\alpha} V \begin{pmatrix} d \\ s \\ b \end{pmatrix}, \tag{1.5}$$

V is the unitary Cabibbo-Kobayashi-Maskawa (CKM) matrix:

$$V = \begin{pmatrix} V_{ud} & V_{us} & V_{ub} \\ V_{cd} & V_{cs} & V_{cb} \\ V_{td} & V_{ts} & V_{tb}, \end{pmatrix} \tag{1.6}$$

containing three real parameters and a phase factor $e^{i\delta}$.

The CKM matrix can be expressed in terms of four Wolfenstein parameters (λ, A, ρ, η) [8]:

$$V = \begin{pmatrix} 1 - \frac{\lambda^2}{2} & \lambda & A\lambda^3(\rho - i\eta) \\ -\lambda & 1 - \frac{\lambda^2}{2} & A\lambda^2 \\ A\lambda^3(1 - \rho - i\eta) & -A\lambda^2 & 1 \end{pmatrix} + \mathcal{O}(\lambda^4). \tag{1.7}$$

[2]The charm quark was discovered four years later

$\lambda = \sin\theta_c = 0.2205 \pm 0.0018$ is measured from the strangeness changing decays [9], $A = 0.80 \pm 0.08$ is measured from the decays of $b \to c$ with measured λ, and $\sqrt{\rho^2 + \eta^2} = 0.5 \pm 0.2$ is measured from the high momentum lepton spectrum in $B \to l\nu X$. The unitarity of the CKM matrix requires the following conditions to be fulfilled:

$$VV^\dagger = 1 \qquad \to \qquad \sum_i V_{\alpha i} V^*_{\beta i} = 0. \tag{1.8}$$

These relations can be geometrically represented in the complex plane as a triangle called the unitarity triangle. One of the unitarity relations

$$V_{ud}V^*_{ub} + V_{cd}V^*_{cb} + V_{td}V^*_{tb} = 0 \tag{1.9}$$

shown in Fig. 1.1 (a), is of particular interest, because it has three sides of the same order. This triangle can be rescaled by (i) choosing a phase convention such that $(V_{cd}V^*_{cb})$ is real, and (ii) dividing the lengths of all sides by $|V_{cd}V^*_{cb}|$; (i) aligns one side of the triangle with the real axis, and (ii) makes the length of this side 1. The scaled unitarity triangle is shown in Fig. 1.1 (b). Two vertices of the rescaled unitarity triangle are thus fixed at $(0, 0)$ and $(1, 0)$. The coordinates of the remaining vertex are denoted by $(\bar{\rho}, \bar{\eta})$:

$$\bar{\rho} = \rho(1 - \lambda^2/2), \quad \bar{\eta} = \eta(1 - \lambda^2/2). \tag{1.10}$$

Precise measurements of all CKM matrix elements and their relative phases are important tests of the Standard Model.

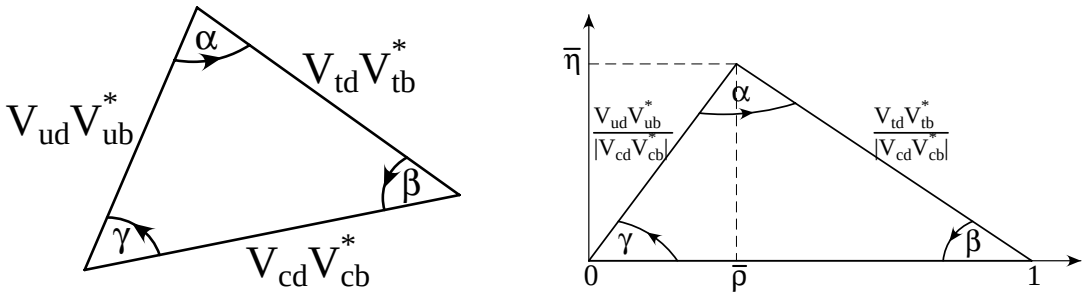

(a) (b)

Figure 1.1: (a) The unitary triangle. (b) The rescaled unitary triangle, all sides divided by $|V_{cd}V_{cb}^*|$.

1.2 The CKM matrix element V_{ub}

Among the CKM matrix elements, $|V_{ub}|$ is one of the least understood and constrained elements. The charmless semileptonic decay channel $B \to X_u e\nu$ provides the theoretically cleanest path for the determination of $|V_{ub}|$. However, this method has experimental challenges.

The main experimental challenge is the large background from $B \to X_c e\nu$ decay, which has a rate about 60 times higher than that for charmless semileptonic decay. The electron energy spectra of both decays from Monte Carlo samples are shown in Fig. 1.2. The charmless decay spectrum is scaled up by factor 10 for easier view. Kinematically the energy of electrons from $B \to X_c e\nu$ decays can be as big as 2.3 GeV ($E_l^* \sim (M_B^2 - M_D^2)/(2M_B)$ [3]) while electrons from $B \to X_u e\nu$ may have energies up to 2.6 GeV. This gives a narrow interval of about 300 MeV where the electrons are only from $B \to$

[3] E_l^* is the electron energy in the B meson rest frame, M_B and M_D are masses of B and D mesons, respectively.

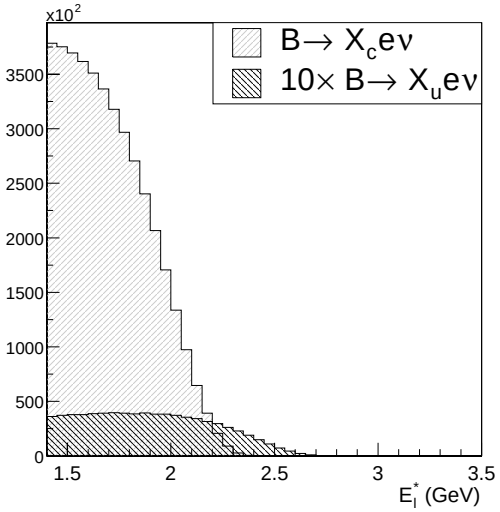

Figure 1.2: The $B \to X_c e\nu$ decay distribution and scaled electron energy spectrum from $B \to X_u e\nu$ decay by factor 10. These are from Monte Carlo samples.

$X_u e\nu$ decays. This is where the charmless electron energy spectrum can be measured with small experimental uncertainties, but covers about 10% of the total $B \to X_u e\nu$ decays.

The challenge in theory is that calculating the charmless electron energy spectrum at meson level ($B \to X_u e\nu$) is more difficult than at the parton level ($b \to ue\nu$), especially near the kinematic limit. The reason is that meson decay processes depend on the b quark's motion inside the B meson. This is why it is an important task for experimentalists to measure the charmless semileptonic electron energy spectrum to as low energy range as possible.

There have been many measurements of $|V_{ub}|$ using the inclusive semileptonic B decays. They are summarized in Table 1.1 [10]. Only those measurements which can be directly comparable to this analysis (and to each other)

Collaboration	$\|V_{ub}\|$ (10^{-3})	Method
CLEO [11]	4.11±0.13±0.31±0.46±0.28	$2.2 < E_l^* < 2.6$
BABAR [12]	4.31±0.20±0.20±0.49±0.30	$2.3 < E_l^* < 2.6$
Belle [13]	3.99±0.17±0.16±0.45±0.27	$2.3 < E_l^* < 2.6$
Belle [14]	4.63±0.28±0.39±0.48±0.32	$M_X < 1.7, q^2 > 8$
BABAR [15]	4.79±0.29±0.28±0.60±0.33	$M_X < 1.55$

Table 1.1: Summary of inclusive $|V_{ub}|$ measurements. The errors are from the statistical, systematic, E_γ-based rate fraction and Γ_{tot} uncertainties. Only those measurements can be directly comparable are shown here. Some are not because they have not been evaluated with identical theoretical inputs.

are shown in the table. Some results not shown in the table can not be directly comparable because they have not been evaluated with identical theoretical inputs [10].

The first three entries in Table 1.1 are measurements of the $b \to ue\nu$ rate near the endpoint ($E_l^* \sim (M_B^2 - M_D^2)/(2M_B)$) by the CLEO, *BABAR* and Belle Collaborations, respectively. The next entry is the measurement at the low M_X region with a dilepton mass (q) cut by the Belle Collaboration. M_X is the invariant mass of the hadrons accompanying the leptons [16]. The last entry is the measurement at the low M_X region by the *BABAR* Collaboration.

This analysis uses charged kaons to tag D mesons and thus to tag $b \to c$ decays[4]. This method has never tried in the $|V_{ub}|$ measurement. We require at least one high energy electron in each event. The high energy electron indicates there is semileptonic B meson in the event.

We measure electron energy spectrum as a function of number of recon-

[4] $b \to c$ decays are $B \to D$, D^*, D^{**}. And D^* and D^{**} go to D 100%.

structed kaons in each event. Since kaons can come from both the semileptonic B meson and the second B meson in each event, the kaons from the second B meson should be removed. With inputs from the Monte Carlo samples, we obtain the electron energy spectrum as a function of generated kaons from the semileptonic B mesons. This spectrum allows us to measure $B \to X_u e\nu$ electron energy spectrum and the partial branching fraction. With theoretical input [2] and $b \to s\gamma$ photon spectrum [3], the ratio between partial and total branching fractions is provided [17]. The total branching fractions allow us to extract $|V_{ub}|$ with measured b quark mass and lifetime.

The detailed discussion on the analysis can be found in Chapter 5.

1.3 Outline of this Dissertation

Apart from this introduction, the dissertation contains 6 more chapters:

- Chapter 2 is about the theoretical background on the charmless semileptonic B decays.
- Chapter 3 is an overview over the *BABAR* experiment. It introduces the PEP-II storage ring and the *BABAR* detector.
- Chapter 4 describes the data and Monte Carlo samples used in the analysis. The event selection criteria are also discussed here.
- Chapter 5 describes the analysis. It includes the electron and kaon selection criteria, the continuum background subtraction, the measurement of

the semileptonic electron energy spectra, the measurement of the charmless semileptonic B decays, taking of the partial and total branching fractions of $B \to X_u e\nu$ decays, extraction of $|V_{ub}|$ and systematic error study.

- Chapter 6 gives a summary of the results.

Chapter 2

Theory

2.1 The Heavy Quark Expansion

One of the theoretical methods to study hadronic B physics is effective field theories. They derive their predictive power by systematically exploiting a small expansion parameter. Effective field theories are based on the idea that in a given process only certain degrees of freedom may be important for understanding the physics. In particular, it is often the case that kinematical considerations that restrict the momenta of external particles effectively restrict the momenta of virtual particles as well. Thus it is sensible to remove from the theory intermediate states of high virtuality. Their absence may be compensated by introducing new "effective" interactions between the degrees of freedom which remain. Effective field theories are often constructed using the technique of the operator product expansion (OPE), which enables one to identify the physics at a given scale and to separate it out explicitly. OPE is used in conjunction with the renormalization group.

The heavy quark expansion (HQE) is one of effective field theories. It is characterized by virtualities $\mu \leq m_b$. Since the b quark is real and the B carries a nonzero b-number which persists in the asymptotic state, it is not

appropriate to integrate out the b and removing it from the theory entirely. Rather, when bound into a hadron with light degrees of freedom of typical energies $E \approx \Lambda_{\rm QCD}$, the b makes excursions from its mass shell by virtualities only of order $\Lambda_{\rm QCD}$. What can be integrated out is not the b itself, but rather those parts of the b field which take it far off shell. The result will be an effective theory of a static b quark in its rest frame.

Processes with hard virtual gluons, which drive the b far off shell, will lead to perturbative corrections in the effective theory of order $\alpha_s\ (m_b)$. In addition, power corrections which will lead to terms of order $(\Lambda_{\rm QCD}/m_b)^n$ appear. The appearance of the scale $\Lambda_{\rm QCD}$ reminds that these corrections involve non perturbative physics and will typically not be calculable from first principles. Instead, the inclusion of power corrections will require the introduction of new phenomenological parameters, whose values are controlled by non perturbative quantum chromodynamics (QCD).

2.2 Heavy Quark Effective Theory

Let us consider a hadron composed of a heavy quark Q and light degrees of freedom consisting of quarks, anti-quarks and gluons, in the limit $m_Q \to \infty$. Since the Compton wavelength of the heavy-quark is a lot smaller than that of light degrees of freedom, the light degrees of freedom cannot resolve features of the heavy quark other than its conserved gauge quantum numbers [18, 19]. In this limit, Q acts as a static source of electric and chromoelectric field. This is called the Heavy Quark Symmetry (HQS).

It is useful to make HQS manifest within QCD by taking the limit $m_b \to \infty$ of the QCD Lagrangian. This is done by making the dependence of all quantities on m_b explicit, and then developing the Lagrangian in a series in inverse powers of m_b. The idea is to write the Lagrangian in a form in which the action of the HQS is well-defined at each order in the expansion, so the effect of symmetry breaking corrections can be studied in a systematic way. The resulting Lagrangian is known as the Heavy Quark Effective Theory (HQET) [20, 21]. The HQET is similar to an effective theory which results from an OPE, in the sense that the only virtualities p which are allowed satisfy $p \ll m_b$, with effects of greater virtuality absorbed into the coefficients of higher dimension operators. The difference is that in this case, the heavy b quark is not explicitly removed from the effective theory.

In inclusive B decays, it is useful to observe that the energy released into the final state by the decay of the heavy b quark is large compared to the QCD scale. Hence the final hadronic state needs not be dominated by a few sharp resonances. If resonances are indeed unimportant, then there is a factorization between the short-distance part of the decay (the disappearance of the b quark) and the long-distance part (the eventual hadronization of the decay products). This factorization implies that for sufficiently inclusive quantities it is enough to consider the short-distance part of the process, with the subsequent hadronization taking place with unit probability. This factorization is known as parton-hadron duality [22]. It must hold as $m_b \to \infty$ with all other masses held fixed. In this limit, wavelengths associated with the

b quark decay are arbitrarily short and cannot interfere coherently with the hadronization process.

2.3 Inclusive Semileptonic B Decays

The calculation of the decay rate of semileptonic B decays begins with the effective Hamiltonian:

$$H_{eff} = \frac{-4G_F}{\sqrt{2}} V_{ub}(\bar{u}\gamma_\mu(1-\gamma_5)b)(\bar{l}\gamma^\mu(1-\gamma_5)\nu_l) \tag{2.1}$$

$$= \frac{-4G_F}{\sqrt{2}} V_{ub} J_\mu J_l^\mu, \tag{2.2}$$

obtained by integrating out the W bosons. The differential decay distribution can then be written as the product of leptonic and hadronic tensors,

$$d\Gamma \propto |V_{ub}|^2 L^{\alpha\beta} W_{\alpha\beta}. \tag{2.3}$$

Using the Optical Theorem[1], the hadronic tensor $W_{\alpha\beta}$ can be related to the imaginary part of the time ordered product of currents

$$W_{\alpha\beta} = -\frac{1}{\pi}\Im T_{\alpha\beta}, \tag{2.4}$$

$$T_{\alpha\beta} = -\frac{i}{2M_B}\int d^4x e^{-iq\cdot x} < B|T(J_\alpha^\dagger(x)J_\beta(0))|B > . \tag{2.5}$$

The time ordered product can be calculated by expanding in an OPE.

Then the lepton energy spectrum is given as [2]:

$$\frac{d\Gamma}{dx} = \frac{G_F^2|V_{ub}|^2 {m_b}^5}{192\pi^3} 2x^2(3-2x)\left(1 - \frac{C_F\alpha_s}{2\pi}G(x)\right), \tag{2.6}$$

[1]The method discussed in the following paragraphs was introduced in [23, 24].

where x is the energy of the charged lepton in the B meson rest frame ($x = 2E_l/m_b$, $0 \leq x \leq 1$), and

$$G(x) = \ln^2(1-x) + 2L_2(x) + \frac{2\pi^2}{3} + \frac{82 - 153x + 86x^2}{12x(3-2x)} \tag{2.7}$$

$$+ \frac{41 - 36x + 42x^2 - 16x^3}{6x^2(3-2x)} \ln(1-x). \tag{2.8}$$

In kinematic regions close to phase space boundaries, the spectrum is infrared sensitive and receives large nonperturbative corrections. Because the corresponding effects can be associated with the motion of the b quark inside the B meson, they are commonly referred to as "Fermi motion" [23]. This happens in the endpoint region $1-x = \mathcal{O}(\Lambda/m_b)$ of the charged lepton energy spectrum.

Fermi motion effects are included in the HQE by re-summing an infinite set of leading-twist corrections into a shape function $F(k_+)$, which governs the light-cone momentum distribution of the heavy quark inside the B meson,

$$F(k_+) = \frac{1}{2m_B} < B(v)|\bar{b}_v \delta(k_+ - iD_+) b_v|B(v) >, \tag{2.9}$$

where D_+ is the light cone component of the covariant derivative of QCD, which is defined with the help of a light-like vector $n_+ = (1,0,0,1)$ as the scalar product $D_+ = n_+ \cdot D$. This function is non-vanishing for values $-\infty < k_+ \leq \bar{\Lambda}$. The physical decay distributions are obtained from a convolution of parton model spectra with the function [25]

$$\frac{d\Gamma}{dE_l} = \int dk_+ F(k_+) \frac{d\Gamma^{parton}(m_b + k_+)}{dE_l}. \tag{2.10}$$

The non perturbative $F(k_+)$ is not calculable. However, if one assumes that u quark and s quark are massless, it can be obtained from other B decays, for example, $b \to s\gamma$. Using the CLEO measurement of the $b \to s\gamma$ photon spectrum [3], the ratio of partial and total branching fraction of $B \to X_u e\nu$ decays (Eq. 2.14) is calculated [17].

The endpoint singularities near $2E_l/m_b \sim 1$ are integrable, and the total decay rate is given model-independently by

$$\Gamma = \frac{G_F^2 |V_{ub}|^2 {m_b}^5}{192\pi^3} \left[1 - \frac{C_F \alpha_S}{2\pi}\left(\pi^2 - \frac{25}{4}\right)\right]. \tag{2.11}$$

The charmless electron energy spectrum from semileptonic B decays are models in the Monte Carlo samples which this analysis uses using Eq. 2.3. So the shape of the spectrum at low energy range has small uncertainties while that near end point has bigger uncertainties.

We measure the electron energy spectrum of $B \to X_u e\nu$ decays from 1.4 GeV to 3.5 GeV. Since we depend on the Monte Carlo samples for the ratio of $B \to X_c e\nu$ decays with and without kaons (R_{bc}^{-1}, Eq. 5.1), we have big model dependency. While the shape of the ratio R_{bc}^{-1} is used as in the Monte Carlo samples, the normalization is fitted to minimize the uncertainty. The error of normalization from the fit is considered as statistical error.

To fit the normalization of $B \to X_c e\nu$ spectrum against $B \to X_u e\nu$ and backgrounds, we need $B \to X_u e\nu$ input. Since theory has small error of order 2% at the low energy range of 1.4–1.8 GeV, and the Monte Carlo samples and

theory shows less than 5% difference, we take the shape of the $B \to X_u e\nu$ spectrum from the Monte Carlo samples and fit the normalization of it too.

2.4 $|V_{ub}|$ extraction

After we measure the charmless electron energy spectrum (N_{bu}), we calculate the partial branching fraction

$$\sum_{E_l^*=E_0}^{M_B/2} \mathcal{B}(B \to X_u e\nu; E_l^*) = \frac{\sum_{E_l^*=E_0}^{M_B/2} N_{bu}(E_l^*)}{\sum_{E_l^*=E_0}^{M_B/2} \epsilon_e(E_l^*) \cdot N_B}, \tag{2.12}$$

where E_l^* is the electron energy in the $\Upsilon(4S)$ rest frame, E_0 is the starting energy (typically 2.0 to 2.3 GeV), M_B is the B meson mass and ϵ_e is the electron efficiency defined using Monte Carlo samples as

$$\sum_{E_l^*=E_0}^{M_B/2} \epsilon_e(E_l^*) = \frac{\sum_{E_l^*=E_0}^{M_B/2} N_{bu}(E_l^*) \text{ with reconstructed electron}}{\sum_{E_l^*=E_0}^{M_B/2} N_{bu}(E_l^*) \text{ with generated electron}}, \tag{2.13}$$

and N_B is the total number of B mesons in the data (1.28234×10^7). It is twice of the accumulated on-peak luminosity (5.964×10^6 nb^{-1}) times $\overline{b}$ cross-section (1.075 nb). Twice is because there are two B mesons for each event.

The total $B \to X_u e\nu$ branching fraction is required in order to extract $|V_{ub}|$ from the measured electron energy spectrum. Since we only have partial branching fraction, we depend on theory[2]. The dimensionless shape function is defined as:

$$F_u(E_l^*) = \frac{1}{\mathcal{B}(B \to X_u e\nu)} \int dE_l^* \, \frac{d\mathcal{B}(B \to X_u e\nu; E_l^*)}{dE_l^*}, \tag{2.14}$$

E_l^*(GeV)	F_u
2.0 – 2.6	0.278 $\pm$0.052
2.1 – 2.6	0.207 $\pm$0.046
2.2 – 2.6	0.137 $\pm$0.034
2.3 – 2.6	0.078 $\pm$0.022

Table 2.1: The shape functions F_u for four E_l^* intervals.

where i_i is bin of which low edge is E_l^*=E_0 and i_f is that of which upper edge is E_l^*=$M_B/2$ $\approx$2.6 GeV.

The values and errors of F_u with different E_0's are derived by the CLEO Collaboration using theory [2] and the shape function parameters based on the measurement of the $B \to X_s\gamma$ photon spectrum [3]. They are summarized in Table 2.1.

A relation for the extraction of $|V_{ub}|$ from the total semileptonic branching fraction, with *BABAR* measured b quark mass and other OPE parameters [26] is [27, 28]:

$$|V_{ub}| = 0.00424\left(\frac{\mathcal{B}(B \to X_u e\nu)}{0.002}\frac{1.61\text{ps}}{\tau_b}\right)^{1/2}(1.0 \pm 0.028_{pert+nonpert} \pm 0.039_{m_b}), \tag{2.15}$$

where the first error arises from the uncertainty in the OPE expansion and the second from the uncertainty in the b quark mass. The *BABAR* measurement of b quark mass is $m_b(1\,\text{GeV}) = (4.61 \pm 0.07)\,\text{GeV}/c^2$ and that of the B lifetime is 1.604 ± 0.012 ps [10].

Chapter 3

The *BABAR* experiment

The main physics goal of the *BABAR* experiment is the study of *CP*-violating asymmetries in the decay of neutral B mesons. Secondary goals are measurements of decays of bottom and charm mesons and of τ leptons, and searches for rare processes which become accessible through the high luminosity of the PEP-II B Factory. The *BABAR* detector is designed for *CP*-violation studies, but it is also well suited for these other physics topics.

In the late 1980s, studies indicated that the best source of B mesons for such a physics program was an e^+e^- collider, operating at the $\Upsilon(4S)$ resonance, but in an *asymmetric* mode [29], i.e., with beams of unequal energy, resulting in B^0 mesons with significant momenta in the laboratory frame. This enables the B^0 mesons' decay times to be inferred from their now-measurable decay lengths. The PEP-II B Factory was designed with these characteristics.

3.1 The PEP-II storage ring

The PEP-II B Factory [30–32] is an asymmetric e^+e^- collider designed to operate at a center-of-mass (CM) energy of 10.58 GeV, the mass of the $\Upsilon(4S)$ resonance. This resonance decays nearly exclusively to $B^0\overline{B}^0$ and B^+B^- pairs

$e^+e^- \rightarrow$	cross-section (nb)
$b\overline{b}$	1.075
$c\overline{c}$	1.30
$s\overline{s}$	0.35
$u\overline{u}$	1.39
$\tau^+\tau^-$	0.94
$\mu^+\mu^-$	1.16
e^+e^-	$\sim$40

Table 3.1: Production cross-sections at the peak of the $\Upsilon(4S)$ resonance. The e^+e^- cross-section is the effective cross-section, expected within the experimental acceptance.

and thus provides an ideal laboratory for the study of B mesons.

In PEP-II, an electron beam of 9 GeV collides head-on with a positron beam of 3.1 GeV. The difference in energy of the two beams results in a relativistic boost of the collision products; the CM frame is moving with respect to the lab frame with $\beta\gamma = 0.56$. The resulting average separation of the B decay vertices is on the order of 250 μs, which is sufficient for precise measurements of CP-asymmetries.

While most data are recorded at the peak of the $\Upsilon(4S)$ resonance, about 12% are taken at a CM energy 40 MeV lower to allow for studies of the non-resonant background. The accumulated luminosity is shown in Fig. 3.1. The cross-sections for the production of fermion pairs at the $\Upsilon(4S)$ are shown in Table 3.1.

The requirements for high beam currents, asymmetric energies and head-on collisions resulted in an innovative design for the interaction region. Beam-line elements are positioned very close to the interaction point, which is

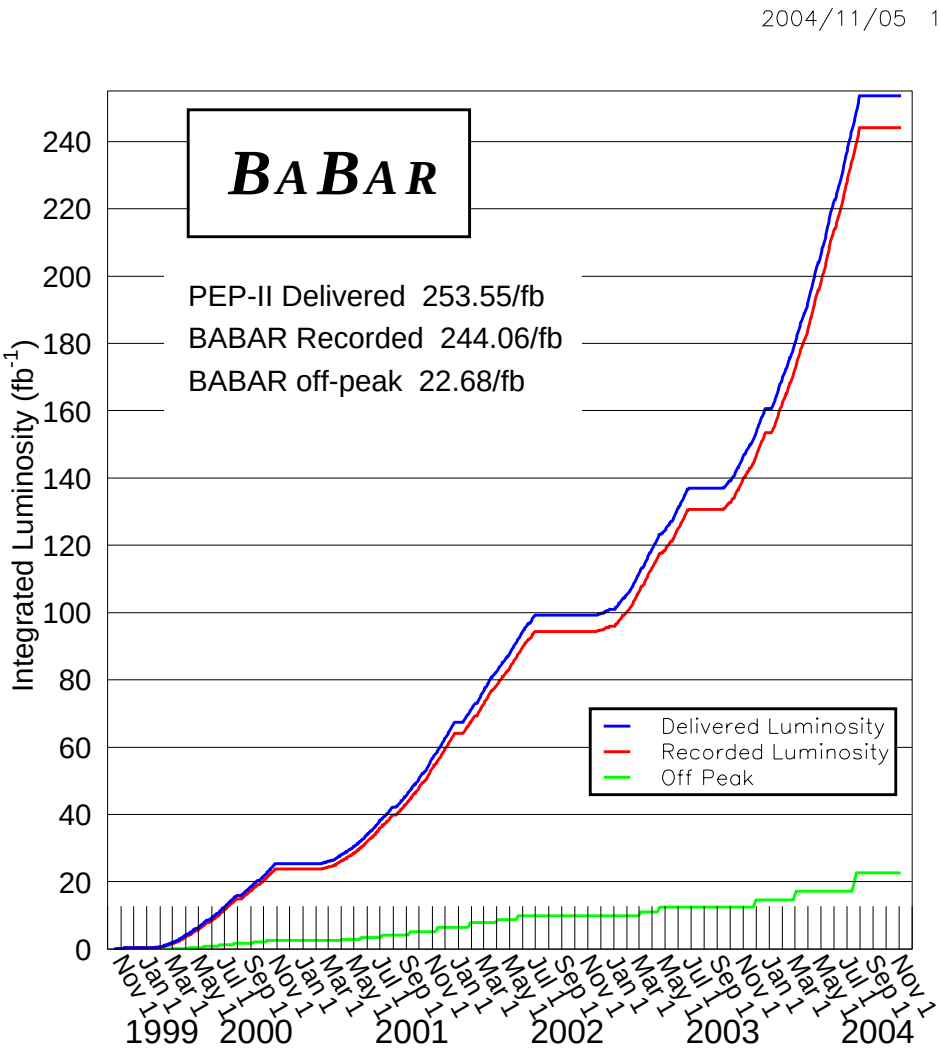

Figure 3.1: Luminosity vs. time.

Parameters	Design	Typical
Energy HER/LER (GeV)	9.0/3.1	9.0/3.1
Current HER/LER (A)	0.75/2.15	1.5/2.5
# of bunches	1658	1588
Bunch spacing (ns)	4.2	6.3–10.5
σ_{L_x} (μm)	110	120
σ_{L_y} (μm)	3.3	5.6
σ_{L_z} (mm)	9	9
Luminosity (10^{33} cm^{-2}s^{-1})	3	9

Table 3.2: PEP-II beam parameters: Values are given both for the design and for typical colliding beam operation in the first year. HER and LER refer to the high energy e^- and low energy e^+ ring, respectively. σ_{L_x}, σ_{L_y} and σ_{L_z} refer to the horizontal, vertical, and longitudinal rms size of the luminous region.

contained within a cylindrical beryllium beam-pipe. Beam-beam interference effects are minimized by arranging for the beams to collide only at the interaction point and by dividing the high currents into a large number of bunches. The parameters of the PEP-II storage rings are presented in Table 3.2.

3.2 The *BABAR* detector

The *BABAR* detector [30–32] has two charged particle tracking systems: the Silicon Vertex Tracker (SVT) and the Drift Chamber (DCH), and three particles identification systems: the detector of internally reflected Cherenkov light (DIRC), the electromagnetic calorimeter (EMC) and the instrumented flux return (IFR), and a superconducting coil which provides a 1.5 T solenoidal magnetic field. The longitudinal section of the *BABAR* detector is shown in Fig. 3.2 and the transverse section is shown in Fig. 3.3. The main features of

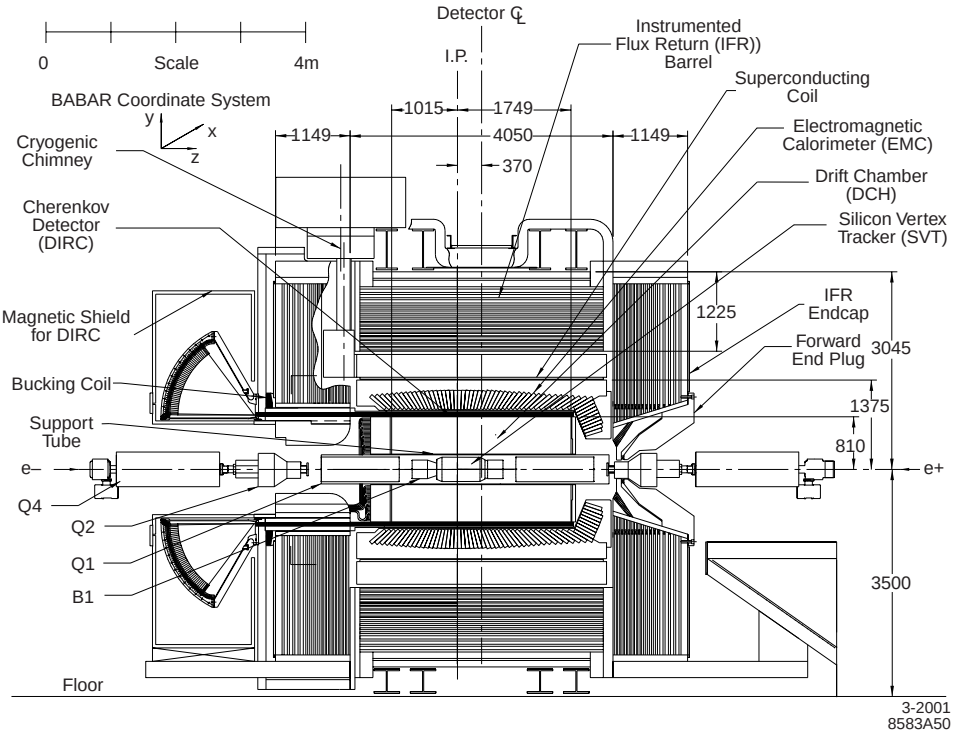

Figure 3.2: The longitudinal section of *BABAR* detector.

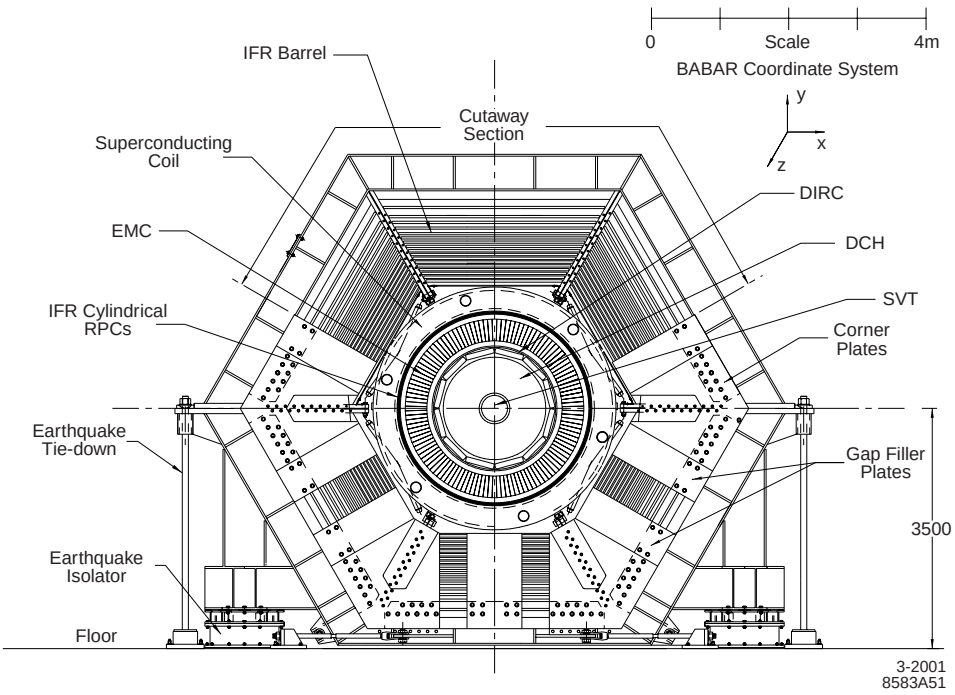

Figure 3.3: The transverse section of *BABAR* detector.

each of the detector systems are reviewed and summarized here.

3.2.1 Silicon Vertex Tracker (SVT)

The goal of the SVT is to measure the angles and positions of charged particles just outside the beam pipe in order to provide precise reconstruction of the decay vertices of the two primary B mesons so as to determine the time between the two decays. The SVT is solely responsible for tracking charged particles with p_T <100 MeV/c, since those tracks will not reach the DCH.

The SVT is composed of five layers of double-sided silicon microstrip

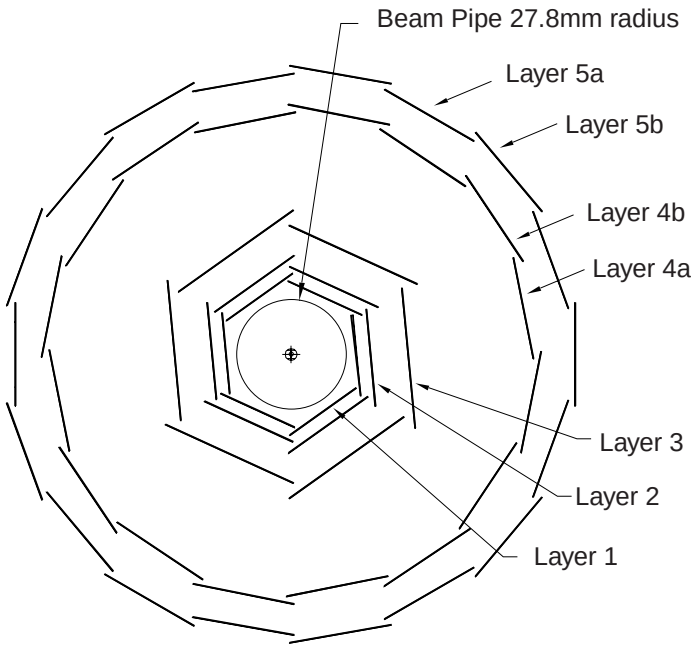

Figure 3.4: The transverse section of SVT.

detectors as shown in Fig. 3.4 [33]. The inner three layers primarily provide position and angle information for the measurement of the vertex position. The outer two layers provide the coordinate and angle measurements needed for linking the SVT and DCH tracks.

The modules of the inner three layers are straight, while the modules of the outer layers are arch-shaped as shown in Fig. 3.5. This arch design was chosen to minimize the amount of silicon required to cover the solid angle, while increasing the crossing angle for particles near the edges of acceptance. The modules are divided electrically into two half-modules, which are read out at the ends.

The inner sides of the detector have strips which are oriented perpendicular to the beam direction to measure the z-coordinate (z-strip), whereas the outer sides have longitudinal strips allowing for ϕ-coordinate measurement (ϕ-strip) with a precision of better than about $250\,\mu$m. This corresponds to a single vertex precision of better than $80\,\mu$m. The active parts of the SVT cover the polar angle between 20.1° and 150.2°.

At PEP-II the radiation near the interaction region is peaking in the bending plane of the machine, with a maximum of $240\,\mathrm{krad/\,yr}$ for the innermost layer detectors, and $100\,\mathrm{krad/\,yr}$ for the electronics in the same layer. The system is designed to withstand such continuous radiation exposure for at least ten years.

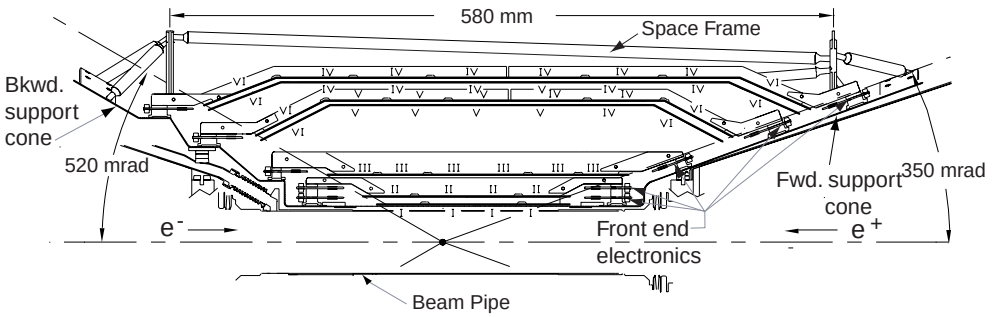

Figure 3.5: Schematic view of SVT: longitudinal section. The Roman numerals label the six different types of sensors.

3.2.2 Drift CHamber (DCH)

The goal of the DCH is to measure the momenta and angles of charged particles with high precision. The DCH complements the measurements of the impact parameter and the directions of charged tracks provided by the SVT near the IP [34].

The DCH should be able to measure the transverse momenta for tracks with momentum above 1 GeV/c with a resolution of $\sigma_{p_T} \approx 0.3\% \times p_T$. The DCH is a 2.8 m long cylinder and its inner and outer radii are 23.6 cm and 80.9 cm respectively. It is composed of 40 layers of small, approximately hexagonal cells. Due to the asymmetric beam energies of the PEP-II collider, the DCH was designed to minimize the material in the forward direction and is positioned asymmetrically about the interaction point.

To minimize multiple scattering inside the DCH, low-mass wires (20 μm

gold-plated tungsten-rhenium for the sense wires, 120 μm and 80 μm gold-plated aluminum for the field wires) and a helium-based gas mixture (helium:isobutane=4:1) were chosen. This gas mixture provides good spatial and $\mathrm{d}E/\mathrm{d}x$ resolution and reasonably short drift time, while minimizing the material. The gas and the wires total a radiation length of $0.3\%X_0$ for tracks at 90°. The inner cylinder is made of 1 mm thick beryllium, which corresponds to $0.28\%X_0$. The outer cylinder consists of 2 layers of carbon fiber on a Nomex core, corresponding to $1.5\%X_0$. The scatter plot of $\mathrm{d}E/\mathrm{d}x$ as a function of momentum is shown in Fig. 3.6, with parameterized Bethe-Bloch curves. Protons and deuterons are mainly from beam gas interactions.

Nominal voltages of 1930 V for the sense wires and 340 V for the field-shaping wires at the boundaries of the superlayers are supplied by HV assemblies mounted on the feed-throughs of the rear endplate. Other field wires are connected to the ground.

The DCH provides prompt trigger signals; information from all 7104 channels is sent at a sampling frequency of 3.75 MHz to the Level-1 trigger system.

3.2.3 Detector of Internally Reflected Cherenkov light (DIRC)

The DIRC is designed to provide an excellent kaon identification, not only for tagging purposes where kaon momenta extend up to about 2.0 GeV/c, but also at higher momenta for rare B meson decay processes [35]. In order to distinguish between the two-body decay modes $B^0 \to \pi^+\pi^-$ and $B^0 \to K^\pm\pi^\mp$,

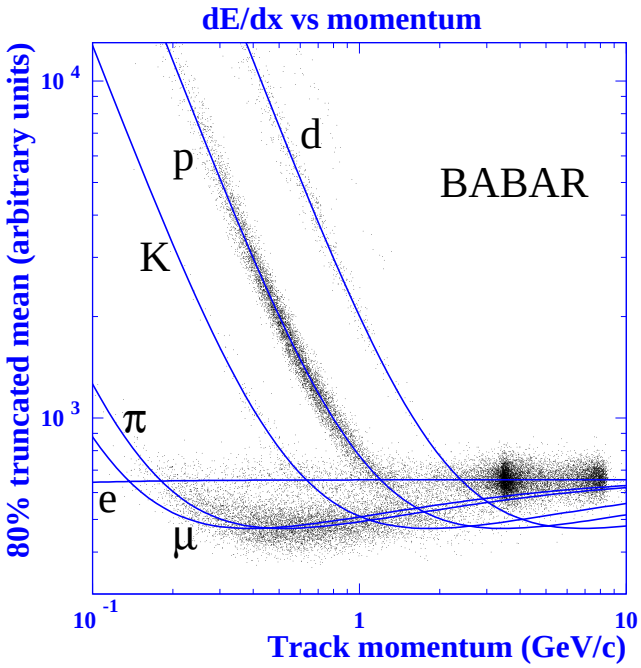

Figure 3.6: dE/dx vs. momentum and parameterized Bethe-Bloch curves.

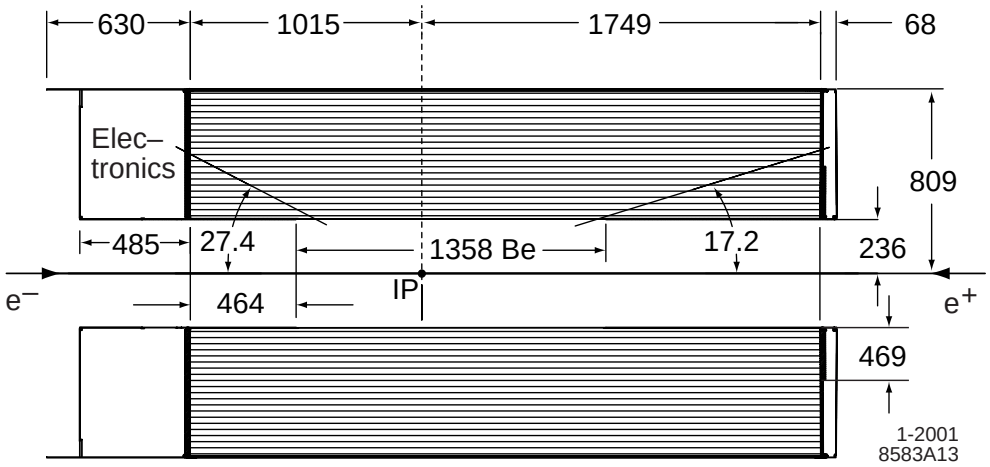

Figure 3.7: Longitudinal section of the DCH with principal dimensions; the chamber center is offset by 370 mm from the interaction point (IP).

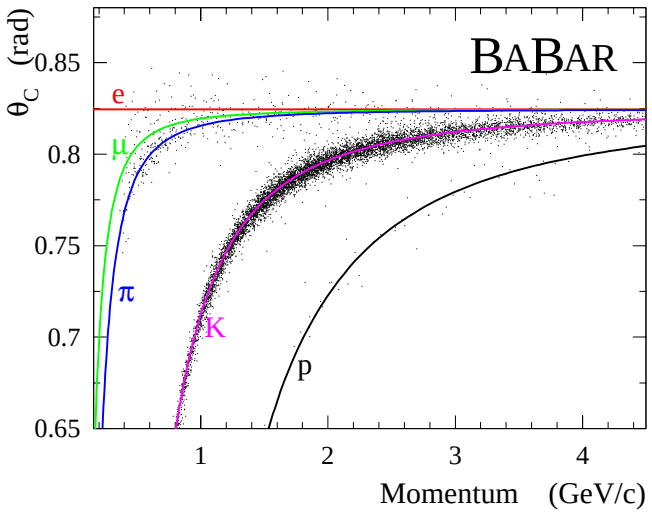

Figure 3.8: Cherenkov angle vs. momentum and parameterized curves.

the DIRC must be able to separate pions from kaons up to about 4.0 GeV/c at large dip angles in the laboratory frame. The DIRC also participates in muon identification in the momentum range where the IFR is inefficient, typically below ∼750 MeV/c.

Cherenkov light is produced in 4.9 m long bars of synthetic fused silica of rectangular cross section, 1.7 cm ×3.5 cm, and transported by total internal reflection, preserving the angle of emission, to an array of photomultiplier tubes. This array forms the backward wall of a toroidal water tank that is located beyond the backward end of the magnet. Only this end of the bars is instrumented. A mirror placed at the other end of each bar reflects forward-going photons to the instrumented end. The DIRC technique was chosen for its many advantages. It presents an amount of material comparable to that

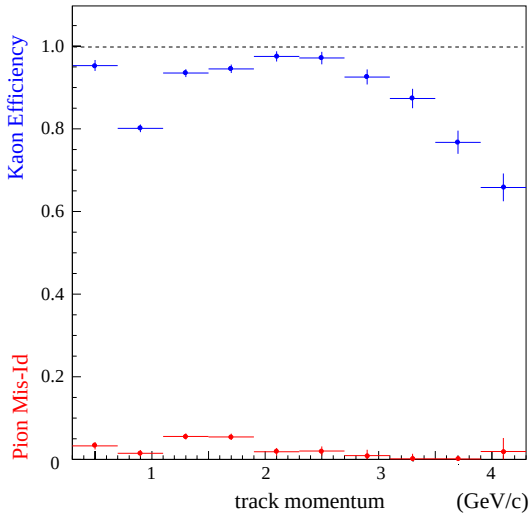

Figure 3.9: Kaon efficiency and mis-identification rate from pions vs. momentum.

of other techniques (14% X_0 for a particle at normal incidence). The DIRC occupies only 8 cm of radial space, its material is located close to the front faces of the crystals and has minimal impact on the EMC performance for soft photon detection. Also, the DIRC performance tends to improve with the steepness of incidence of particles, as more light is generated and trapped at steeper angles, which matches well the needs of a detector at an asymmetric B Factory.

The refractive index of quartz is close to 1.474. In a quartz radiator, the Cherenkov threshold for kaons ($\sim$460 MeV/c) is well below the value of momentum for which there is no possible confusion between a pion and a kaon through ionization loss measurement ($\mathrm{d}E/\mathrm{d}x$) in the DCH ($\sim$700 MeV/c): the two systems are remarkably complementary as far as π/K separation is concerned. The difference in Cherenkov angle between a pion and a kaon at

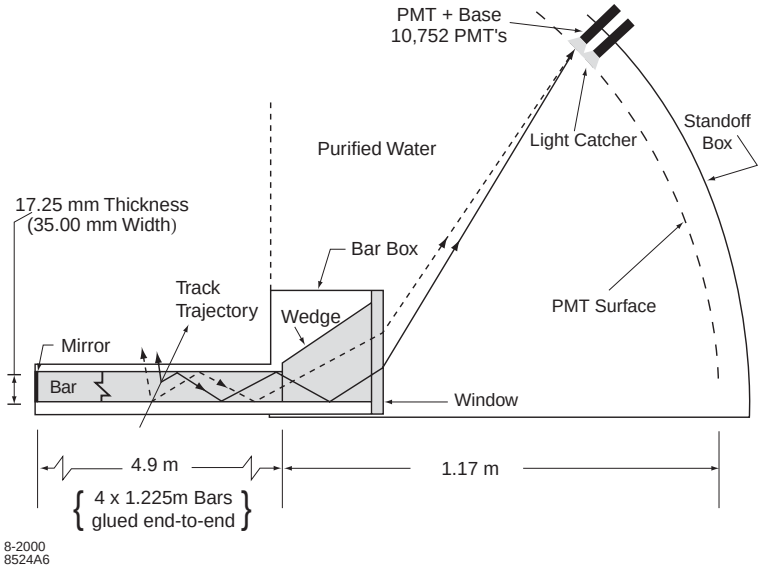

Figure 3.10: Schematics of the DIRC fused silica radiator bar and imaging region.

4.0 GeV/c is as small as 6.5 mrad (the same difference occurs between a muon and a pion at 700 MeV/c). A good π/K separation therefore requires resolutions on the Cherenkov angle for a track of 2 mrad or better. The cherenkov angle as a function of momentum is shown in Fig. 3.8 with parameterized curves. The kaon selection efficiency and mis-identification rate from pions as a function of momentum are shown in Fig. 3.9, with tracks from D^0 sample.

The single photoelectron resolution, intrinsically limited by geometry and quartz achromaticity, are obtained by combining measurements from the large number of photoelectrons generally observed for each track.

Parameters	Values
Radiation Length	1.85 cm
Moliĕre Radius	3.8 cm
Density	4.53 g/ cm^3
Light Yield	50,000 γ/ MeV
Light Yield Temp. Coeff.	0.28 %/°C
Peak Emission $\lambda_{\max}$	565 nm
Refractive Index ($\lambda_{\max}$)	1.80
Signal Decay Time	680 ns (64%)
	3.34 μs (64%)

Table 3.3: Properties of CsI(Tl).

3.2.4 ElectroMagnetic Calorimeter (EMC)

The goal of the EMC is to detect electromagnetic showers with excellent energy and angular resolution over an energy range from 20 MeV to 9 GeV. The EMC provides good electron identification down to about 0.5 GeV and information for neutral hadron identification. It uses a quasi-projective arrangement of crystals made from thallium doped cesium iodide(CsI(Tl)) covering a range of CM solid angle of $-0.916 \leq \cos\theta \leq 0.895$. The crystals are arranged in two sections, a barrel and a forward endcap as shown in Fig. 3.11.

Some properties of thallium-doped CsI are listed in Table 3.3. The high light yield and small Moliĕre radius allow for excellent energy and angular resolutions. The short radiation length allows for a compact design. The high light yield and the emission spectrum permit efficient use of silicon photodiodes which operate well in high magnetic fields.

The length of the crystals vary between 29.6 cm ($16X_0$) and 32.4 cm

($17.5X_0$). The barrel and outer five rings of the endcap have less than $0.3\sim0.6X_0$ of material in front of the crystal faces. The typical area of the front face is $4.7\times4.7\,\mathrm{cm}^2$, while the back face area is typically $6.1\times6.0\,\mathrm{cm}^2$. The crystals act not only as a total-absorption scintillating medium, but also as a light guide to collect light at the photodiodes that are mounted on the rear surface.

The photon detector consists of two $2\times1\,\mathrm{cm}^2$ silicon PIN diodes glued to a transparent 1.2 mm-thick polystyrene substrate which is glued to the center of the rear face of the crystal. Each of the diodes is directly connected to a low-noise preamplifier.

The requirements on energy resolution is of the order of $1\sim2\%$. Below energies of 2 GeV, the π^0 mass resolution is dominated by the energy resolution. At higher energies, the angular resolution becomes dominant, and therefore is required to be of the order of a few mrad. The target energy resolution for photons at 90° is:

$$\frac{\sigma_E}{E} = \frac{1\%}{\sqrt[4]{E(\mathrm{GeV})}} \oplus 1.2\% \tag{3.1}$$

where E and σ_E refer to the energy of a photon and its rms error, measured in GeV. The 1% term arises primarily from the fluctuations in photon statistics, but it is also impacted by electronic noise in the photon detector and its electronics. The 1.2% term, which is dominant at higher energies($> 1\,\mathrm{GeV}$), arises from non-uniformity in light collection, leakage or absorption in the material between and in front of the crystals and uncertainties in the calibrations. The angular resolution is determined by the transverse crystal size and the distance from the interaction point. The target angular resolution for photons at

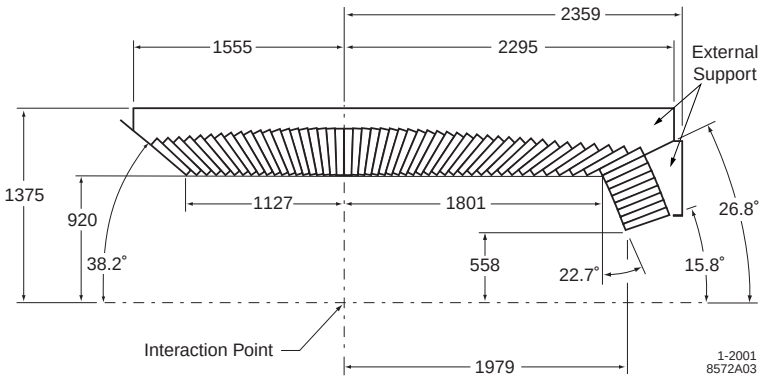

Figure 3.11: A longitudinal cross section of the EMC (only the top half is shown) indicating the arrangement of the 56 crystal rings. The detector is axially symmetric around the z-axis. All dimensions are given in mm.

a polar angle of 90° is:

$$\sigma_{\theta,\phi} = \frac{3\,\text{mrad}}{\sqrt{E(\,\text{GeV})}} \oplus 2\,\text{mrad}. \tag{3.2}$$

A position resolution of a few mm will translate into an angular resolution of a few mrad.

3.2.5 Instrumented Flux Return (IFR)

The goal of the IFR is to identify muons and to detect neutral hadrons (primarily K_L^0 and neutrons). The principal requirements for the IFR are large solid angle coverage, good efficiency to identify muons down to momenta below 1 GeV/c. To achieve the needed measurement goals, the magnet flux return steel is instrumented with single gap resistive plate chambers (RPCs) as shown in Fig. 3.12.

The IFR is 6.35 m in length, 5.84 m in height and 6.75 m in width. The

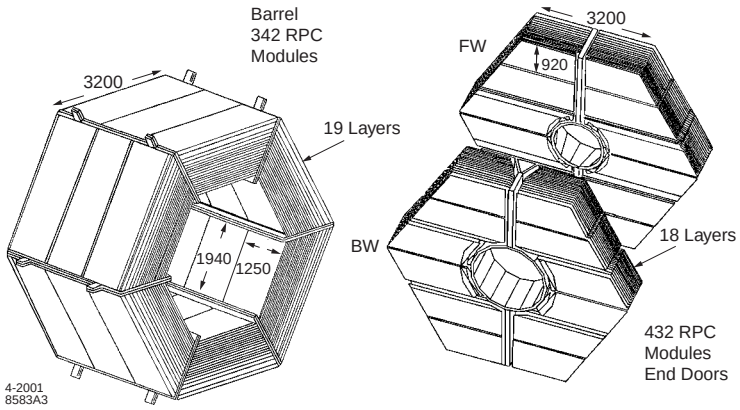

Figure 3.12: Overview of the IFR: Barrel sectors and forward (FW) and backward (BW) end doors; the shape of the RPC modules and their dimensions are indicated.

inner surface of each of the six sextants that make up the barrel section is at a radial distance of approximately 1.70 m from the beam line. The polar angle coverage is down to 300 mrad in the forward direction and 400 mrad in the backward direction. The average chamber efficiencies are 78% in the barrel and 87% in the endcaps.

The gas contained within the chamber is a mixture of isobutane (4.5%), argon (56.7%) and freon (38.8%). A charged particle traversing an RPC gap produces a quenched spark, which is detected on external aluminum pickup electrodes. The discharge is very fast (of order 100 pC). The pulse rise time is around 2 ns and the duration is typically around 20 ns.

The aluminum pickup strips on either side of the chamber are arranged orthogonally so as to provide a three-coordinate measurement. Strips in the barrel have a pitch of 38.5 mm for measuring z and 19.7 mm to 33.5 mm for

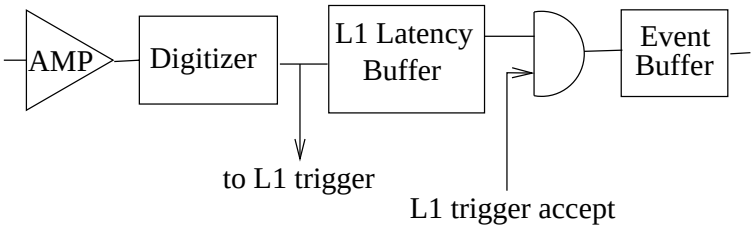

Figure 3.13: Schematic diagram of the Front-End Electronics (FEE). Analog signals arrive from the left, proceed conditionally through the indicated steps and are injected into the remainder of the data acquisition system.

measuring ϕ. In the end caps, the strip pitches are 38.0 mm and 28.4 mm for the measurement of x and y coordinates respectively. The IFR delivers timing information, which is then employed in the trigger.

3.3 Front end electronics

Each subsystem has its own custom-made front end electronics (FEE) situated in the detector. These apply simple amplification, shaping and digitization to the data. The signals are then stored in a trigger latency buffer and sent by optical fiber to the Read Out Modules (ROMs), situated outside of the detector, for further processing. Fig. 3.13 shows the typical job of the FEE. The EMC and DCH signals are passed on to the Level-1 trigger (described in Section 3.4), for the other subsystems the data are only read out for an L1 accept.

3.4 The trigger system

The *BABAR* trigger system consists of a Level-1 (L1) hardware trigger and a Level-3 (L3) software trigger.

The L1 trigger is designed to select candidate physics events at a rate of no more than 2kHz, the maximum rate allowed by the data acquisition system. It consists of the drift chamber trigger (DCT), calorimeter trigger (EMT) and global trigger (GLT). The maximum L1 response latency for a given collision is $12\,\mu$s. The DCT and EMT construct 'primitive objects' which are then combined by the GLT to produce a whole range of 'trigger lines'. If a GLT trigger line is active for a time corresponding to a beam crossing, an L1 accept is produced.

The primitive objects of main DCT are 'short' and 'long' tracks, corresponding to tracks with p_T >120 MeV/c and >150 MeV/c respectively. For EMT, the basic trigger object is a 'tower', corresponding to three adjacent rows of crystals along the length of the calorimeter.

The trigger system has been designed such that the EMC and DCH triggers are orthogonal. This allows the individual and combined trigger efficiencies to be easily determined. For $B\overline{B}$ events the efficiency for both DCT and the EMT is over 99%, with the combined efficiency being greater than 99.9%.

The L3 trigger uses more complex algorithms to reduce the 2kHz input from the L1 trigger to an event rate of 100Hz, which is the maximum rate that

the event processing farm and mass storage facility can tolerate. It carries out an analysis of the complete event, using timing information as well as simple track finding and calorimeter clustering to accept or reject events. Beam background events are rejected by looking at the impact parameters of the L3 tracks. L3 decisions are based on simple track cluster topologies rather than recognizing actual physics processes.

The L3 trigger lines can be pre-scaled to keep the trigger rate under control. This is done for physics processes with high cross section like Bhabha events and two-photon events. These are needed for luminosity measurements and calibration purposes, but not at the rate at which they occur. The L3 trigger runs on a 125 node Online Event Processing (OEP) farm.

To calculate efficiencies, monitor and to calibrate, L1 and L3 pass through events (which are not required to pass the triggers) at a low rate, which is called a random trigger.

Chapter 4

The data samples and event selection

This analysis is based on data recorded in the year 2001, corresponding to $59.64\,\mathrm{fb}^{-1}$ collected at the $\Upsilon(4S)$ resonance (10.58 GeV), called *on-peak* data, and $6.92\,\mathrm{fb}^{-1}$ at an CM energy 40 MeV below the resonance (10.54 GeV), called *off-peak* data. Due to the kinematic limit, the off-peak data can not have B mesons. Table 4.1 gives an overview over the data samples selected for this analysis.

We histogram the CM energy of electrons in 42 bins from 1.4 GeV to 3.5 GeV with a bin size of 0.05 GeV. The electrons in the on-peak data are consist of

- semileptonic : from semileptonic B decays (ex: $B \to De\nu$),
- $B\overline{B}$ background : from B decays but not semileptonic,
  - from secondary decays (ex: $B \to DX$ and $D \to Ke\nu$),
  - from mis-identification,
  - from wrong reconstruction: $E_l^*(rec) - E_l^*(gen) > 0.1\,\mathrm{GeV}$, $E_l^*(rec)$ and $E_l^*(gen)$ are the reconstructed and generated electron energy in the $\Upsilon(4S)$ rest frame, respectively,

Dataset	Time	$\mathcal{L}(\text{fb}^{-1})$
2001-b1-s2-on	03/16/2001 – 07/15/2001	10.452
2001-b1-s3-on	07/10/2001 – 09/13/2001	6.297
2001-b1-s4-on	09/13/2001 – 10/11/2001	4.605
2001-b1-s5-on	10/13/2001 – 11/01/2001	4.005
2001-b1-s6-on	11/02/2001 – 11/30/2001	4.219
2001-b1-s7-on	12/01/2001 – 12/23/2001	4.535
2002-b1-s0-on	01/12/2002 – 02/02/2002	2.502
2002-b1-s1-on	02/02/2002 – 02/11/2002	1.260
2002-b1-s2-on	02/14/2002 – 05/31/2002	17.699
2002-b1-s3-on	06/01/2002 – 06/23/2002	3.323
2002-b1-s4-on	06/24/2002 – 06/30/2002	0.833
2001-b1-s0-off	02/10/2001 – 02/13/2001	0.005
2001-b1-s2-off	03/16/2001 – 07/15/2001	1.291
2001-b1-s3-off	07/10/2001 – 09/13/2001	1.058
2001-b1-s6-off	11/02/2001 – 11/30/2001	1.323
2002-b1-s0-off	01/12/2002 – 02/02/2002	1.352
2002-b1-s2-off	02/14/2002 – 05/31/2002	1.891
Total on resonance	03/16/2001 – 06/30/2002	59.64
Total off resonance	02/10/2001 – 05/31/2002	6.92

Table 4.1: Summary of the data used in this analysis.

  - from QED processes,
  - from J/ψ decays,
  - from photon conversion,
  - from Dalitz decay,
  - $\cdots$,

- continuum background : from non B decays.

The $B\overline{B}$ background is estimated using Monte Carlo samples and the continuum background is estimated using the off-peak data. We subtract the $B\overline{B}$ background electron energy spectrum and the continuum background spectrum from the off-peak electron energy spectrum to obtain the signal electron energy spectrum N_{SL}. Since there are only 12% of the off-peak data samples to the on-peak data samples, the scale factor is needed.

The scale factor for the continuum background $\xi_{\mathcal{L}}$ is given as:

$$\xi_{\mathcal{L}} = \frac{N_{on}}{N_{off}} = \frac{\mathcal{L}_{on}}{\mathcal{L}_{off}} \cdot \frac{E_{off}^2}{E_{on}^2}, \tag{4.1}$$

where N are the number of events, $\mathcal{L}$ are the luminosities of the data sets, E_{on} is 10.58 GeV and E_{off} is 10.54 GeV. This relation is derived from the fact that the number of events is the luminosity times the cross-section and the cross-section is proportional to the inverse of the CM energy. With the given numbers, $\xi_{\mathcal{L}}$ is 8.55. The relative error on $\xi_{\mathcal{L}}$ is 1.7%, estimated from the errors

of the luminosities and the CM energies [1]. To account for the difference in the beam energies, the measured electron energy in the off-peak data are scaled by a factor of 10.58/10.54=1.0038.

For each semileptonic B meson, there always is the second B meson in the event. These mesons are called as *the second* B mesons in this document. They decay fully inclusively.

4.1 The event selection

The data samples used in this analysis pass one of two Level 3 triggers and they satisfy additional event selection criteria. These are discussed in detail next.

4.1.1 The trigger and filter

The *BABAR* data are selected and recorded through the L3 triggers and the front-end filters of the Prompt Reconstruction. Selecting the L3 trigger lines and filter ensures a well-controlled sample, with a measurable (and simulatable) efficiency.

The following two L3 trigger lines are required for this analysis: the first is based on the charged tracks recorded from the DCH information only:

- $|d_0^{IP}| < 1.5\,\mathrm{cm}$, $|d_0^{IP}|$ is the distance of closest approach to the interaction

[1] The rms spread of E_{on} is 5.5 MeV, that of E_{off} is 2.3 MeV [30] and the relative errors on the luminosity calculations are 1.2% [36]

point in the $x - y$ plane,

- $z_0 < 10.0\,\mathrm{cm}$, z_0 is the z-coordinate of a track's point of closest approach to the z-axis,
- $p_T \geq 0.25\,\mathrm{GeV}/c$, p_T is the transverse momentum.

The second requires for clusters on the EMC:

- $E_{Lab} \geq 0.10\,\mathrm{GeV}$,
- $E_{CM} \geq 0.35\,\mathrm{GeV}$,
- Number of good clusters ≥ 2,
- Effective mass $\geq 1.5\,\mathrm{GeV}$, the effective mass is the mass calculated using the locations and energies of all good clusters, which is not the real mass if the particle does not discharge all the energy in the calorimeter.

For both cases, the event may also not be a Bhabha event according to the criteria summarized in Table A.1 and Table A.2 of Appendix A.

In case the event does not pass one of the two criteria described above, the following criteria are required [37]:

- Number of tracks ≥ 3,
- $R_2^{ch} \leq 0.98$.

The R_2^{ch} is the ratio of the second to zeroth Fox-Wolfram moments [38] calculated only with the charged tracks satisfying $|d_0^{IP}| \leq 1.5\,\mathrm{cm}$, $z_0 \leq 10.0\,\mathrm{cm}$, and $p_T \geq 0.1\,\mathrm{GeV}/c$ in the event.

4.1.2 Event selection cuts

We require at least one electron with a CM energy above 1.4 GeV. For the off-peak data, 1.0 GeV is required to fit its shape from below 1.4 GeV.

To suppress non-resonant continuum events containing a high energy electron, selection criteria are applied to the data samples. Most of these backgrounds are events with low charged multiplicity, originating mainly from $q\overline{q}$ and QED pair production, which result in events with jet-like topology. The following cuts are applied to the events to reduce these backgrounds:

- $R_2 \leq 0.6$, R_2 is the ratio of the second to zeroth Fox-Wolfram moments [38] calculated from all charged tracks in the event,
- Number of charged tracks ≥ 4,
- Multiplicity ≥ 6[2],
- Total charge ≤ 2[3].

[2]Multiplicity is total number of charged and neutral tracks.

[3]This is not important for this analysis. It is applied for other analyses which share the same data samples.

Dataset	Equiv. Lumi.	Number of reconstructed B mesons
$B^0\overline{B}^0$ generic	$133\,\mathrm{fb}^{-1}$	143.3×10^6
B^+B^- generic	$132\,\mathrm{fb}^{-1}$	141.8×10^6

Table 4.2: Summary of the Monte Carlo samples used in this analysis.

4.2 The Monte Carlo samples

The Monte Carlo samples are generated with the `EvtGen` [39] generator and the experiment is simulated with the software package called `GEANT4` [40]. The $B \to X_u e\nu$ decays are simulated based on the ISGW2 model [41, 42]. For the $B \to X_c e\nu$ decays three models are employed to simulate different decay modes. The decay to $D^* e\nu$ is modeled following a form factor based parameterization of HQET [43], for decays to $De\nu$ and higher mass charm meson states the ISGW2 model is used The non-resonant decays to $D^{(*)}\pi e\nu$ are modeled according to a prescription by Goity and Roberts [44].

The Monte Carlo samples used for this analysis are summarized in the Table 4.2. The generic $B\overline{B}$ Monte Carlo represent the full simulation of all possible decays of the B meson.

4.3 The inclusive samples

The data samples and the Monte Carlo samples with the electron requirement are called the *electron samples*; the electron data samples and the electron Monte Carlo samples. There are samples with no electron requirement and they are called the *inclusive samples*; the inclusive data samples and

the inclusive Monte Carlo samples. The inclusive samples are used to get kaon multiplicity distribution from B mesons which can decay into any channels.

Chapter 5

Analysis

5.1 Introduction

The b quark can decay only into quarks of a different generation, and it has W-mediated decays to both first-generation (u) and second-generation (c) quarks; $B \to X_u e\nu$ and $B \to X_c e\nu$. In the Monte Carlo sample, $B \to X_c e\nu$ is specified as $B \to Dl\nu$, $B \to D^* l\nu$, $B \to D^{**} l\nu$, and $B \to D^{(*)}\pi l\nu$. Their electron energy spectra are shown in Fig. 5.1 with that of $B \to X_u e\nu$. As shown in this figure, $B \to X_u e\nu$ is small compared to $B \to X_c e\nu$. Because of the kinematics, there is almost no $B \to X_c e\nu$ decay with CM electron energy (E_l^*) of about 2.5 GeV or higher, and almost no $B \to X_u e\nu$ decay with about 2.8 GeV or higher [1].

To give an idea how big effect the uncertainty on $B \to X_c e\nu$ decays can make on $B \to X_u e\nu$ measurement, the ratio of $B \to X_u e\nu$ over $B \to X_c e\nu$ decay yields from Monte Carlo sample is shown in Fig. 5.2. It shows that 1% of systematic error on $B \to X_c e\nu$ causes relative errors of 50%, 20% and 7% on $B \to X_u e\nu$ at E_l^*= 2 GeV, 2.1 GeV and 2.2 GeV, respectively. The goal of this analysis is to measure the electron energy spectrum of $B \to X_c e\nu$ decay

[1] There can be some due to the reconstruction errors.

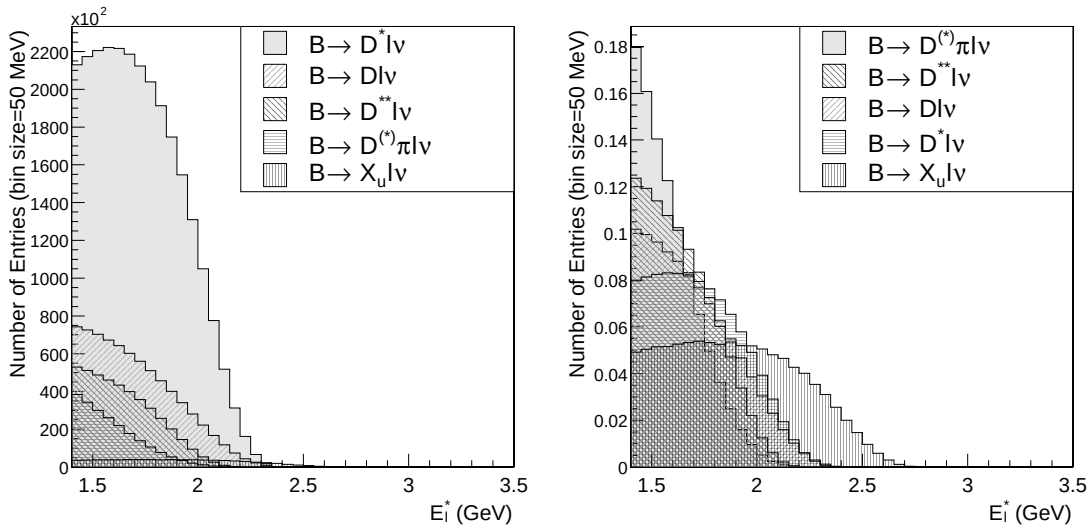

Figure 5.1: (a) The electron energy spectra of all modes from Monte Carlo sample. (b) Same as (a) except their areas are normalized to be 1.

with a systematic error of order of 1% to reduce the electron energy cut as much as possible.

The $B \to X_c e\nu$ decays are tagged with charged kaons. To understand the idea, let's think in the Monte Carlo samples first. Since the number of kaons (n_K^g) produced in a semileptonic decay of a B meson are known in Monte Carlo samples, we can get the following ratio:

$$R_{bx} \equiv \frac{N_{bx}(n_K^g \geq 1)}{N_{bx}(n_K^g \geq 0)}, \ (x{=}c \text{ or } u), \tag{5.1}$$

where R_{bc}^{-1} and R_{bu} are shown in Fig. 5.3, and the following relations between

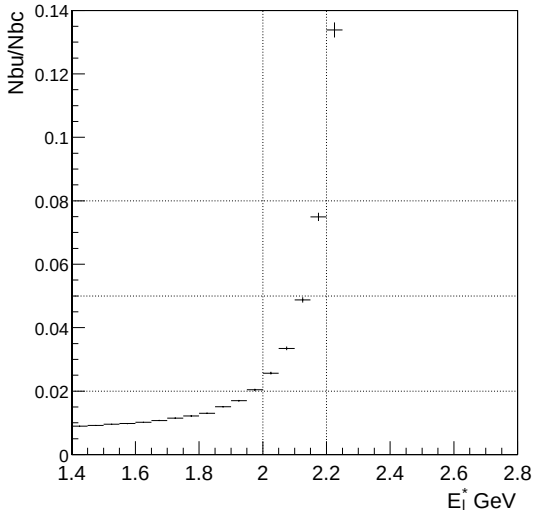

Figure 5.2: Ratio of electron energy spectrum from $B \to X_u e\nu$ over $B \to X_c e\nu$, using Monte Carlo sample.

electron energy spectra:

$$N_{bc}(n_K^g \geq 0) = R_{bc}^{-1} \cdot N_{bc}(n_K^g \geq 1) \tag{5.2}$$

$$= R_{bc}^{-1} \cdot \Big(N_{SL}(n_K^g \geq 1) - R_{bu} \cdot N_{bu}(n_K^g \geq 0) \Big), \tag{5.3}$$

where N_{bc}, N_{bu}, N_{SL} denotes the electron energy spectrum of $B \to X_c e\nu$, $B \to X_u e\nu$ and $B \to X_{(c,u)} e\nu$ decays, respectively, n_K^g is the number of generated kaon.

By rearranging $N_{SL} = N_{bc} + N_{bu}$ using Eq. 5.3, we get the electron energy spectrum for $B \to X_u e\nu$ decays:

$$N_{bu}(E_l^*) = \frac{N_{SL}(E_l^*) - R_{bc}^{-1}(E_l^*) \cdot N_{SL}(E_l^*, n_K^g \geq 1)}{1 - R_{bc}^{-1}(E_l^*) \cdot R_{bu}(E_l^*)}. \tag{5.4}$$

We get R_{bu} from Monte Carlo samples. The shape of R_{bc}^{-1} is from Monte Carlo samples and the magnitude is fitted using data to minimize model de-

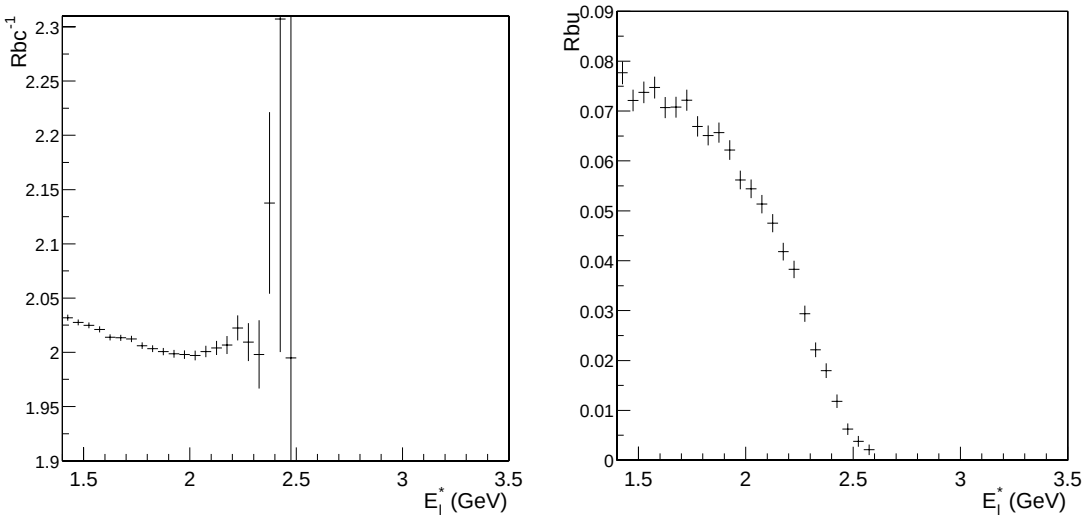

(a) (b)

Figure 5.3: (a) R_{bc}^{-1}, (b) R_{bu}. Both from Monte Carlo sample.

pendency. We will obtain $N_{SL}(E_l^*)$ and $N_{SL}(E_l^*,n_K^g)$ using mainly on data with some Monde Carlo input. $N_{SL}(E_l^*)$ can be obtained easily from background subtraction.

Denoting the number of reconstructed kaons in each event as n_K^{ev}, we obtain $N_{SL}(n_K^g)$ from $N_l(E_l^*,n_K^{ev})$ correcting for efficiency, faked kaons and kaon background from the second B in the event.

- the $\mathcal{E}$ matrix transforms $N_{SL}(E_l^*,n_K^g)$ to $N_{SL}(E_l^*,n_K^r)$, using Monte Carlo samples,
- the $\mathcal{F}$ matrix adds fake kaons to the reconstructed kaon distribution, using Monte Carlo samples,

- the $\mathcal{S}$ matrix adds the kaons from the second B mesons, using the inclusive samples.

Combining this three steps gives:

$$N_l(n_K^{ev}) = \mathcal{S} \cdot \mathcal{F} \cdot \mathcal{E} \cdot N_{SL}(n_K^g). \tag{5.5}$$

Having determined $N_{bu}(E_l^*)$, the partial branching fraction of $B \to X_u e\nu$ can be obtained by dividing $N_{bu}(E_l^*)$ with the electron efficiency and the total number of B mesons in the data set. The electron efficiency ϵ_e is defined in Eq. 2.13 using Monte Carlo sample.

Then the total branching fraction is calculated as explained in Section 2.4. The $|V_{ub}|$ is extracted with the total branching fraction, b quark mass and b quark lifetime measurements (Eq. 2.15).

5.2 Measurement of the semileptonic electron energy spectrum $N_{SL}(E_l^*)$

In the following sections, the criteria for electron reconstruction and selection are given to obtain electron sample. The high-energy electron is a signal for the semileptonic B decays. Thus their reconstruction is very important for this analysis.

5.2.1 Electron reconstruction and selection

From the list of the charged tracks (candidates with non-zero charge and pion mass hypothesis), the electrons are selected by the following criteria:

The likelihood-based method requires tracks to satisfy the following criteria to be identified as electrons:

- $0.88 < E/p < 1.3$,
- Number of crystals > 3,
- $0.1 <$ LAT (Lateral Shower Moment) < 0.6,
- $f_e \geq 0.95$, f_e is the likelihood fraction for electron.

The likelihood fraction for electron is computed by weighings the individual likelihoods with *a priori* probabilities p_η, where $\eta \in \{e; \pi; K; p\}$; $f_e = p_e \cdot \mathcal{L}(e) / \sum_\eta p_\eta \cdot \mathcal{L}(\eta)$, with $p_e : p_\pi : p_K : p_p = 1 : 5 : 1 : 0.1$ assumed [45].

When a candidate electron is paired with an opposite-sign electron and if the invariant mass of the pair is consistent with J/ψ mass ($2.5 < M_{e^+e^-} < 3.3\,\mathrm{GeV}/c^2$), the candidate electron is rejected.

5.2.2 Background subtraction

To obtain the semileptonic electron energy spectrum, the $B\overline{B}$ background and the continuum background should be removed[2]. The $B\overline{B}$ background is subtracted using the Monte Carlo samples. We use the off-peak data to describe the shape of the continuum background. However, since the amount of the off-peak data is about 12% of that of the on-peak data, the off-peak data should be scaled before the subtraction.

[2]The definition of each background can be found in Section 4

The off-peak data can be subtracted from the on-peak data too. However, the bin-by-bin subtraction of the off-peak data of the scaled distribution will amplify the statistical errors of the off-peak sample by a factor 8.55. To avoid this, we fit the shape of the off-peak data to smoothen the fluctuations. The continuum model which gives the best probability is the following:

$$f_c(p_0, \cdots, p_3; x) = \exp(p_0 + p_1 \cdot x) \cdot (1 + p_2 \cdot x + p_3 \cdot x^2), \tag{5.6}$$

where x is E_l^* and p_j are parameters. So, there are total 5 parameters in the fit; four parameters for the continuum function and one for $\xi_{\mathcal{L}}$. The $\xi_{\mathcal{L}}$ is also fitted because the error from the fit is smaller.

Due to the kinematics, all entries with $E_l^* \geq 2.8\,\mathrm{GeV}$ in the on-peak data cannot have any B mesons and thus they are all continuum background. We fit the on-peak data from 2.8 GeV to 3.5 GeV and the off-peak data from 1.1 GeV to 3.5 GeV together with a scale factor $\xi_{\mathcal{L}}$. The off-peak data is fitted from 1.1 GeV [3] to minimize uncertainties near 1.4 GeV. The fit function to be minimized (f_{fit}) is the following:

$$f_{fit} = \sum_{i=i_0}^{i_{max}} \chi^2_{off}(i) + \sum_{i=i_1}^{i_{max}} \chi^2_{on}(i), \tag{5.7}$$

$$\chi^2_{off}(i) = \frac{\Big(f_c(x_i) - N_{off}(x_i)\Big)^2}{N_{off}(x_i)}, \tag{5.8}$$

$$\chi^2_{on}(i) = \frac{\Big(\xi_{\mathcal{L}} \cdot f_c(x_i) - N_{on}(x_i) + N_{B\overline{B}}(x_i)\Big)^2}{N_{on}(x_i)}, \tag{5.9}$$

[3] All the plots show from 1.4 GeV only.

where x_i is $E_l^*(i)$, f_c is defined above, i_0 is the electron energy bin with center value 1.1 GeV, i_1 is that with 2.8 GeV, i_{max} is that with 3.5 GeV. N_{on} is the electron energy spectrum of the on-peak data, N_{off} is that of the off-peak data and $N_{B\overline{B}}$ is that of the $B\overline{B}$ background from Monte Carlo samples. This fit gives a χ^2 probability of 61.5%, and 8.70 for $\xi_{\mathcal{L}}$. The electron energy spectrum of the off-peak data, the scaled off-peak spectrum, the scaled continuum function, the scaled continuum function plus $B\overline{B}$ background, and the on-peak spectrum are shown in Fig. 5.4.

5.2.3 Result

The subtracted distribution is $N_{SL}(E_l^*)$:

$$N_{SL}(E_l^*) = N_{on}(E_l^*) - N_{B\overline{B}}(E_l^*) - \xi_{\mathcal{L}} \cdot f_c(p_0, \cdots, p_3; E_l^*), \tag{5.10}$$

where $\xi_{\mathcal{L}}$ and f_c are from the fit. The electron energy spectrum from semileptonic B mesons (N_{SL}) is shown in Fig. 5.5.

5.3 Measurement of $N_{SL}(E_l^*)$ as a function of the reconstructed kaon multiplicity $N_l(n_K^{ev})$

Mesons containing c quarks, X_c, are D, D^* and D^{**}. The exited D states, D^* and D^{**} mesons, decay into D almost 100%. So finding $B \to X_c e\nu$ modes is basically looking for D mesons from semileptonic decays. Due to the high branching fraction of $D \to K^{\pm}$ decay channels, the charged kaons are used as tags for D mesons. The branching fractions are [10]:

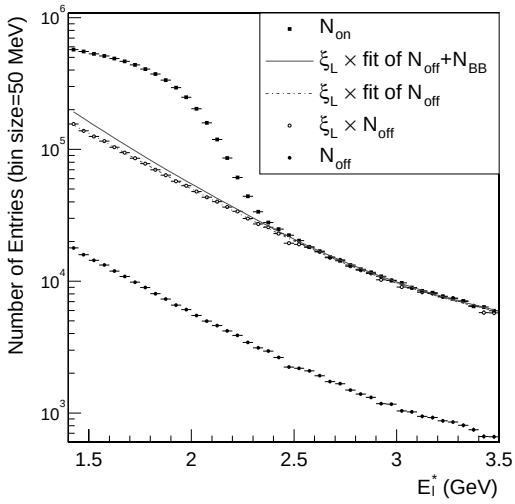

Figure 5.4: The electron energy spectrum. The closed square is the on-peak data, the closed circle is the off-peak data, the open circle is the scaled off-peak data by scale factor $\xi_{\mathcal{L}}$, the dashed line is the scaled fit of the off-peak data and the solid line is the $B\overline{B}$ background added to the dashed line.

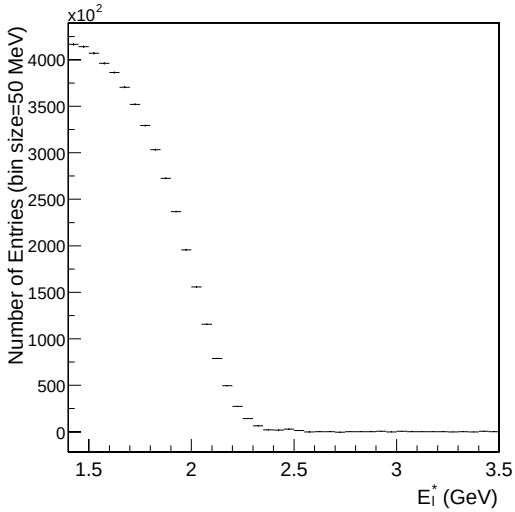

Figure 5.5: The electron energy spectrum of the off-peak and $B\overline{B}$ background subtracted on-peak data. Using the marker scheme of Fig. 5.4, this is the closed square minus the solid line.

Detector		Momentum (GeV/c)	Requirements
SVT	dE/dx	$0.025 < p < 0.7$, $p > 1.5$	> 3 dE/dx sample hits
DCH	dE/dx	$0.090 < p < 0.7$, $p > 1.5$	> 10 dE/dx hits
DIRC	# of Photons θ_C	$0.6 < p < 10$	Expected number of photons for electron > 0

Table 5.1: Minimal requirements applied to charged tracks for kaons.

- $\mathcal{B}(D^0 \to K^-$ anything$) = (53 \pm 4)\%$,
- $\mathcal{B}(D^0 \to K^+$ anything$) = (3.4 + 0.6\ -0.4)\%$,
- $\mathcal{B}(D^+ \to K^-$ anything$) = (27.5 \pm 2.4)\%$,
- $\mathcal{B}(D^+ \to K^+$ anything$) = (5.5 \pm 1.6)\%$.

The kaons can also directly come from $B \to X_u e\nu$ decays by hadronization. We use Monte Carlo samples to get the ratio of of $B \to X_u e\nu$ decays with and without charged kaons in the daughters (R_{bu} in Eq. 5.1) to correct this.

In the following sections the kaon reconstruction and selection, corrections and background subtraction are discussed.

5.3.1 Kaon reconstruction and selection

The kaon selection in *BABAR* is based on the information from the SVT, the DCH and the DIRC.

Among the charged particles satisfying criteria in Table 5.1, the ones passing the following additional criteria are chosen as kaons.

- $p_{SVT} < 0.6\,\mathrm{GeV}/c$, p_{SVT} is particle momentum in SVT,
- $p_{DCH} < 0.6\,\mathrm{GeV}/c$,
- $p_{DIRC} > 0.6\,\mathrm{GeV}/c$,
- $\mathcal{L}(K) > \mathcal{L}(p)$, $\mathcal{L}(x)$ is likelihood of particle x and is defined in [46],
- $\mathcal{L}(K) > r_\pi \mathcal{L}(\pi)$,

where r_π is 1 for $p < 2.7\,\mathrm{GeV}/c$[4], 80 for $p > 2.7\,\mathrm{GeV}/c$ and 15 for $0.5 < p < 0.7\,\mathrm{GeV}/c$. These criteria are optimized to keep the misidentification rate below 2% up to momenta of $4\,\mathrm{GeV}/c$, using the DIRC only at higher momenta.

5.3.2 Kaon efficiency correction

Since Monte Carlo samples are not yet optimally tuned to the data, some corrections need to be applied to the Monte Carlo samples. Two of these corrections are applied in this analysis: tracking efficiency correction and Particle Identification (PID) killing.

The Tracking Efficiency Correction

The tracking efficiency is measured for data and Monte Carlo samples for various conditions over time. The most significant such variations that impacts

[4]It does not matter which sub detector measured the momentum.

tracking efficiency are changes to the DCH high voltage setting. For 1999 and the first half of 2000, the voltage was set to 1900V, then raised to 1960V for the remainder of 2000. In 2001, the intermediate value of 1930V is used. The Tracking Efficiency Task Force has studied this in detail and provided a correction [47]. The result is applied to this analysis.

The PID Killing

This correction makes the Monte Carlo sample to reflect the data efficiency of particle selectors. PID Tables store the data efficiency and misidentification of the various particle selectors in bins of momentum, polar and azimuthal angles [48].

The Kaon PID Efficiency Correction

The kaon momentum distributions of data and Monte Carlo sample are shown in Fig. 5.6. Even after the tracking efficiency correction and the PID killing, the kaon momentum shows big difference between 0.5–0.8 GeV/c. To correct this, we measure the PID efficiency from a D control sample.

A control sample is a set of tracks where the type of the particle that caused the track is known from the topology of the respective event. Due to the large branching fraction of 3.8%, we choose the $D \to K\pi$ decay channel. We histogram the invariant masses of kaon-pion combinations and hadron-pion combinations as shown in Fig. 5.7. The hadrons are forced to have the kaon mass 0.493677 GeV/c^2 [10].

To estimate the number of D mesons, the sideband is used to estimate

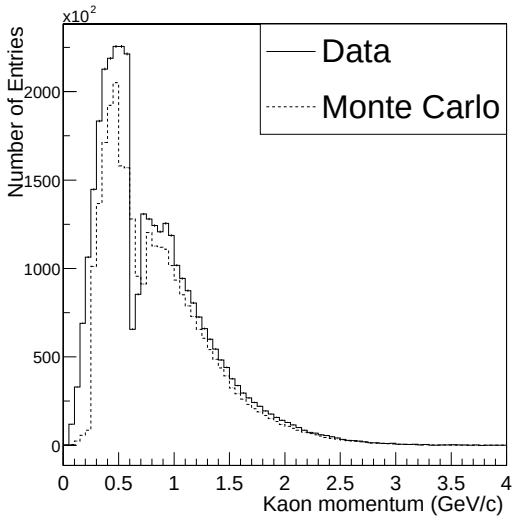

Figure 5.6: Kaon momentum distribution. The solid like is the kaons from data and the dotted line is the kaons from Monte Carlo samples.

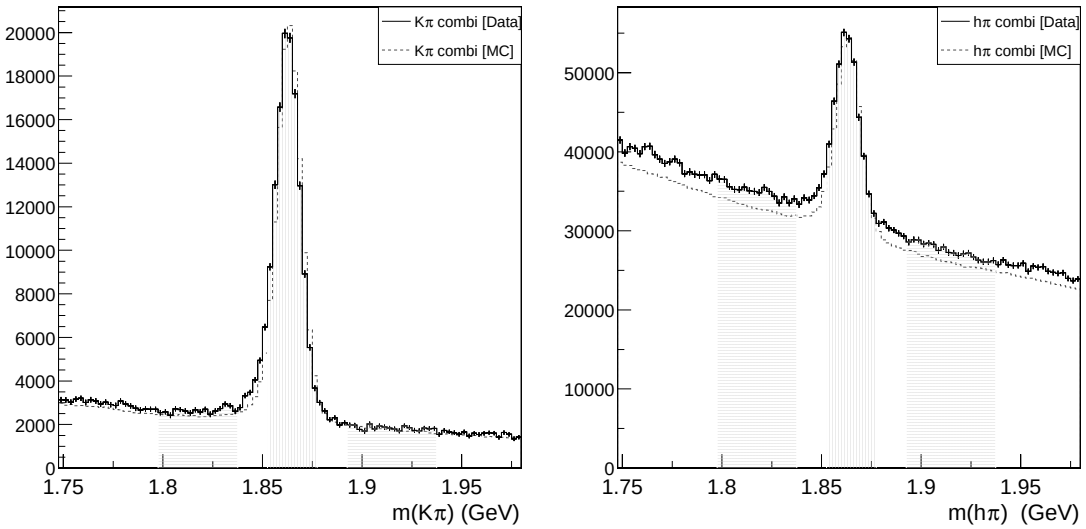

(a) (b)

Figure 5.7: (a) Invariant mass of kaon and pion combination. (b) Invariant mass of hadron and pion combination. The kaon mass is forced for hadrons. For both (a) and (b), the vertical lined area indicates the typical signal region and the horizontal lined areas are the typical side bands. See text for more detail.

the background of the control sample and to correct for it. This method is based on the assumption that the background is linear in the invariant mass distribution. The signal and sideband regions are shown in Fig. 5.7. The detail calculation can be found in Section A.1.

The number of D mesons is estimated by counting all entries in the signal region and subtracting the estimated background in the signal region. Then the particle identification efficiency (ϵ_{PID}) is defined as the number of D mesons from $K\pi$ combinations ($N_D^{K\pi}$) divided by that from $h\pi$ combinations ($N_D^{h\pi}$):

$$\epsilon_{PID} \equiv N_D^{K\pi}/N_D^{h\pi}. \tag{5.11}$$

For the systematic error calculation, the PID efficiency is calculated four more times:

- with the sideband regions increased by 10% at each end (ϵ_1),
- with the sideband regions decreased by 10% at each end (ϵ_2),
- with the signal region increased by 10% at each end (ϵ_3),
- with the signal region decreased by 10% at each end (ϵ_4).

If a region was (r_i, r_f), increasing it by 10% at each ends means that the region changed to $(r_i - 0.1 \times (r_f - r_i), r_f + 0.1 \times (r_f - r_i))$, and so on. The systematic error is calculated as following:

$$\text{systematic error} = 0.5 \cdot \left(\sqrt{\Sigma_+^2} + \sqrt{\Sigma_-^2} \right), \tag{5.12}$$

where

$$\Sigma_+^2 = \sum_{i=1}^{4} (\epsilon_{PID} - \epsilon_i)^2, \text{ if } \epsilon_{PID} < \epsilon_i, \tag{5.13}$$

$$\Sigma_-^2 = \sum_{i=1}^{4} (\epsilon_{PID} - \epsilon_i)^2, \text{ if } \epsilon_{PID} > \epsilon_i. \tag{5.14}$$

This is done for several kaon momentum ranges below $0.75\,\mathrm{GeV}/c$, and for one range above it. The sidebands and signal regions vary a little bit for each p_K bin.

The PID efficiencies, statistical errors and systematic errors for each kaon momentum bin are shown in Fig. 5.8. Due to the big error in the lowest bins, the PID efficiency measured in this method is trusted and applied only for $p_K > 0.45\,\mathrm{GeV}/c$. Because the reconstructed kaon distribution of data and Monte Carlo samples below $0.45\,\mathrm{GeV}/c$ are different from each other, their shapes are not a result of PID differences only, and we exclude kaons with $p_K < 0.45\,\mathrm{GeV}/c$. The final kaon momentum cut is 0.45–3.5 GeV/c.

We correct the Monte Carlo for the ratio:

$$c_p = \epsilon_{PID}^{Data} / \epsilon_{PID}^{MC}, \tag{5.15}$$

which are shown in Fig. 5.9.

5.3.3 Background subtraction

The $B\overline{B}$ background and the continuum background are subtracted from the on-peak electron energy spectrum for each number of kaons (n_K^{ev}) per

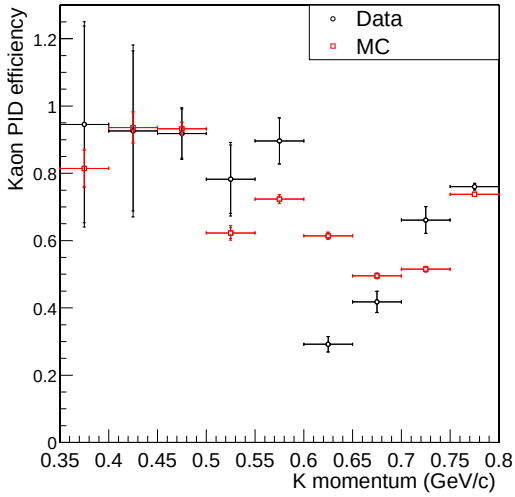

Figure 5.8: The kaon PID efficiency from the D control samples. The last bin covers all momentum ranges above $0.75\,\mathrm{GeV}/c$. The circle is data and the square is the Monte Carlo samples. The smaller error bars are statistical only and the bigger error bars are statistical and systematic combined.

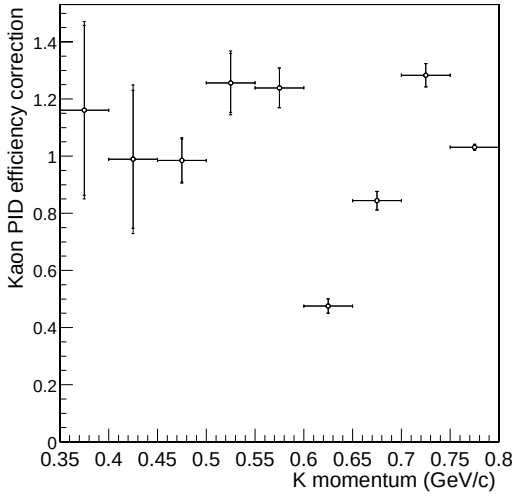

Figure 5.9: The kaon PID efficiency correction (c_p). The last bin covers all momentum ranges above $0.75\,\mathrm{GeV}/c$. The smaller error bars are statistical only and the bigger error bars are statistical and systematic combined.

event, in the same way for no kaon requirement case discussed in Section 5.2.2. We fit the off-peak electron energy spectrum and the on-peak data for each n_K^{ev} bin with the following empirical model:

$$f_c^k(p_0,\cdots,p_3;x_i) = \begin{cases} \exp(p_0+p_1\cdot x_i)\cdot(1+p_2\cdot x_i+p_3\cdot x_i^2), & \text{for } k\text{=0 or 1,} \\ \exp(p_0+p_1\cdot x_i+p_2\cdot x_i^2+p_3\cdot x_i^3), & \text{for } k\text{=2, 3 or 4,} \end{cases} \tag{5.16}$$

where p_j are p_{4k+j} to be precise. Due to the lack of entries, the fit is good up to n_K^{ev} =4 bin. Thus there are 21 parameters (5 n_K^{ev} bins $\times$ 4 fit parameters of continuum functions + 1 scaling factor) determined minimizing:

$$f_{fit} = \sum_{k=0}^{4}\left(\sum_{i=i_0}^{i_{max}}\chi^2_{off}(k,i)+\sum_{i=i_1}^{i_{max}}\chi^2_{on}(k,i)\right), \tag{5.17}$$

$$\chi^2_{off}(k,i) = \frac{\left(f_c^k(p_0,\cdots,p_3;x_i)-N^k_{off}(x_i)\right)^2}{N^k_{off}(x_i)}, \tag{5.18}$$

$$\chi^2_{on}(k,i) = \frac{\left(\xi_{\mathcal{L}}\cdot f_c^k(p_0,\cdots,p_3;x_i)-N^k_{on}(x_i)+N^k_{B\overline{B}}(x_i)\right)^2}{N^k_{on}(x_i)}, \tag{5.19}$$

where x_i is $E_l^*(i)$ and $N^k_{B\overline{B}}$ are $B\overline{B}$ background with k kaons in the event.

The fit gives χ^2 probabilities of 48.26%, 60.9%, 84.95%, 49.6% and 50.4% for n_K =0,1,...,4, respectively. The electron energy spectra of the on-peak data, the off-peak data and the continuum functions are shown in Fig. 5.10 and Fig. 5.11 for each n_K^{ev} bin.

5.3.4 Results

The subtracted distribution is:

$$N^k_{SL}(E^*_l) = N^k_{on}(E^*_l) - N^k_{B\overline{B}}(E^*_l) - \xi_{\mathcal{L}} \cdot f^k_c(p_{0+4k}, \cdots, p_{3+4k}; E^*_l), \qquad (5.20)$$

for each n^{ev}_K bin k (k=0,$\cdots$,4), as shown in Fig. 5.12 and Fig. 5.13.

5.4 Measurement of $N_{SL}(E^*_l)$ as a function of the generated kaon multiplicity $N_{SL}(E^*_l,n^g_K)$

After $B\overline{B}$ background and continuum subtraction as discussed in Section 5.3.3, each event has at least one semileptonic B mesons. Let n^{ev}_K be the reconstructed kaons in the event including fake kaons. What we want, as shown in Eq. 5.4, is the electron energy spectrum as a function of the number of kaon $N_{SL}(n^g_K)$ produced in the semileptonic B decays. Our goal, in this chapter, is to get from $N_l(n^{ev}_K)$ with the three steps discussed

1. The kaons from the second B mesons in events are removed using the $\mathcal{S}$ matrix: $\mathcal{S} \cdot N_{SL}(n^{r,f}_K) = N_l(n^{ev}_K)$, $n^{r,f}_K$ is the number of reconstructed kaons including fake kaons,

2. The fake kaons are removed using the $\mathcal{F}$ matrix: $\mathcal{F} \cdot N_{SL}(n^r_K) = N_{SL}(n^{r,f}_K)$, n^r_K is the number of reconstructed kaons including no fake kaons,

3. $N_{SL}(n^g_K)$ is from$N_{SL}(n^r_K)$ using the $\mathcal{E}$ matrix: $\mathcal{E} \cdot N_{SL}(n^g_K) = N_{SL}(n^r_K)$.

Here, these three steps are discussed in detail.

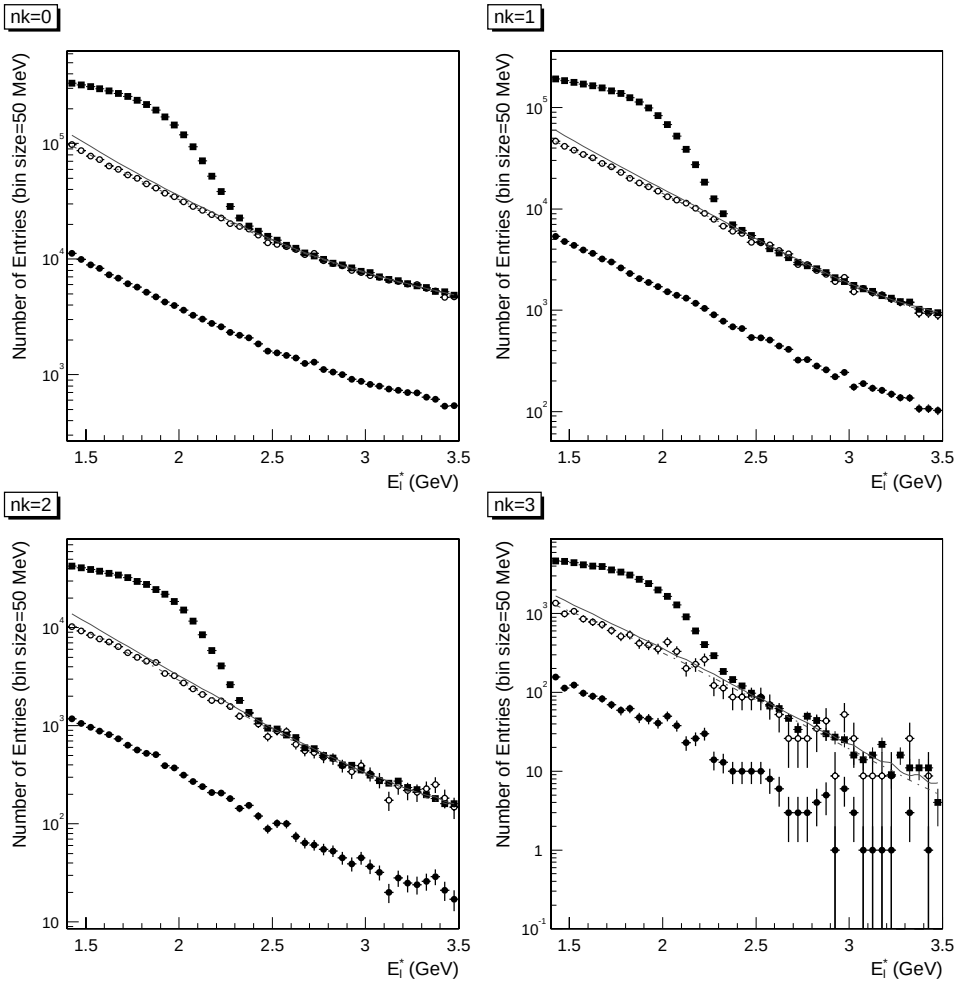

Figure 5.10: The electron energy spectra for each n_K bins. The marker schema is the same as in Fig. 5.4.

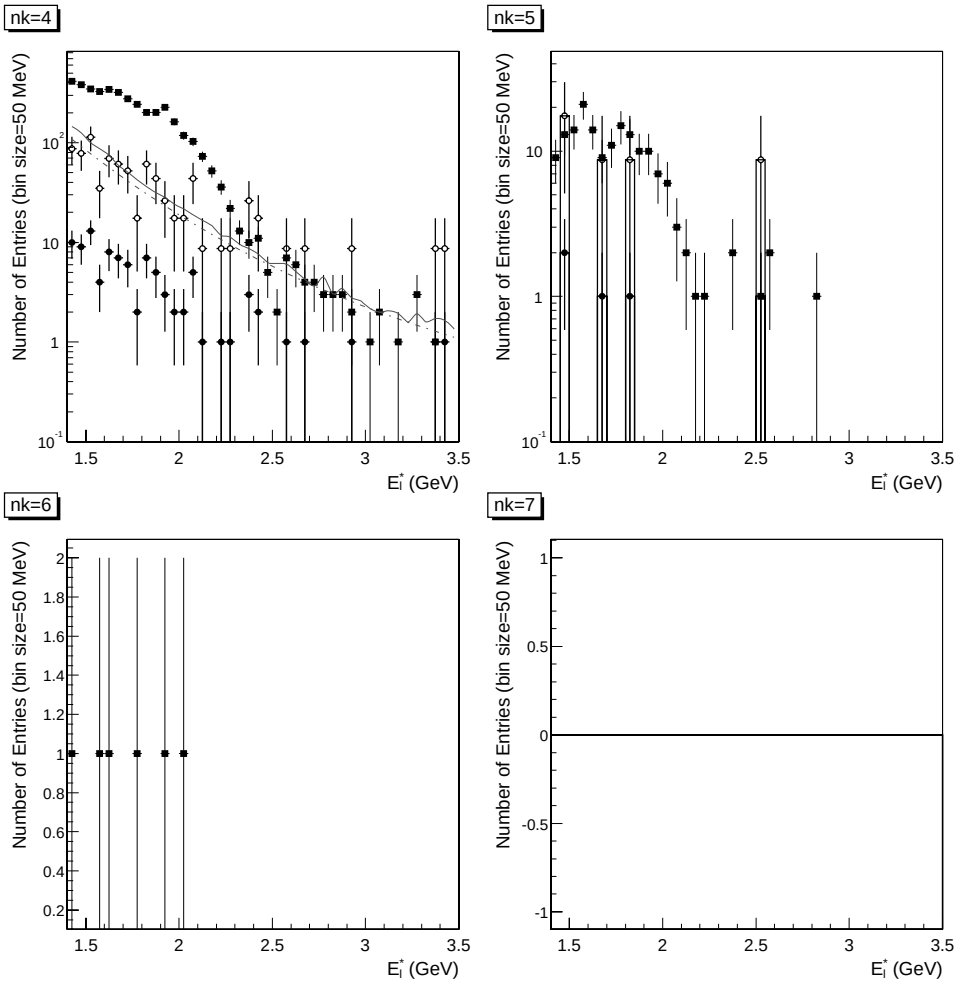

Figure 5.11: The electron energy spectra for each n_K bins. The marker schema is the same as in Fig. 5.4. Notice that the $n_K \geq 5$ bins are not fitted due to low statistics.

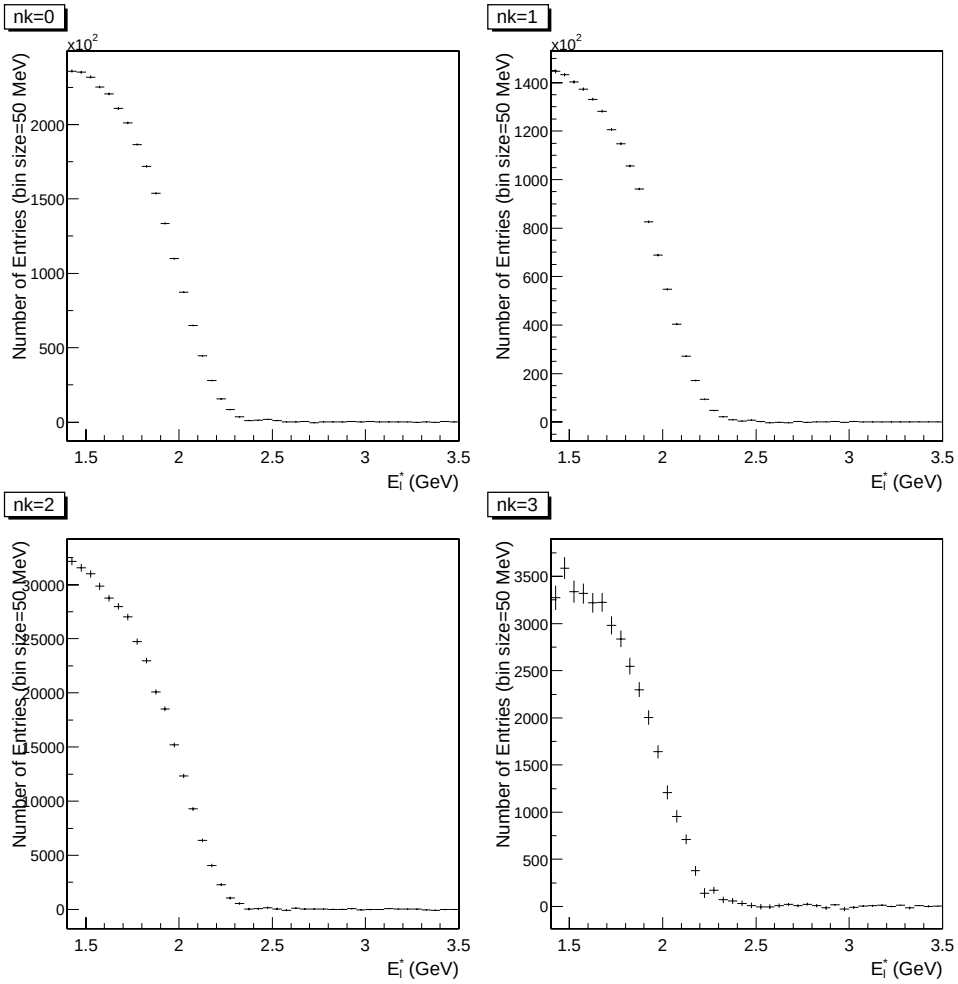

Figure 5.12: The electron energy spectra of the off-peak and $B\overline{B}$ background subtracted on-peak data, for each n_K bin.

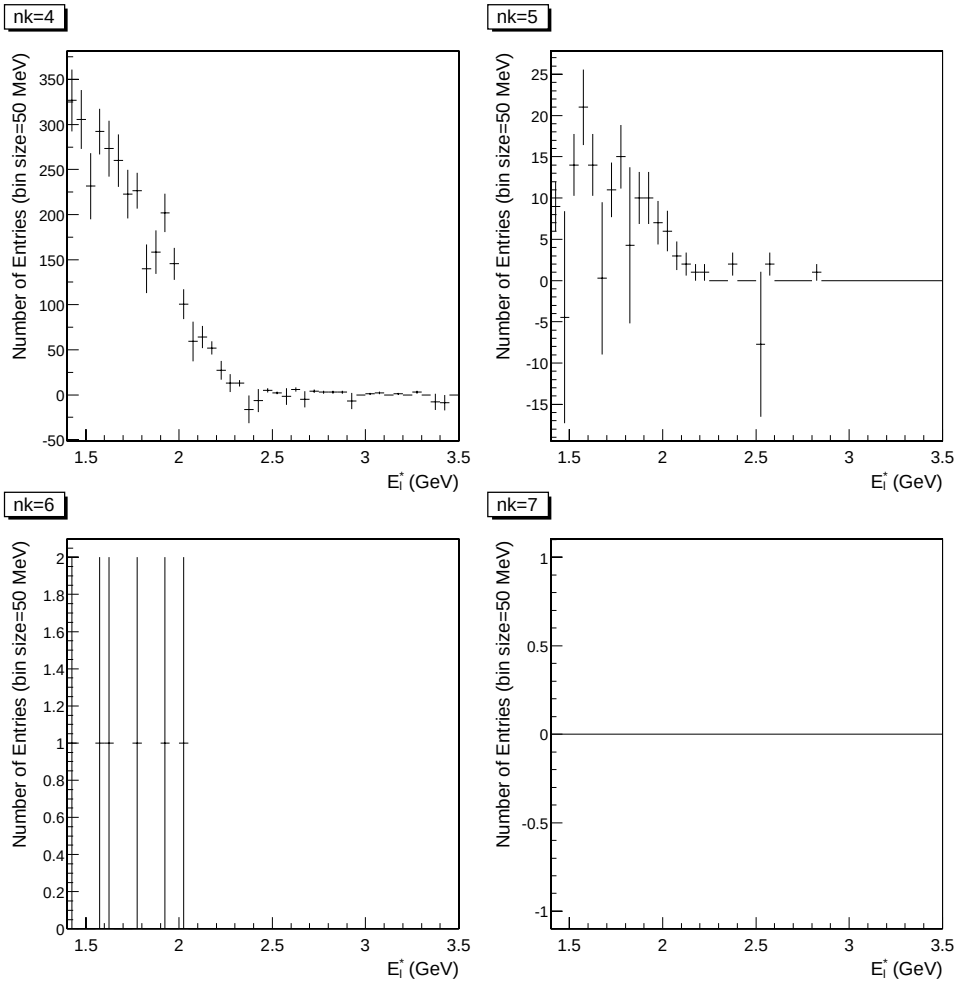

Figure 5.13: The electron energy spectra of the off-peak and $B\overline{B}$ background subtracted on-peak data, for each n_K bin.

5.4.1 Kaons from the second B mesons

The kaons in $N_l(n_K^{ev})$ can come from both B mesons in each event. We need to remove the kaons from the second B mesons. The relation between number of kaons per event is a summation:

$$n_K^{ev} = n_K^{r,f}(\text{from SL } B) + n_K^{r,f}(\text{from the second } B), \tag{5.21}$$

but that between distributions is a convolution:

$$N_l(E_l^*, n_K^{ev}) = g(n_K^B) \circ N_{SL}(E_l^*, n_K^{r,f}), \tag{5.22}$$

where $g(n_K^B)$ is the normalized kaon multiplicity distribution from the second B mesons. A normalization is required because the total number of electrons are same:

$$\sum_{n_K^{ev}=0} N_l(E_l^*, n_K^{ev}) = \sum_{n_K^{r,f}=0} N_{SL}(E_l^*, n_K^{r,f}) = N_{SL}(E_l^*). \tag{5.23}$$

The inclusive samples[5] can provide us $g(n_K^B)$. Because of no electron requirement, both B mesons in inclusive samples are same as the second B mesons in electron samples[6]. Assuming the two B mesons are independent, the kaon multiplicity distribution per event $N(n_K^{ev})$ is a convolution of $g(n_K^B)$ and itself

$$N(n_K^{ev}) = Ng(n_K^B) \circ g(n_K^B). \tag{5.24}$$

[5]The continuum background and $B\overline{B}$ background are subtracted bin-by-bin for the inclusive samples, with the scale factor determined from electron samples.

[6]They can decay into any possible modes while the semileptonic B mesons decay only into either $B \to X_u e\nu$ or $B \to X_c e\nu$.

The solution of this and more detailed discussions on convolution are given in Appendix B.

To test if the two B mesons are really independent, we compare the following two kaon multiplicity distributions:

- $g(n_K^B)$ from inclusive Monte Carlo samples using Eq. 5.24,
- the kaon multiplicity distribution from the second B mesons using electron Monte Carlo samples, $g(n_K^{B,sl})$.

The two kaon multiplicity distributions are shown in Fig. 5.14. The first bin shows about 0.048% difference which shows there is small correlations between semileptonic B mesons and the second B mesons. The correction $g(n_K^{B,sl})/g(n_K^B)$ is multiplied to $g(n_K^B)$ in data, assuming the data has the same amount of correlations between the two B mesons as the Monte Carlo sample. The distribution after the correlation fix is shown in Fig. 5.15.

The matrix $\mathcal{S}$ is given as:

$$\mathcal{S} = \begin{pmatrix} g(0) & 0 & 0 & 0 & \cdots & 0 \\ g(1) & g(0) & 0 & 0 & \cdots & 0 \\ g(2) & g(1) & g(0) & 0 & \cdots & 0 \\ \vdots & \vdots & \vdots & \vdots & \vdots & \vdots \\ g(9) & g(8) & g(7) & g(6) & \cdots & g(0) \end{pmatrix}, \tag{5.25}$$

for each electron energy bin. With this, we can rewrite Eq. 5.22 for each electron energy bin as following:

$$N_l(E_l^*, n_K^{ev}) = \mathcal{S}(E_l^*) \cdot N_{SL}(E_l^*, n_K^{r,f}). \tag{5.26}$$

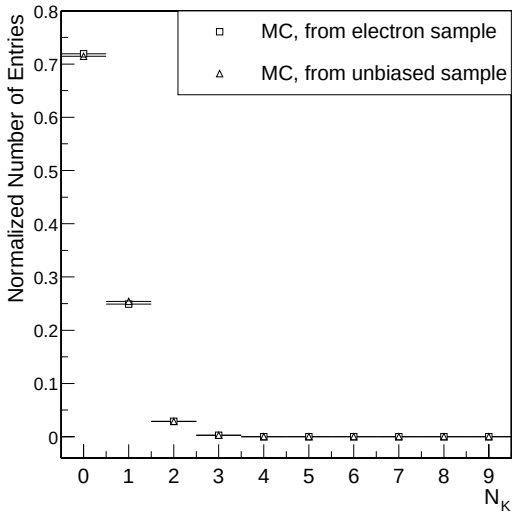

Figure 5.14: The normalized kaon multiplicity distributions $g(n_K^B)$. The square is from the electron Monte Carlo samples and the triangle is from the inclusive Monte Carlo samples.

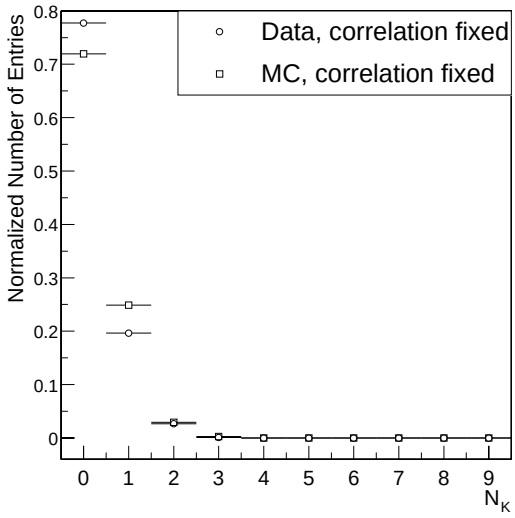

Figure 5.15: The normalized kaon multiplicity distributions after correlation fix. See text for the correlation fix. The circle is from data and the square is from Monte Carlo sample. The square is same as the square in Fig. 5.14.

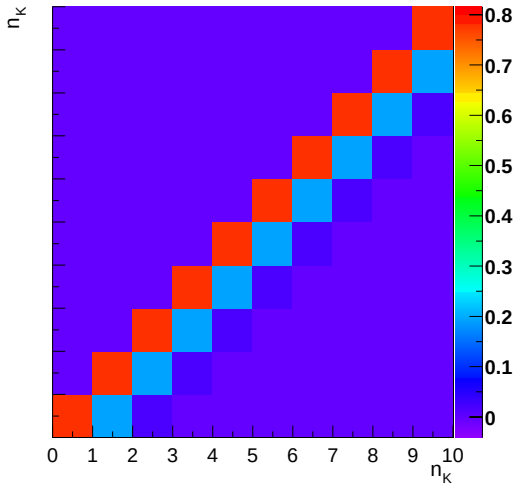

Figure 5.16: The $\mathcal{S}$ matrix.

The typical $\mathcal{S}(E_l^*)$ matrix is shown in Fig. 5.16. The variations on the matrices for each electron energy bin is very small.

5.4.2 Fake kaons

Particles which are not kaons can be reconstructed as kaons. They are called the fake kaons or fakes. From the Monte Carlo sample we may obtain the number of kaons including fakes from the semileptonic B mesons, $N_{SL}(n_K^{r,f})$, and the same but without fakes, $N_{SL}(n_K^r)$. From these, the $\mathcal{F}$ matrix is made.

Let $F(n_K^{r,f}, n_K^r)$ be the number of semileptonic B decays with $n_K^{r,f}$ kaons with fakes and n_K^r non-fake kaons. Let $f(n_K^{r,f}, n_K^r)$ be the normalized distribution:

$$f(n_K^{r,f}, n_K^r) = \frac{F(n_K^{r,f}, n_K^r)}{\sum_{n_K^{r,f}=0}^{9} F(n_K^{r,f}, n_K^r)}. \tag{5.27}$$

The matrix of $f(n_K^{r,f}, n_K^r)$ is the $\mathcal{F}$ matrix.

$$\mathcal{F}_{before} = \begin{pmatrix} f(0,0)| & 0 & 0 & 0 & \cdots & 0 \\ f(1,0)| & f(1,1) & 0 & 0 & \cdots & 0 \\ f(2,0)| & f(2,1) & f(2,2) & 0 & \cdots & 0 \\ f(3,0)| & f(3,1) & f(3,2) & f(3,3) & \cdots & 0 \\ \vdots & \vdots & \vdots & \vdots & \vdots & \vdots \\ f(9,0)| & f(9,1) & f(9,2) & f(9,3) & \cdots & f(9,9) \end{pmatrix} \tag{5.28}$$

The number of kaons from the semileptonic B meson is usually 0 or 1. But we still keep 10 n_K bins. So the $\mathcal{F}$ matrix has many zeros even at diagonal. This makes the $\mathcal{F}$ matrix not invertible. To fix this, we patch the second column of the $\mathcal{F}$ matrix to all the following columns. The second column is chosen because the numbers were fluctuating too much from the third column due to low statistics.

$$\mathcal{F}_{after} = \begin{pmatrix} f(0,0) & 0 & 0 & 0 & \cdots & 0 & 0 \\ f(1,0) & f(1,1) & 0 & 0 & \cdots & 0 & 0 \\ f(2,0) & f(2,1) & f(1,1) & 0 & \cdots & 0 & 0 \\ f(3,0) & f(3,1) & f(2,1) & f(1,1) & \cdots & 0 & 0 \\ \vdots & \vdots & \vdots & \vdots & \vdots & \vdots & \vdots \\ f(8,0) & f(8,1) & f(7,1) & f(6,1) & \cdots & f(1,1) & 0 \\ f(9,0) & f(9,1) & f(8,1) & f(7,1) & \cdots & f(2,1) & f(1,1) \end{pmatrix} \tag{5.29}$$

The fake multiplicity distribution is normalized so that the normalization of the electron energy spectrum remains same. The sum of all the $\mathcal{F}(E_l^*)$ matrices is shown in Fig. 5.17. The matrices for each electron energy bin can be found in Appendix A.2.

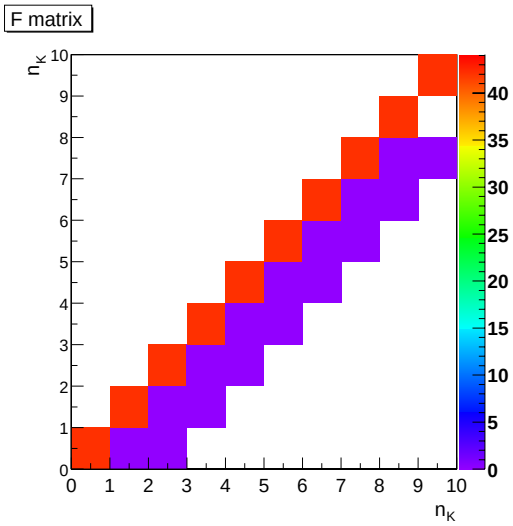

Figure 5.17: The $\mathcal{F}$ matrix. This is sum of 42 $\mathcal{F}$ matrices for all electron energy bins. There are some fluctuations at high n_K area. But there are no cases with so many kaons from semileptonic B mesons. So it does not really matter.

5.4.3 Kaon efficiency

The kaon efficiency matrix $\mathcal{E}$ can be obtained directly from the Monte Carlo samples in the same way as the fake matrix. Each matrix element $\mathcal{E}(g, r)$ is the normalized ratio of cases with g generated kaons and r reconstructed kaons.

The $\mathcal{E}$ matrix from the Monte Carlo sample is fitted for mean efficiency $\overline{\epsilon}$ assuming they follow the Binomial distribution. This is used to fix columns with too low statistics ($r < 50$) [7]. For example, if there is only one case

[7] The χ^2 probability for this fit is not good. It indicates the assumption of the Binomial distribution does not hold. That's why this is used only as a correction where there are not many event.

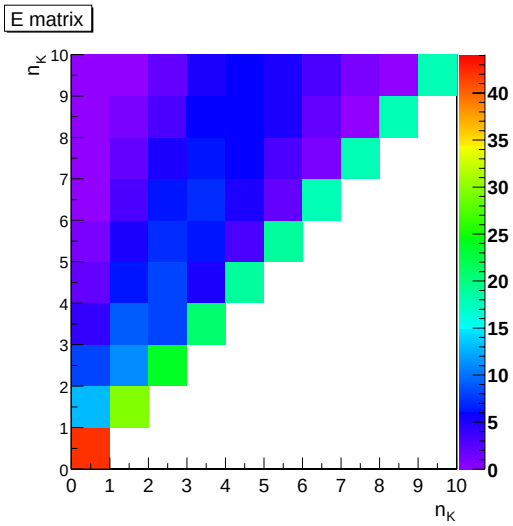

Figure 5.18: The $\mathcal{E}$ matrix. This is the sum of 42 $\mathcal{E}$ matrices for all electron energy bins.

of 4 generated and 2 reconstructed kaons, the column in $\mathcal{E}$ matrix would be (0,0,1,0,0). We replace this column with $((1-\overline{\epsilon})^4$, $\overline{\epsilon}\cdot(1-\overline{\epsilon})^3$, $\overline{\epsilon}^2\cdot(1-\overline{\epsilon})^2$, $\overline{\epsilon}^3\cdot(1-\overline{\epsilon})$, $\overline{\epsilon}^4)$. This is a small effect because these cases happen where there are not many kaons [8].

The sum of all the $\mathcal{E}(E_l^*)$ matrices is shown in Fig. 5.18. The matrices for each electron energy bin can be found in Appendix A.3.

From the relation:

$$N_l(E_l^*, n_K^{ev}) = \mathcal{S}\cdot\mathcal{F}\cdot\mathcal{E}\cdot N_{SL}(E_l^*, n_K^g), \tag{5.30}$$

by inverting the matrices, we get the electron energy spectra as a function

[8] For the high electron energy range, where there are no kaons, the matrix from the Monte Carlo sample is a zero matrix. This makes the $\mathcal{E}$ matrix not invertible. To fix this, if the matrix is a zero matrix, it is replaced with a unit matrix. Since there is no kaon, it does not make any difference in the analysis.

of produced kaon multiplicity from semileptonic B mesons from those as a function of reconstructed kaon multiplicity in each event:

$$N_{SL}(E_l^*, n_K^g) = (\mathcal{S} \cdot \mathcal{F} \cdot \mathcal{E})^{-1} \cdot N_l(E_l^*, n_K^{ev}). \tag{5.31}$$

5.5 Charmless electron energy spectrum

Our goal is to get $B \to X_u e\nu$ electron energy spectrum as already discussed in Eq. 5.4:

$$N_{bu}(n_K^g \geq 0) = \frac{N_{SL}(n_K^g \geq 0) - R_{bc}^{-1} \cdot N_{SL}(n_K^g \geq 1)}{1 - R_{bc}^{-1} \cdot R_{bu}}, \tag{5.32}$$

$$= \frac{N_{SL} - R_{bc}^{-1} \sum_{k=1}^{9} \Big((\mathcal{S} \cdot \mathcal{F} \cdot \mathcal{E})^{-1} \cdot N_{SL}(n_K^{r,f}; ev) \Big)(k)}{1 - R_{bc}^{-1} \cdot R_{bu}}. \tag{5.33}$$

If $R_{bc}^{-1} \cdot R_{bu}$ is small, this equation is $N_{bu} \approx N_{SL} - N_{bc}$. The N_{bc} part depends on R_{bc}^{-1} which is from the Monte Carlo samples. To minimize the Monte Carlo dependency, the magnitude of N_{bc} part is fitted with parameter α. To fit $B \to X_c e\nu$ spectrum against $B \to X_u e\nu$ and backgrounds, the $B \to X_u e\nu$ input is needed. Since this distribution from theory has about 2% error in the range of E_l^*=1.4–1.8 GeV, we use the shape of theoretical prediction.

The Monte Carlo samples and the theoretical calculation shows about 5% difference in shape, so instead of theory, we simply take the shape of the $B \to X_u e\nu$ spectrum from Monte Carlo samples. However, we fit the magnitude with parameter β, because we don't know it precisely.

In addition to this, we combine all the fit including the $B\overline{B}$ and off-peak subtraction (discussed in Section 5.2.2 and Section 5.3.3) altogether, to simplify the error propagation and to avoid having two scale factors from separate fits. We want all the fit parameters from one fit so that we can plug the fit values into Eq. 5.44. The fit function (f_{fit}) is consist of the off-peak part (χ^2_{off}) for continuum distribution, the on-peak part (χ^2_{on}) for scale factor $\xi_{\mathcal{L}}$, the model part (χ^2_{md}) for α and β. Here is f_{fit} to be minimized:

$$f_{fit} = \sum_{i=i_0}^{i_{max}} \chi^2_{off}(x_i) + \sum_{i=i_1}^{i_{max}} \chi^2_{on} \tag{5.34}$$

$$+ \sum_{i=i_2}^{i_3} \chi^2_{md} + \left(\frac{\beta - \mathcal{B}(B \to X_u e\nu)}{\sigma_{\mathcal{B}(B\to X_u e\nu)}} \right)^2, \tag{5.35}$$

where

$$\chi^2_{off} = \frac{(N_{off} - f_c)^2}{N_{off}}, \tag{5.36}$$

$$\chi^2_{on} = \frac{(N_{on} - N_{B\overline{B}} - \xi_{\mathcal{L}} \cdot N_{off})^2}{N_{on}}, \tag{5.37}$$

$$\chi^2_{md} = \frac{(N_{on} - f_{md})^2}{N_{on} + \sigma_f^2}, \tag{5.38}$$

with

$$f_{md} = N_{bc} + N_{bu} + N_{B\overline{B}} + \xi_{\mathcal{L}} N_{B\overline{B}} \tag{5.39}$$

$$\begin{aligned} &= \alpha \cdot R_{bc}^{-1} \Bigg(\sum_{k=1}^{k_{max}} (\mathcal{B} \cdot \mathcal{F} \cdot \mathcal{E})^{-1} (N^k_{on} - N^k_{B\overline{B}} - \xi_{\mathcal{L}} \cdot f^k_c) \\ &\quad - \frac{R_{bu} \cdot \beta N^{MC}_{bu}}{\mathcal{B}(B \to X_u e\nu)} \Bigg) + \frac{\beta \cdot N^{MC}_{bu}}{\mathcal{B}(B \to X_u e\nu)} + N_{B\overline{B}} + \xi_{\mathcal{L}} \cdot f_c, \end{aligned} \tag{5.40}$$

where N_{bu}^{MC} is the N_{bu} directly from the Monte Carlo samples. We take the shape of N_{bu}^{NC} but fit the normalization. Once again, we trust the shape at the low energy range due to the small uncertainties in the theory.

The error of f, σ_f^2, is defined as:

$$\sigma_f^2 = A \cdot T_{on} \cdot A^T, \tag{5.41}$$

where A and a 10×10 matrix T_{on} are defined as

$$A \equiv \alpha \cdot R_{bc}^{-1} \left(\sum_{k=1}^{k_{max}} (\mathcal{B} \cdot \mathcal{F} \cdot \mathcal{E})^{-1} \right), \tag{5.42}$$

$$T_{on}[i][j] = \begin{cases} N_{on}(x_i), & \text{if } i = j, \\ 0, & \text{elsewhere.} \end{cases} \tag{5.43}$$

The continuum functions f_c and f_c^k are already defined in Eq. 5.6 and Eq. 5.16. The bin numbers i_0 and i_1 are the bins with central E_l^* values 1.1 and 2.8, respectively, as defined in Section 5.2.2. The bin numbers i_2 and i_3 are the bins with central E_l^* values 1.4 and 1.8, respectively. The $\mathcal{B}(B \to X_u e\nu)$ used in the fit is a measured total $B \to X_u e\nu$ branching fraction from *BABAR* experiment; $\mathcal{B}(B \to X_u e\nu) = (2.2 \pm 0.5) \times 10^{-3}$.

The fit gives 72.5% probability with $\xi_{\mathcal{L}}$ =8.75±0.04, α =0.804 ± 0.004, β =(2.46 ± 0.48) × 10^{-3}. The final $B \to X_u e\nu$ electron energy spectrum is shown in Fig. 5.19.

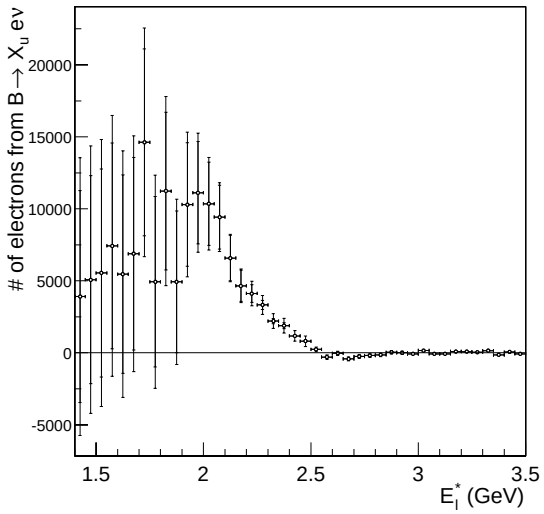

Figure 5.19: $B \to X_u e\nu$ electron energy spectrum. The small error bars are statistical only and the big error bars are statistical and systematic combined.

The final $B \to X_u e\nu$ electron energy spectrum is:

$$N_{bu}(E_l^*) = \frac{1}{1 - \alpha \cdot R_{bc}^{-1}(E_l^*) \cdot \beta \cdot R_{bu}(E_l^*)/\mathcal{B}(B \to X_u e\nu)} \times \Bigg[(N_{on} - N_{B\overline{B}})(E_l^*) - \xi_{\mathcal{L}} \cdot f_c(E_l^*) - \alpha \cdot R_{bc}^{-1}(E_l^*) \cdot \sum_{k'=1}^{9} \Bigg\{ (\mathcal{B} \cdot \mathcal{F} \cdot \mathcal{E})^{-1}(E_l^*) \cdot \Bigg((N_{on}^k - N_{B\overline{B}}^k)(E_l^*) - \xi_{\mathcal{L}} \cdot f_c^k(E_l^*) \Bigg) \Bigg\}(k') \Bigg], \tag{5.44}$$

where α, β, $\xi_{\mathcal{L}}$, f_c and f_c^k are from the fit.

The error matrix (V_{Nbu}) on N_{bu} is given as following:

$$V_{Nbu} = \left(\frac{\partial N_{bu}}{\partial p_i}\right) \cdot V_{cov} \cdot \left(\frac{\partial N_{bu}}{\partial p_i}\right)^T + \left(\frac{\partial N_{bu}}{\partial \mathcal{S}}\right) \cdot V_{\mathcal{S}} \cdot \left(\frac{\partial N_{bu}}{\partial \mathcal{S}}\right)^T, \tag{5.45}$$

where V_{cov} is the covariant matrix from the fit, p_i are the fit parameters and $V_{\mathcal{S}}$ is the error matrix of $\sum_{k=1}^{9} \mathcal{S}^{-1}$. This is statistical error only. The statistical

E_l^*(GeV)	Electron Efficiency
2.0 – 2.6	0.490
2.1 – 2.6	0.476
2.2 – 2.6	0.461
2.3 – 2.6	0.445

Table 5.2: The electron Efficiency.

errors of Monte Carlo samples are counted as systematic errors. Among the three matrices $\mathcal{S}$, $\mathcal{F}$, and $\mathcal{E}$, only $\mathcal{S}$ is made with data and the others are made with Monte Carlo sample. That is the reason why only errors of $\mathcal{S}$ matrix are counted as statistical errors.

The $B \to X_u e\nu$ branching fraction for each electron energy bin is calculated using the electron efficiency (ϵ_e) defined in Eq. 2.13 and summarized in Table 5.2. The statistical error of the electron efficiency is negligible and the systematic error on it is about 2%.

The electron efficiency for each energy bin shows a slope as shown in Fig. 5.20 due to the migration effect. The energy resolution of electrons shows that there is a big tail to the lower energy. The electrons produced at high energy near the end point can be reconstructed at lower energies but there are not many electrons produced at higher energy due to the kinematics. If we calculated the efficiency as function of the generated energy, then the efficiency is flat.

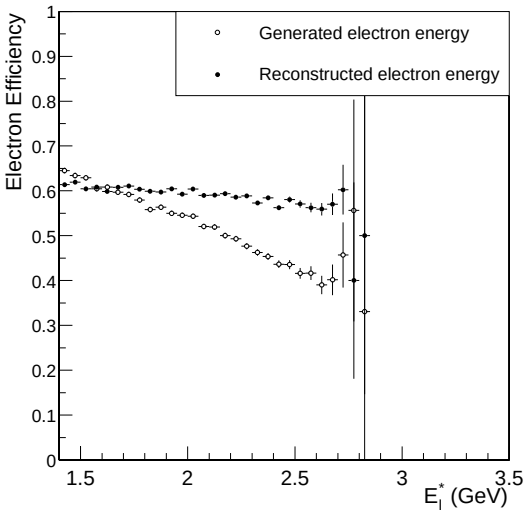

Figure 5.20: The electron efficiency from Monte Carlo sample. Due to the electron energy resolution, the efficiency as a function of the reconstructed electron energy has a slope. But the efficiency as a function of the generated electron energy is flat.

5.6 Systematic error study

The biggest systematic error sources, R_{bc}^{-1} and R_{bu}, and the systematic error sources on electron background in $B\overline{B}$ background and those on kaon background in $B\overline{B}$ ($n_K \geq 1$) are studied.

The kaon tracking efficiency correction and the kaon PID efficiency correction using D samples are discussed in Section 5.3.2. We start with the systematic errors from these in the next section.

5.6.1 Systematic error from the kaon efficiency corrections

There are uncertainties in the kaon tracking and PID efficiency corrections. These are considered as systematic errors. Let the kaon tracking

and PID efficiency correction factors be $c_t(p_k)$ and $c_p(p_k)$, respectively, as a function of kaon momentum p_k. And let their errors be $e_t(p_k)$ and $e_p(p_k)$, respectively. The values and error of the PID efficiency correction c_p and e_p are calculated in Section 5.3.2. The default correction factor is $c_t(p_k) \times c_p(p_k)$. The $B \to X_u e\nu$ electron energy spectrum with this default correction is N_{bu}. The analysis is repeated with the following correction factors:

- $(c_t + e_t)(p_k) \times c_p(p_k)$ [gives N^1_{bu}],
- $(c_t - e_t)(p_k) \times c_p(p_k)$ [gives N^2_{bu}],
- $c_t(p_k) \times (c_p + e_p)(p_k)$ [gives N^3_{bu}],
- $c_t(p_k) \times (c_p - e_p)(p_k)$ [gives N^4_{bu}].

The systematic errors from the kaon efficiency corrections on N_{bu} for each electron energy bin is calculated as following:

$$\text{systematic error} = 0.5 \cdot \left(\sqrt{\Sigma^2_+} + \sqrt{\Sigma^2_-} \right), \tag{5.46}$$

where

$$\Sigma^2_+ = \sum (N_{bu} - N^i_{bu})^2, \text{ if } N_{bu} < N^i_{bu}, \quad i = 1, 2, 3, 4, \tag{5.47}$$

$$\Sigma^2_- = \sum (N_{bu} - N^i_{bu})^2, \text{ if } N_{bu} > N^i_{bu}. \tag{5.48}$$

5.6.2 Systematic error from R^{-1}_{bc}

The magnitude of R^{-1}_{bc} is fitted and its error is counted as statistical error. The R^{-1}_{bc} is the ratio of all X_c meson decays to the X_c meson decays with

charged kaon produced. So it is sensitive to the uncertainties in $\mathcal{B}(B \to X_c e\nu)$ of each mode[9], in $\mathcal{B}(D^0 \to K^{\pm})$ and in $\mathcal{B}(D^+ \to K^{\pm})$.

We vary the branching fractions of all $B \to X_c e\nu$ decay modes by $\pm$ 1 sigma and also vary $D \to K^{\pm}$ branching fractions by $\pm$ 1 sigma. Let b_i to be the default branching fractions for each mode i and let e_i to be their errors. The analysis is repeated with $b_i + e_i$ and $b_i - e_i$. Then the systematic error is calculated in the same way as that from the kaon efficiency corrections.

5.6.3 Systematic error from R_{bu}

The relative systematic error on R_{bu} is estimated to be 50% because this is not well known. The systematic error from R_{bu} is calculated in the same way as that from R_{bc}^{-1}. The systematic error from R_{bu} is given as

$$\Delta N_{bu}(R_{bu}) = \sqrt{\left(\frac{\partial N_{bu}}{\partial R_{bu}}\right) \cdot M_{Rbu} \cdot \left(\frac{\partial N_{bu}}{\partial R_{bu}}\right)^T}, \tag{5.49}$$

where M_{Rbu} is a matrix with element $M_{Rbu}^{i,j} = \Delta_{Rbu}^i \cdot \Delta_{Rbu}^j$ and $\Delta_{Rbu}^i \equiv 0.5 \times R_{bu}(i)$, i and j are electron energy bins.

5.6.4 Systematic error from $B\overline{B}$ background

The following possible sources of systematic errors on electrons are studied for $B\overline{B}$ background. Each $B\overline{B}$ background category is shown in Fig. 5.21, Fig. 5.22 and Fig. 5.23. The relative systematic errors on each category are: [49]

[9] $B \to D$, $B \to D^*$ and $B \to D^{**}$

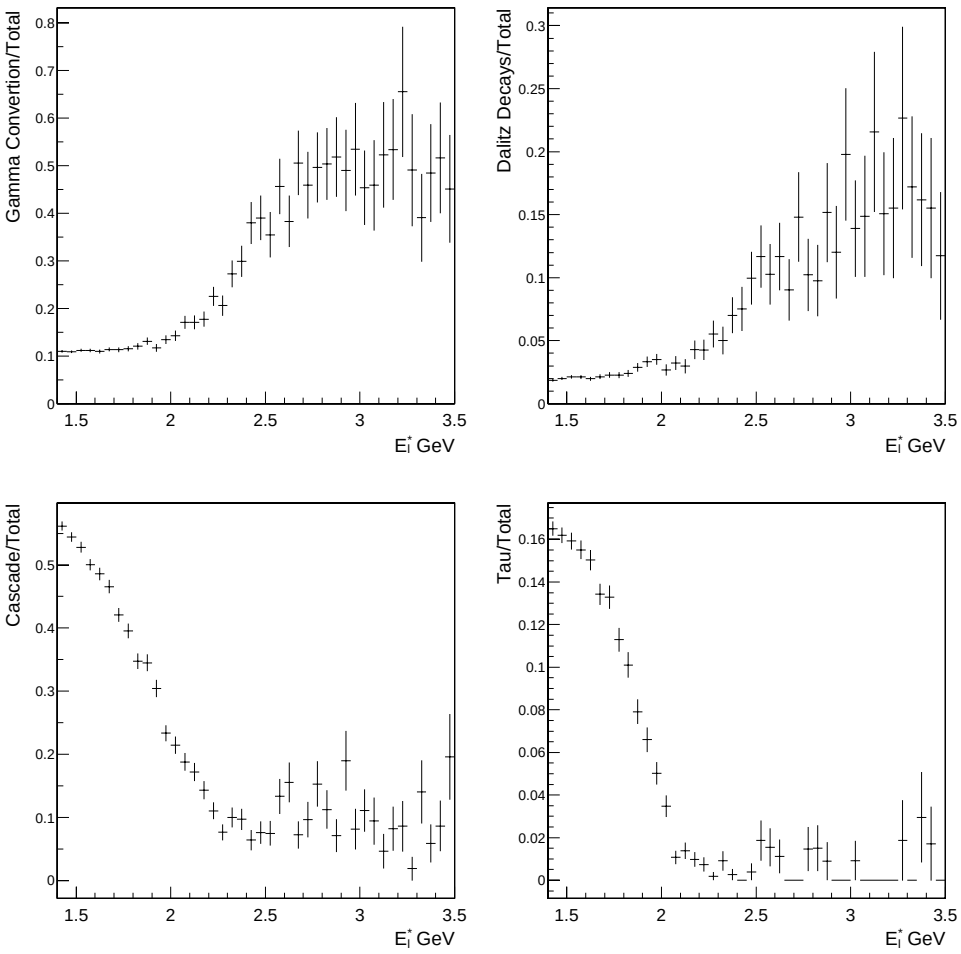

Figure 5.21: $B\overline{B}$ background in categories divided by the total $B\overline{B}$ background.

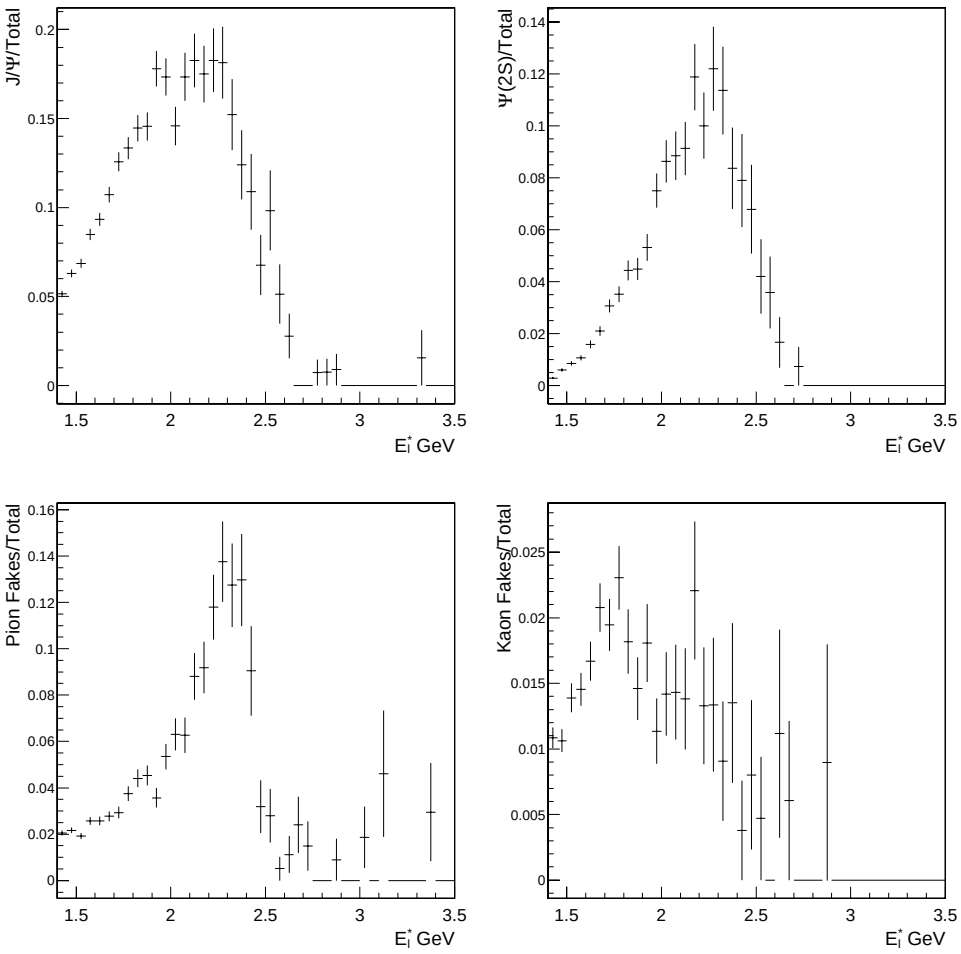

Figure 5.22: $B\overline{B}$ background in categories divided by the total $B\overline{B}$ background.

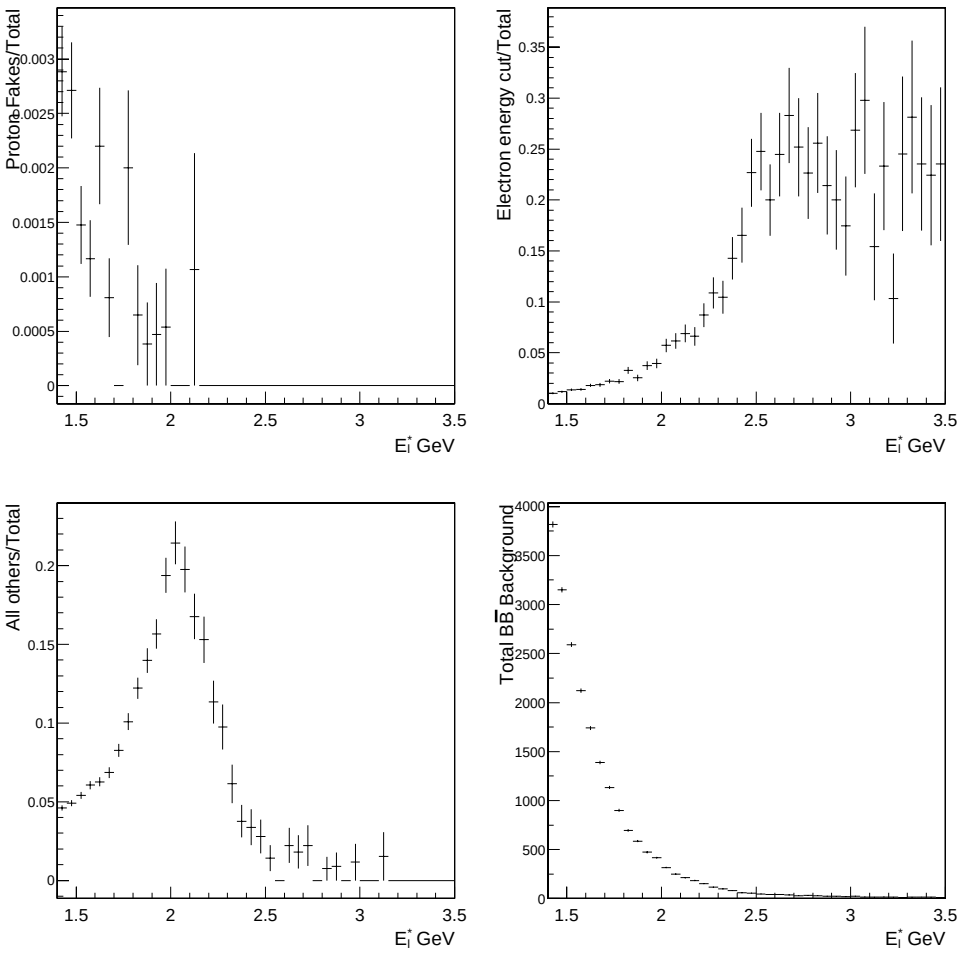

Figure 5.23: $B\overline{B}$ background in categories divided by the total $B\overline{B}$ background. The last plot is the total $B\overline{B}$ background.

- The systematic error on electron tracking efficiency about 0.7%,
- The mis-identification as electron
  - The relative systematic error on pion fake rate is about 3.5%,
  - The relative systematic error on kaon fake rate is about 15%,
  - The relative systematic error on proton fake rate is about 20%,
- Backgrounds
  - The relative systematic error on the electrons from gamma conversions is about 13%,
  - The relative systematic error on the electrons from Dalitz Decays is about 19%,
  - The relative systematic error on the electrons from cascade decays is about 25% [$\mathcal{B}(B \to \bar{c} \to e)$=(1.64± 0.37)%],
  - The relative systematic error on the electrons from τ decay is about 11.2% [$\mathcal{B}(B \to \tau^+ X, \tau^+ \to e^+ \nu e \bar{\nu} \tau)$=(0.565± 0.063)%],
- J/ψ , $\psi(2S)$:
  - The relative systematic error on the electrons from J/ψ is about 5.6% [$\mathcal{B}(B \to J/\psi \to e^+e^-$=(6.82± 0.38)$\times 10^{-4}$],
  - The relative systematic error on the electrons from $\psi(2S)$ is about 193.5% [$\mathcal{B}(B \to \psi(2S) \to e^+e^-$=(0.31± 0.6)$\times 10^{-4}$],

- The relative systematic error on all other sources is about 25%.

The systematic error from $B\overline{B}$ background is calculated as

$$\Delta N_{bu}(B\overline{B}) = \sqrt{\left(\frac{\partial N_{bu}}{\partial B\overline{B}}\right) \cdot \sum_{h} M_{B\overline{B}(h)} \cdot \left(\frac{\partial N_{bu}}{\partial B\overline{B}}\right)^{T}}, \tag{5.50}$$

where $M_{B\overline{B}(h)}$ is a matrix with element $M^{i,j}_{B\overline{B}(h)} = \Delta^{i}_{B\overline{B}(h)} \cdot \Delta^{j}_{B\overline{B}(h)}$ and

$$\Delta^{i}_{B\overline{B}(h)} \equiv \delta(h) \times B\overline{B}(h), \tag{5.51}$$

while $\delta(h)$ is the relative error in category h and i is the electron energy bin.

The relative systematic errors on partial branching fraction of $B \to X_u e\nu$ decay are summarized in Table 5.3.

5.7 Determination of the CKM element $|V_{ub}|$

The partial branching fraction for few E_l^* ranges are summarized with the F_u[10] in Table 5.4. The total branching fraction and the values and errors of $|V_{ub}|$ for few E_l^* ranges are calculated using Eq. 2.14 and Eq. 2.15, respectively, and summarized in Table 5.5. We choose $E_l^* = 2.1 - 0.26\,\mathrm{GeV}$ because the relative error of $|V_{ub}|$ is the smallest.

[10]This is already given in Table 2.1. Here it is shown again for convenience.

Error Source	2.0–2.6	2.1–2.6	2.2–2.6	2.3–2.6
Shape of R_{bc}^{-1}	17.953	12.125	6.114	2.455
R_{bu}	4.949	3.890	2.932	1.799
Efficiency Corrections	3.026	3.224	3.762	4.258
Electron Tracking Effieincy	0.800	0.800	0.800	0.800
Gamma Conversion	0.165	0.209	0.280	0.393
Dalitz Decays	0.054	0.072	0.103	0.148
Cascade Decays	0.271	0.229	0.224	0.241
Tau Decay	0.012	0.008	0.007	0.007
J/Ψ Decay	0.071	0.074	0.075	0.076
$\Psi(2S)$ Decay	1.464	1.777	1.929	2.199
π mis-ID	0.024	0.032	0.039	0.046
K mis-ID	0.016	0.018	0.021	0.021
p mis-ID	0.001	0.001	0.002	0.003
μ mis-ID	0.211	0.162	0.095	0.050
E_l^*(rec)-E_l^*(gen)>0.1 GeV cut	0.115	0.162	0.238	0.379
Other e background	0.047	0.049	0.063	0.090
Stat. Error on MC	0.233	0.233	0.240	0.252
Total	18.929	13.264	8.007	5.718

Table 5.3: Summary of systematic errors (%) on the branching fraction for $B \to X_u e\nu$.

E_l^*(GeV)	$\Delta\mathcal{B}$ (10^{-3})	F_u
2.0 – 2.6	0.714 $\pm$0.070 $\pm$0.135	0.278 $\pm$0.052
2.1 – 2.6	0.415 $\pm$0.040 $\pm$0.055	0.207 $\pm$0.046
2.2 – 2.6	0.231 $\pm$0.024 $\pm$0.019	0.137 $\pm$0.034
2.3 – 2.6	0.110 $\pm$0.016 $\pm$0.006	0.078 $\pm$0.022

Table 5.4: Results on the partial branching fraction ($\Delta\mathcal{B}$) for inclusive $B \to X_u e\nu$ decays and shape functions for four E_l^* intervals. First and second errors of $\Delta\mathcal{B}$ are statistical and systematic, respectively.

E_l^*(GeV)	$\mathcal{B}$ (10^{-3})	$\lvert V_{ub}\rvert$ (10^{-3})
2.0 – 2.6	2.57 $\pm$0.55 $\pm$0.48	4.80 $\pm$0.51 $\pm$0.45 $\pm$0.23
2.1 – 2.6	2.00 $\pm$0.33 $\pm$0.44	4.25 $\pm$0.35 $\pm$0.45 $\pm$0.20
2.2 – 2.6	1.68 $\pm$0.22 $\pm$0.42	3.89 $\pm$0.25 $\pm$0.48 $\pm$0.19
2.3 – 2.6	1.41 $\pm$0.22 $\pm$0.40	3.55 $\pm$0.28 $\pm$0.50 $\pm$0.17

Table 5.5: Results on the total branching fraction ($\mathcal{B}$) for inclusive $B \to X_u e\nu$ decays and $|V_{ub}|$ for four E_l^* intervals. First and second errors of $\mathcal{B}$ are experimental(stat.+sys.) and from F_u, respectively. Errors on $|V_{ub}|$ are experimental, F_u and theory, respectively.

Chapter 6

Conclusion

We measured the electron energy spectrum of the charmless semileptonic B meson decays by getting the spectrum of the charmed semileptonic decays using kaon tags. The total branching fraction of the charmless semileptonic B meson decays is:

$$\mathcal{B}(B \to X_u e\nu) = (2.00 \pm 0.33_{(exp)} \pm 0.44_{(F_u)})\%, \tag{6.1}$$

and the extracted $|V_{ub}|$ using the ratio (F_u) of the partial Branching Fraction over the total Branching Fraction from theory is:

$$|V_{ub}| = (4.25 \pm 0.35_{(exp)} \pm 0.45_{(F_u)} \pm 0.20_{(theo)}) \times 10^{-3} \tag{6.2}$$

The other inclusive $|V_{ub}|$ measurement are summarized in Fig. 6.1. The ones above line uses different theory frame work and thus can not be compared directly. The ones below line all use HQET to extract $|V_{ub}|$. The result of this analysis agrees with other measurements.

There are some things can be improved. To reduce Monte Carlo dependency in R_{bc}^{-1}, the neutral kaons can also be used as tags. There is a way to estimate R_{bc}^{-1} from data, if we know branching fractions of D meson to charged

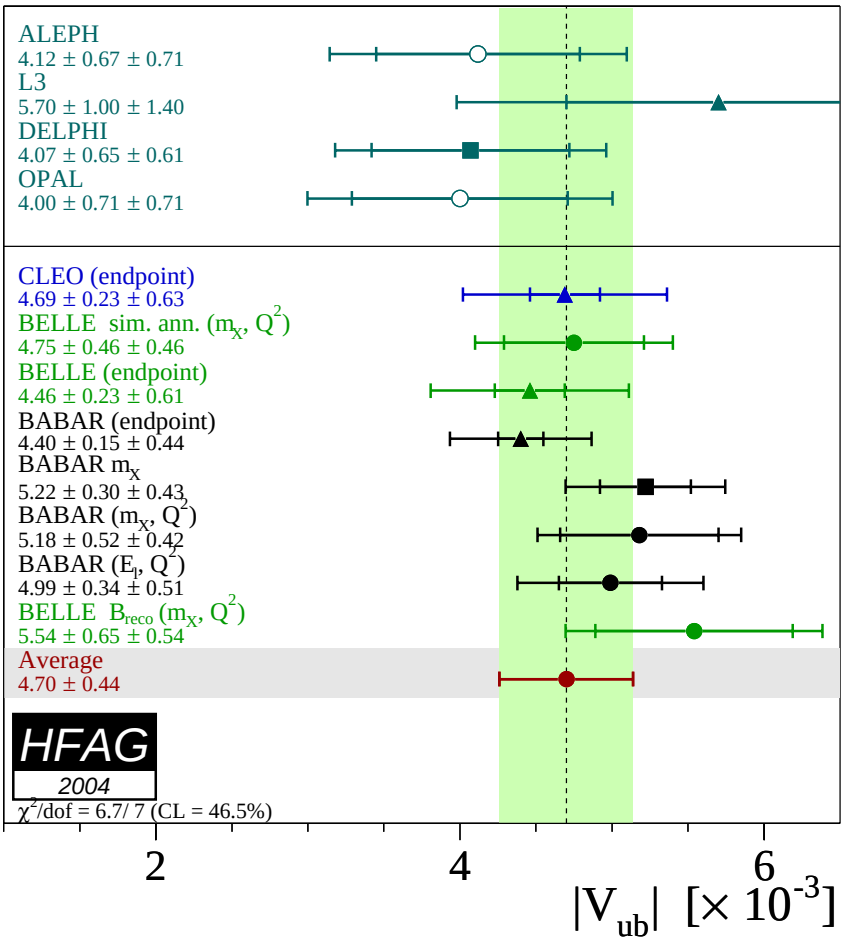

Figure 6.1: Other inclusive $|V_{ub}|$ measurements.

kaons precisely and the ratio of charged and neutral D mesons well:

$$\frac{N_{bc}}{N_{bc}(n_K^g \geq 1)} = \frac{(1-\mathcal{B}(D^0 \to K^+))N_{D^0} + (1-\mathcal{B}(D^+ \to K^+))N_{D^+}}{\mathcal{B}(D^0 \to K^+)N_{D^0} + \mathcal{B}(D^+ \to K^+)N_{D^+}} \tag{6.3}$$

,where D^0, D^+, K^+ denotes neutral D meson, charged D meson and charged kaons, respectively. This method gives R_{bc}^{-1} with too big error due to the big errors from the current branching fractions. So it was not used in this analysis.

The $B\overline{B}$ background is about 10% of the semileptonic spectrum and it is pure Monte Carlo input. The magnitude of each category of $B\overline{B}$ background can be fitted with signal and continuum background. This has not been tried in this analysis.

This analysis uses minimal Monte Carlo input and has a result agrees with the world average.

Appendices

Appendix A

Detail information and more plots

This appendix have some detail information which was not as important to put in the main text and many detail plots. The Bhabha event selection criteria are summarized in two tables; Table A.1 and Table A.2. These were used to reject so that we have non-Bhabha electrons.

A.1 The PID Efficiency

In this section, the calculation of PID efficiency using the D control sample is discussed in detail.

Let the sidebands be within the mass values of b_1^i, b_1^f and b_2^i, b_2^f, and the signal region be within s^i and s^f; $(b_1^i < b_1^f < s^i < s^f < b_2^i < b_2^f)$. The widths of the regions be w_{b1}, w_{b2} and w_s, respectively, and the distances between the regions be δ_1 and δ_2:

$$w_{b1} \equiv b_1^f - b_1^i, \qquad w_{b2} \equiv b_2^f - b_2^i, \qquad w_s \equiv s^f - s^i, \tag{A.1}$$

$$\delta_1 \equiv s^i - b_1^f, \qquad \delta_2 \equiv b_2^i - s^f. \tag{A.2}$$

If the background is linear and can be parameterized as $f(x) = \alpha x + \beta$, the

Cut Description	Cut Value
Good track criteria	
Maximum vertex $\lvert d_0^{IP}\rvert$	1.5 cm
Maximum vertex $\lvert z_0^{IP}\rvert$	10.0 cm
Minimum p_{cm}	0.25 GeV
Event criteria	
Number of good tracks	1
Minimum track $x = p_{cm}/(W/2)$	0.567
Minimum track θ	2.0
Maximum track-cluster $\lvert\Delta\phi\rvert$	0.1
Maximum track-cluster $\lvert\Delta\theta\rvert$	0.1
Minimum cluster $x = E_{cm}/(W/2)$	0.300
Minimum E_{cm}/p_{cm} (cluster/track)	0.650
Minimum θ for looser E_{cm}/p_{cm} cut	2.43
Looser minimum E_{cm}/p_{cm} (above a minimum θ)	0.300

Table A.1: Criteria for Bhabha 1 prong veto in Level-3 Trigger. $W/2$ is half the total CM energy, nominally 5.29 GeV at the $\Upsilon(4S)$.

number of background events in each region can be calculated as:

$$\mathcal{N}_1 = \frac{w_{b1}}{2}\Big(f(b_1^i) + f(b_1^f)\Big), \tag{A.3}$$

$$= \frac{w_{b1}}{2}\Big(f(s^i - \delta_1 - w_{b1}) + f(s^i - \delta_1)\Big), \tag{A.4}$$

$$= w_{b1}(\alpha s^i - \alpha\delta_1 + \beta - \frac{w_{b1}}{2}\alpha), \tag{A.5}$$

$$\mathcal{N}_2 = \frac{w_{b2}}{2}\Big(f(b_2^i) + f(b_2^f)\Big), \tag{A.6}$$

$$= w_{b2}(\alpha s^f + \alpha\delta_2 + \beta + \frac{w_{b1}}{2}\alpha), \tag{A.7}$$

$$\mathcal{N}_s = \frac{w_s}{2}\Big(f(s^i) + f(s^f)\Big), \tag{A.8}$$

$$= \frac{w_s}{2}(\alpha s^i + \alpha s^f + 2\beta), \tag{A.9}$$

where $\mathcal{N}_1$ and $\mathcal{N}_2$ are the numbers of background events in the sidebands and $\mathcal{N}_s$ in the signal region.

Cut Description	Cut Value
Good track criteria	
Maximum vertex $\lvert d_0^{IP}\rvert$	1.5 cm
Maximum vertex $\lvert z_0^{IP}\rvert$	10.0 cm
Minimum p_{cm}	0.25 GeV
Event criteria	
Number of good tracks	2
Minimum track $x = p_{cm}/(W/2)$	0.378
Minimum track $\sum x = \sum p_{cm}/(W/2)$	0.500
Maximum ϕ acolinearity in cms	0.10
Maximum θ acolinearity ($\lvert\theta_1 + \theta_2 - \pi\rvert$) in cms	0.20
Maximum — missing x - predicted missing x —	0.15
Maximum track-cluster $\lvert\Delta\phi\rvert$	0.1
Maximum track-cluster $\lvert\Delta\theta\rvert$	0.1
Minimum cluster $x = E_{cm}/(W/2)$	0.300
Minimum cluster $\sum x = \sum E_{cm}/(W/2)$	0.0
Minimum E_{cm}/p_{cm} (cluster/track)	0.650
Minimum θ for looser E_{cm}/p_{cm} cut	0.0
Looser minimum E_{cm}/p_{cm} (above a minimum θ)	0.000

Table A.2: Criteria for Bhabha 2 prong veto in Level-3 Trigger. $W/2$ is half the total CM energy, nominally 5.29 GeV at the $\Upsilon(4S)$.

After simple math, we have:

$$\mathcal{N}_s = \frac{w_s}{2}\left[\frac{\mathcal{N}_1}{w_{b1}} + \frac{\mathcal{N}_2}{w_{b2}} - \alpha(\delta_2 - \delta_1)\right]. \tag{A.10}$$

To avoid getting α, we choose δ_1 and δ_2 to be same. Then we may simply use the following equation:

$$\mathcal{N}_s = \frac{w_s}{2}\left[\frac{\mathcal{N}_1}{w_{b1}} + \frac{\mathcal{N}_2}{w_{b2}}\right]. \tag{A.11}$$

All the detail plots of $\mathcal{F}$ and $\mathcal{E}$ matrices for each electron energy bin are here.

A.2 The $\mathcal{F}$ matrices

All the $\mathcal{F}$ matrices for all the lepton energy bins are shown in Fig. A.1, Fig. A.2 and Fig. A.3.

A.3 The $\mathcal{E}$ matrices

All the $\mathcal{E}$ matrices for all the lepton energy bins are shown in Fig. A.4, Fig. A.5 and Fig. A.6.

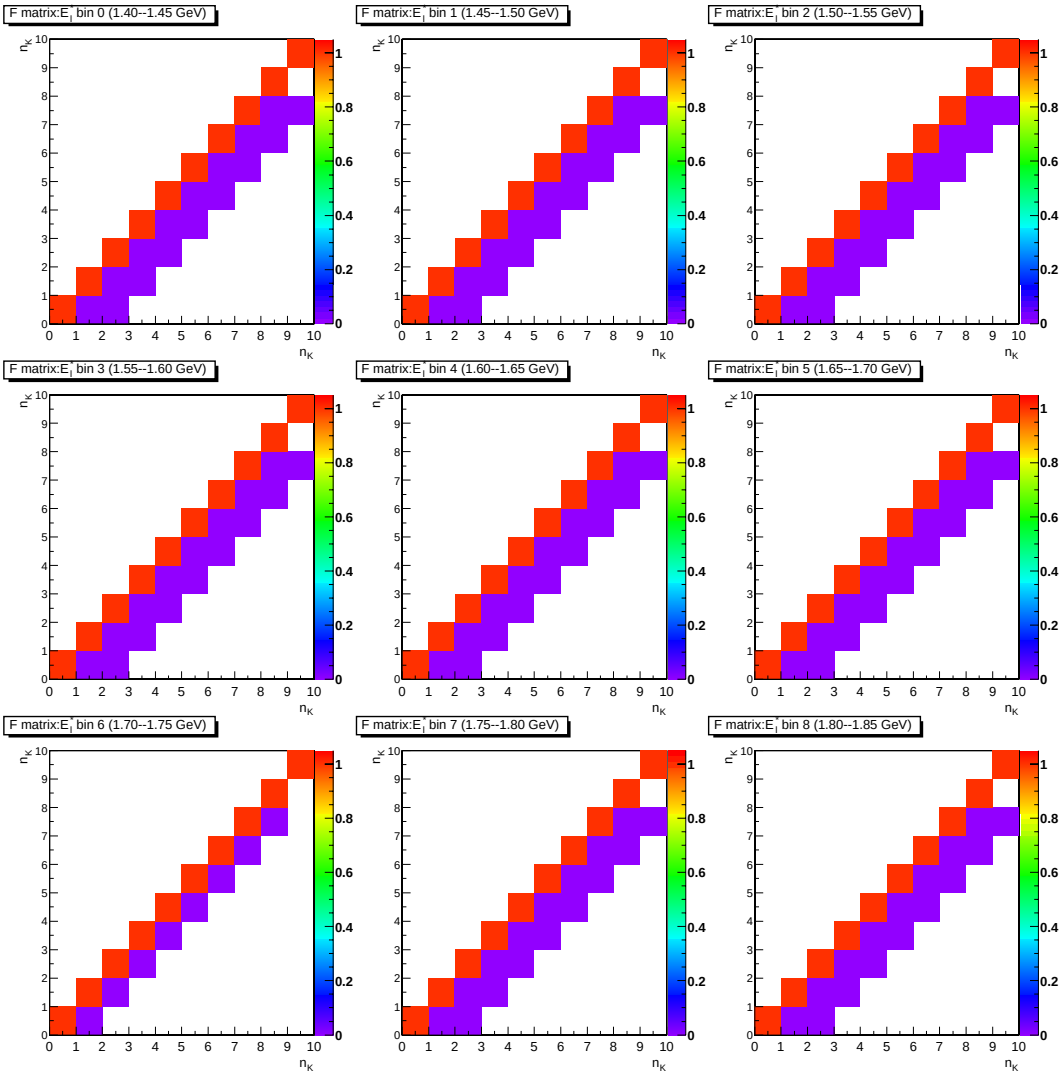

Figure A.1: The $\mathcal{F}$ matrices of the first 9 electron energy bins.

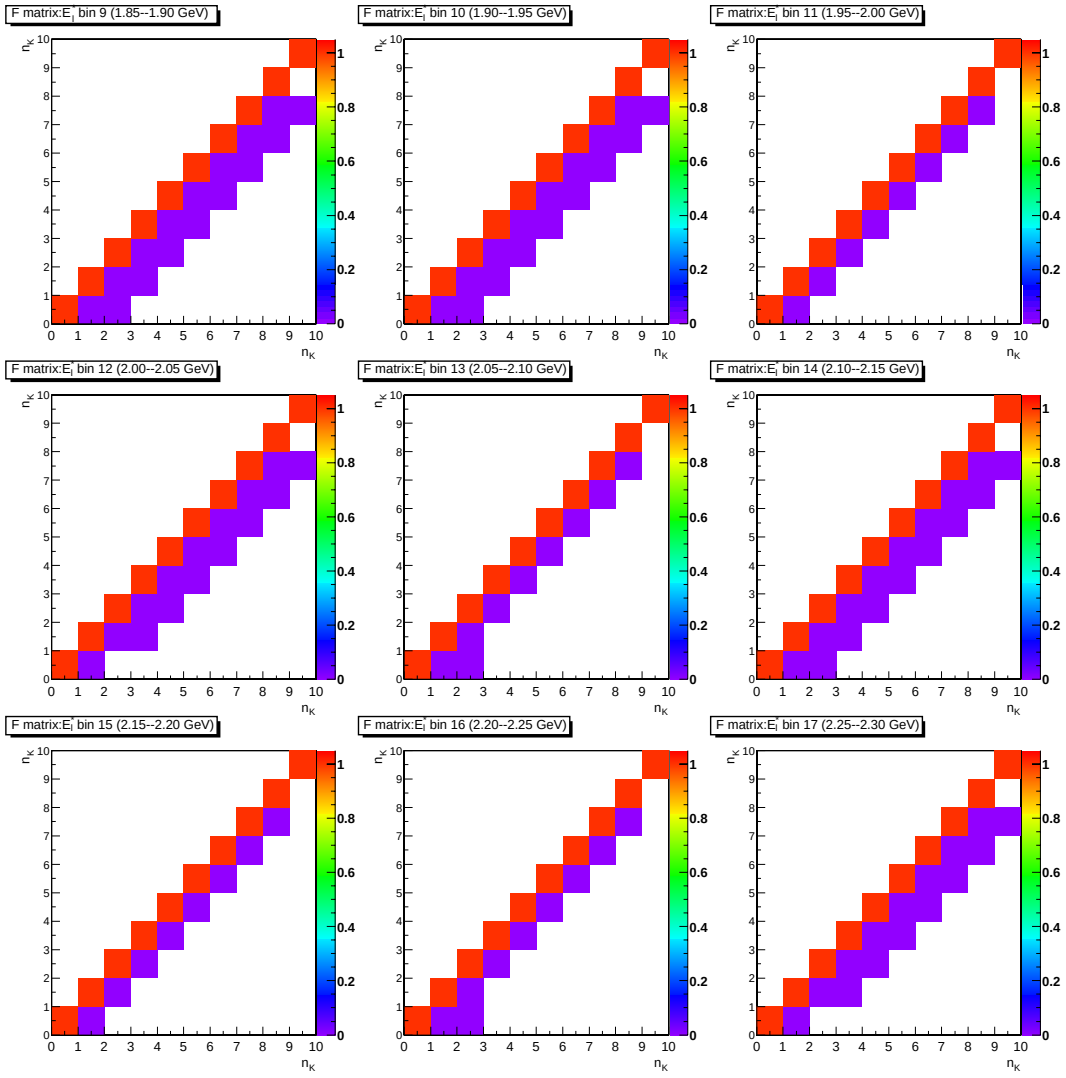

Figure A.2: The $\mathcal{F}$ matrices of the second 9 electron energy bins.

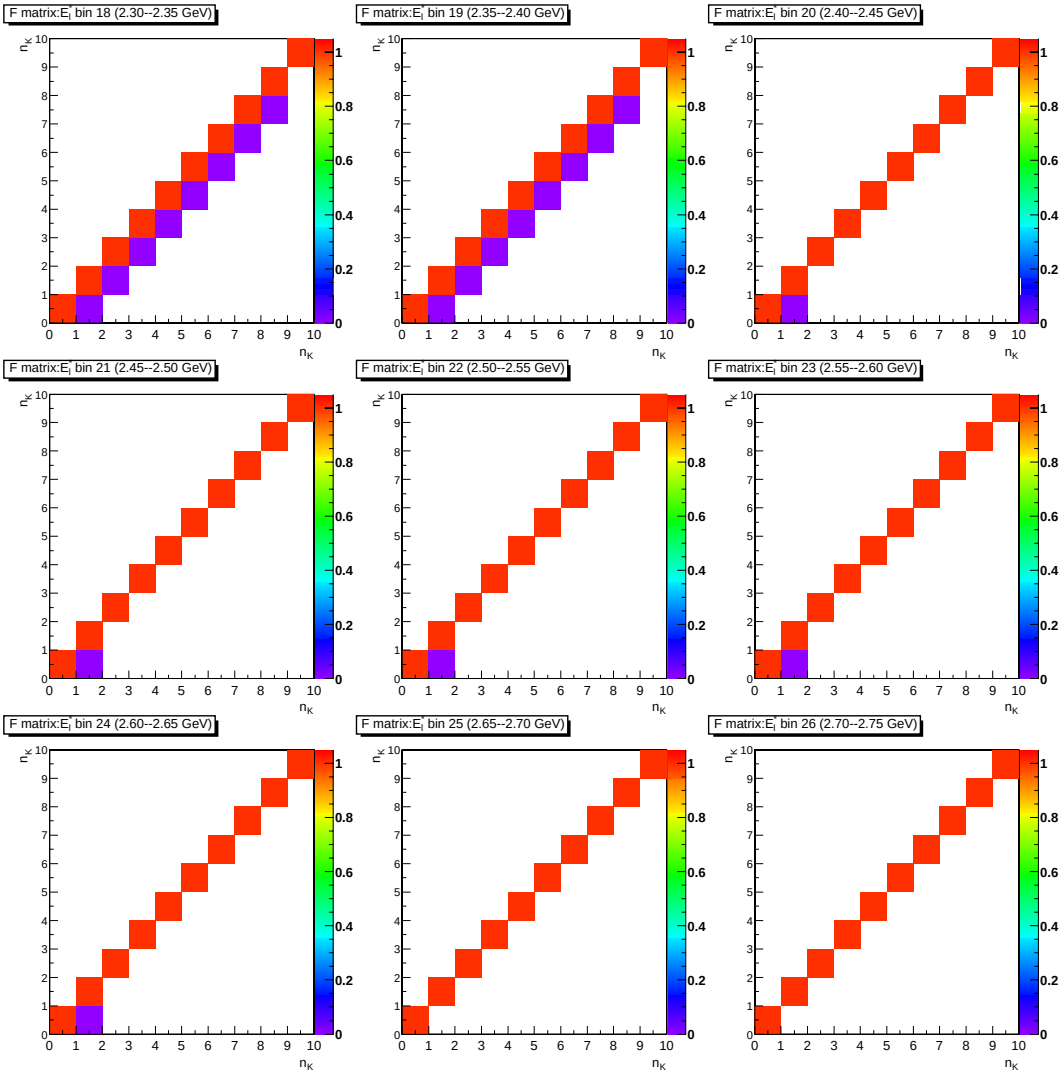

Figure A.3: The $\mathcal{F}$ matrices of the third 9 electron energy bins. The rest bins (which are not shown here) are all same the the last matrix.

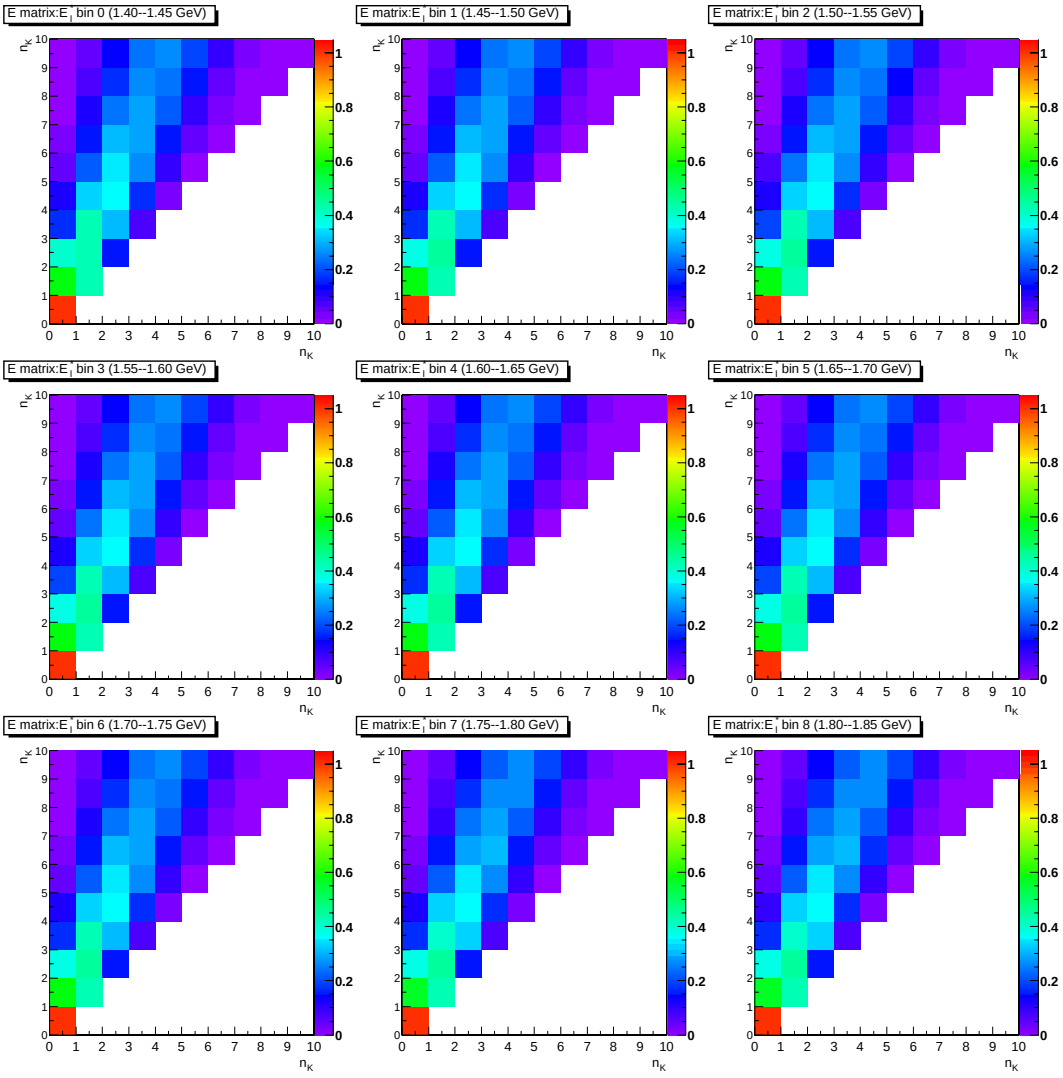

Figure A.4: The $\mathcal{E}$ matrices of the first 9 electron energy bins.

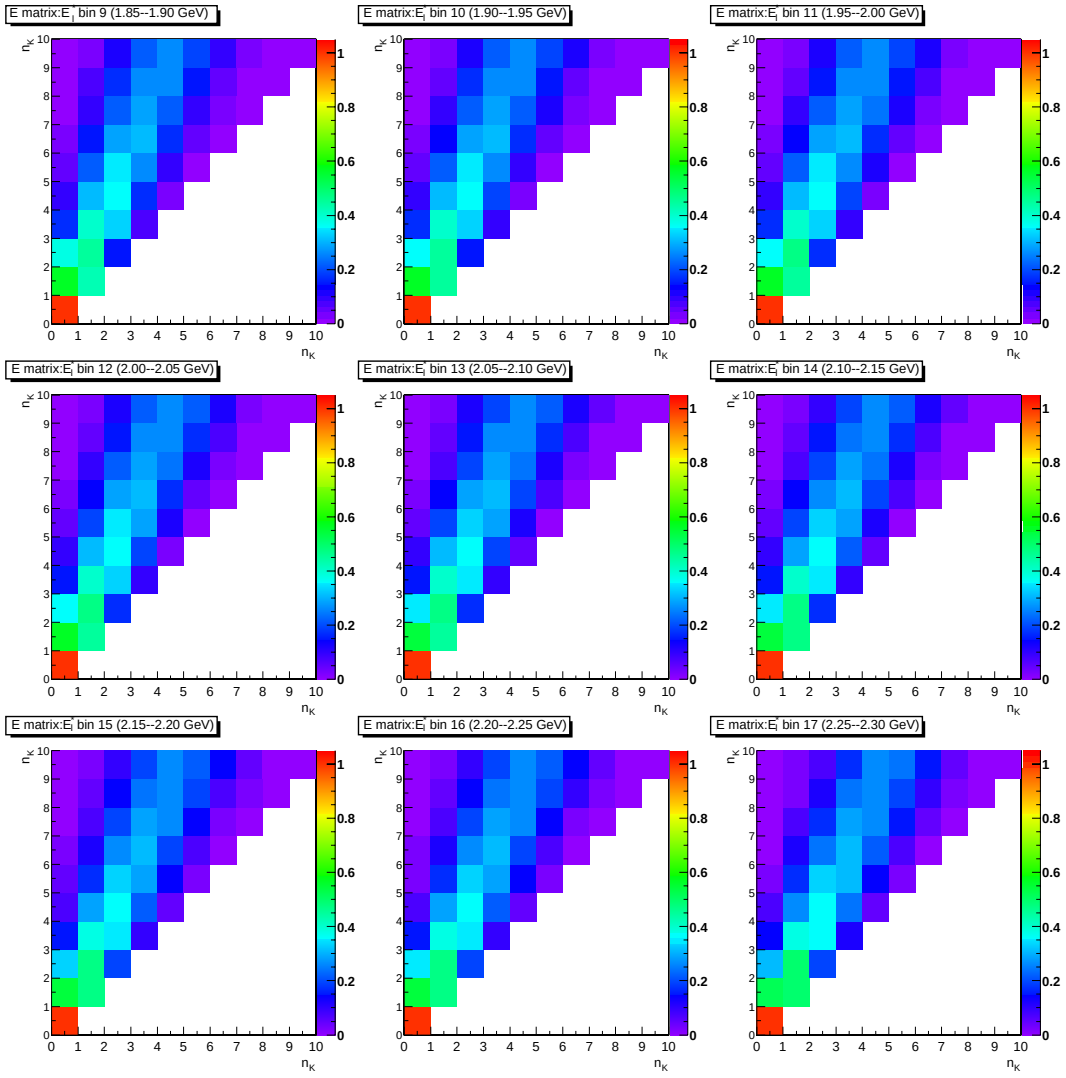

Figure A.5: The $\mathcal{E}$ matrices of the second 9 electron energy bins.

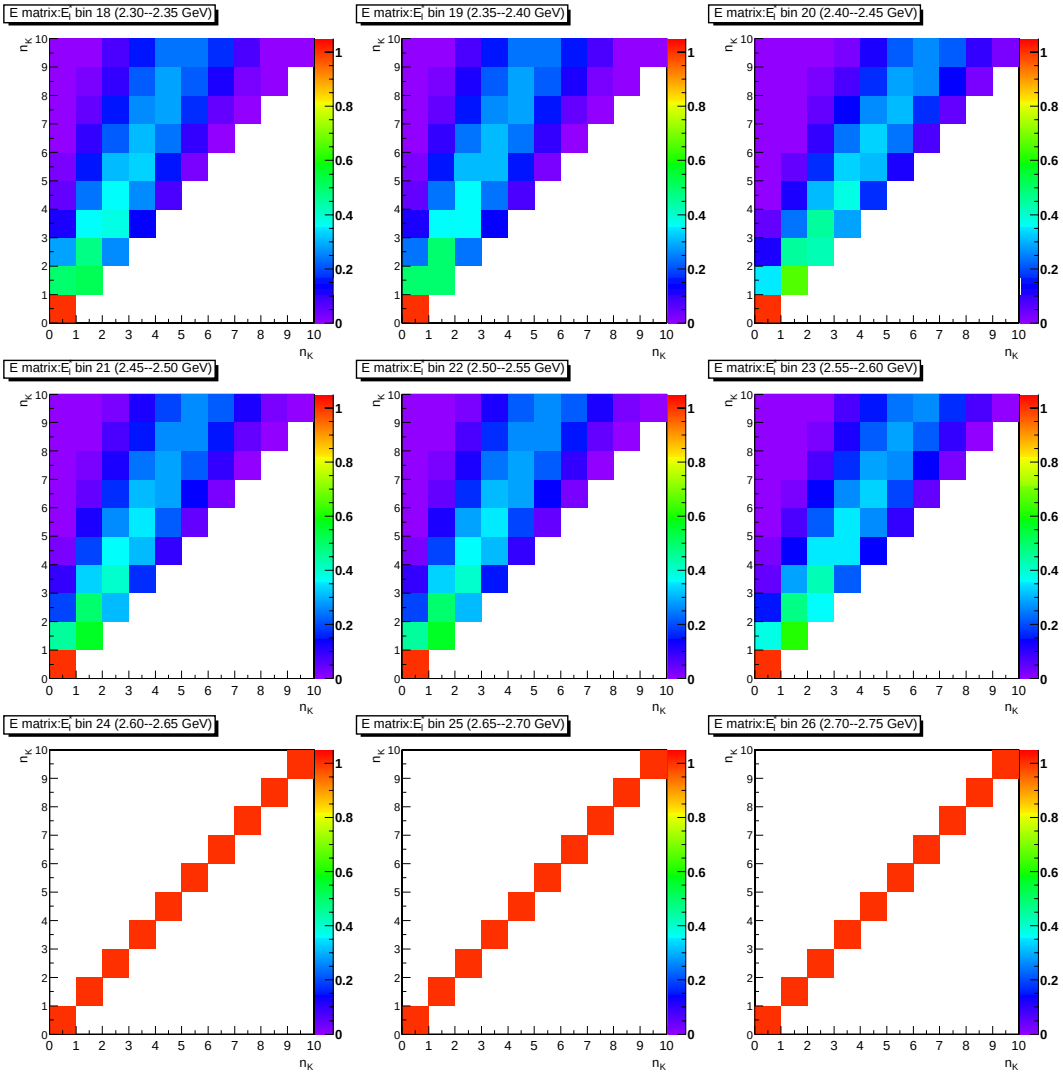

Figure A.6: The $\mathcal{E}$ matrices of the third 9 electron energy bins. The rest bins (which are not shown here) are all same the the last matrix.

Appendix B

Convolution, deconvolution and their errors

The convolution and deconvolution with their error calculation is explained here. It will be focus on the special cases this analysis uses than more general discussion. The special cases are:

1. The number of kaons is a positive discrete random variable.

2. We deconvolute the distribution of the sum of two independent variables.

3. The error of a convolution of two functions assumes they are correlated, This affects on the error propagation. This affects on the error propagation. This affects on the error propagation. This affects on the error propagation.because this is a test to see if the convolution of deconvoluted functions return the same values and errors, and they do.

B.1 Convolution of two different functions

The convolution of two functions f and g, F, is defined as:

$$F_k \equiv (f \circ g)_k = \sum_{k'=0}^{k} f_{k'} \cdot g_{k-k'}, \tag{B.1}$$

$$F_0 = f_0 \cdot g_0, \tag{B.2}$$

$$F_1 = f_0 \cdot g_1 + f_1 \cdot g_0, \tag{B.3}$$

$$F_2 = f_0 \cdot g_2 + f_1 \cdot g_1 + f_2 \cdot g_0, \tag{B.4}$$

$$\cdots, \tag{B.5}$$

The physical meanings are: F_k is the number of events with k kaons, f'_k is that of one type of B mesons with k' kaons and $g_{k-k'}$ is that of the other type of B mesons with k-k' kaons. The one type of B mesons can mean semileptonically decaying ones, the other type of B mesons can mean inclusively decaying ones, in case the events are tagged with one lepton.

The error matrix of F, V_F, is given like following, with a covariance matrix of f, V_f, and of g, V_g:

$$V_F = A \cdot V_f \cdot A^T + B \cdot V_g \cdot B^T + A \cdot V_{fg} \cdot B^T + B \cdot V_{gf} \cdot A^T, \tag{B.6}$$

where a matrix A is defined as following:

$$A_{ij} = \partial F_i / \partial f_j \tag{B.7}$$
$$= \sum_{k=0}^{i} \partial f_k / \partial f_j \cdot g_{i-k} \tag{B.8}$$
$$= \sum_{k=0}^{i} \delta_{k,j} \cdot g_{i-k} \tag{B.9}$$
$$= g_{i-j}, \tag{B.10}$$

and a matrix B is defined as following:

$$B_{ij} = \partial F_i / \partial g_j \tag{B.11}$$
$$= \sum_{k=0}^{i} f_k \cdot \partial g_{i-k} / \partial g_j \cdot \tag{B.12}$$
$$= \sum_{k=0}^{i} f_k \cdot \delta_{i-k,j} \tag{B.13}$$
$$= f_{i-j} \cdot \tag{B.14}$$

B.2 Deconvolution of two different functions

The deconvolution of f from $F = f \circ g$ is defined as:

$$f_k \equiv (F \circ^{-1} g)_k = \frac{1}{g_0} \left(F_k - \sum_{k'=0}^{k-1} f'_k \cdot g_{k-k'} \right), \tag{B.15}$$
$$f_0 = \frac{F_0}{g_0}, \tag{B.16}$$
$$f_1 = \frac{F_1 - f_0 \cdot g_1}{g_0}, \tag{B.17}$$
$$f_2 = \frac{F_2 - f_0 \cdot g_2 - f_1 \cdot g_1}{g_0}, \tag{B.18}$$
$$\cdots . \tag{B.19}$$

The error matrix of f, V_f, is given as:

$$V_f = A^{'} \cdot V_F \cdot A^{'T} + C \cdot V_g \cdot C^T, \tag{B.20}$$

where a matrix $A^{'}$ of which components are $A^{'}_{ij} = \partial f_i / \partial F_j$ can be calculated:

$$A^{'}_{ij} = \partial f_i / \partial F_j = \frac{1}{g_0} \left(\partial F_i / \partial F_j - \sum_{k=0}^{i=1} \partial f_k / \partial F_j \cdot g_{i-k} \right), \tag{B.21}$$

$$= \frac{1}{g_0} \left(\delta_{i,j} - \sum_{k=0}^{i=1} \partial f_k / \partial F_j \cdot g_{i-k} \right), \tag{B.22}$$

and a matrix C of which components are $C_{ij} = \partial f_i / \partial g_j$ can be calculated:

$$C_{ij} = \partial f_i / \partial g_j, \tag{B.23}$$

$$= \frac{1}{g_0} \left(- \sum_{k=0}^{i=1} (\partial f_k / \partial g_j \cdot g_{i-k} + f_k \cdot \partial g_{i-k} / \partial g_j) - f_i \cdot \partial g_0 / \partial g_j \right) \tag{B.24}$$

$$= -\frac{1}{g_0} \left(\sum_{k=0}^{i=1} \partial f_k / \partial g_j \cdot g_{i-k} + f_{i-j} \cdot (1 - \delta_{0,j}) + f_i \cdot \delta_{0,j} \right). \tag{B.25}$$

B.3 Convolution of same functions

The convolution of two same function f is F as shown following:

$$F_k \equiv (f \circ f)_k = \sum_{k'=0}^{k} f_{k'} \cdot f_{k-k'}, \tag{B.26}$$

$$F_0 = f_0 \cdot f_0, \tag{B.27}$$

$$F_1 = f_0 \cdot f_1 + f_1 \cdot f_0, \tag{B.28}$$

$$F_2 = f_0 \cdot f_2 + f_1 \cdot f_1 + f_2 \cdot f_0, \tag{B.29}$$

$$\cdots . \tag{B.30}$$

The error matrix of F, V_F is given with a covariance matrix of f, V_f, as following:

$$U_F = A \cdot V_f \cdot A^T, \tag{B.31}$$

where a matrix A is defined as:

$$\begin{aligned} A_{ij} &= \partial F_i / \partial f_j & \text{(B.32)} \\ &= \sum_{k=0}^{i} (\partial f_k / \partial f_j \cdot f_{i-k} + f_k \cdot \partial f_{i-k} / \partial f_j) & \text{(B.33)} \\ &= \sum_{k=0}^{i} (\delta_{k,j} \cdot f_{i-k} + f_k \cdot \delta_{i-k,j}) & \text{(B.34)} \\ &= 2 \cdot f_{i-j} & \text{(B.35)} \end{aligned}$$

B.4 Deconvolution of same functions

The deconvolution of f from $F = f \circ f$ is defined as:

$$\begin{aligned} f_k &\equiv (F \circ^{-1} f)_k, & \text{(B.36)} \\ f_0 &= \sqrt{F_0}, & \text{(B.37)} \\ f_1 &= \frac{F_1}{2 \cdot f_0}, & \text{(B.38)} \\ f_2 &= \frac{F_2 - f_1 \cdot f_1}{2 \cdot f_0}, & \text{(B.39)} \\ &\cdots . & \text{(B.40)} \end{aligned}$$

Generalization looks like:

$$\begin{cases} k = 0, & f_0 = \sqrt{F_0}, \\ k > 0, & f_k = \frac{F_k - \sum_{k'=1}^{k-1} f'_k \cdot f_{k-k'}}{2 \cdot f_0}. \end{cases} \tag{B.41}$$

The error matrix of f, V_f, is given as:

$$V_f = A^{'} \cdot V_F \cdot A^{'T}, \tag{B.42}$$

while a matrix $A^{'}$ is defined as:

$$A^{'}_{ij} = \frac{1}{2f_0}\left(\delta_{i,j} - \sum_{k=1}^{i-1}(\partial f_k/\partial F_j \cdot f_{i-k} + f_k \cdot \partial f_{i-k}/\partial F_j) - 2 \cdot f_i \cdot \partial f_0/\partial F_j\right) \tag{B.43}$$

Appendix C

Study of EMC Performance Using $e^+e^- \to \gamma\gamma$ events

We present a study of the performance of the *BABAR* Electromagnetic Calorimeter (EMC) using photons from $e^+e^- \to \gamma\gamma$ events which have energies between 3.1 GeV and 9.0 GeV. Kinematic constraints between the two detected photons permit checks of the EMC calibration, resolution and geometry. Our results indicate that photon energies are being reconstructed systematically 1.2 ± 0.3 % higher than what is predicted by kinematics. The energy resolution of photons in upper energy range of this sample (mean energy 7.8 GeV, which are observed at relatively smaller polar angles θ with respect to the electron beam direction), is found to be 1.6 ± 0.3 %. Photons in the lower energy range (mean energy 4.1 GeV, observed at larger θ), have energy resolutions measured to be 2.1 ± 0.3 %. Azimuthal angles are measured with systematic errors less than 1 mrad and the azimuthal angle resolution is determined to be 2.7 mrad for photons of mean energy 6.0 GeV. Systematic errors in the measurement of polar angles are observed at the 1 mrad level, arising from shower reconstruction algorithms used in event reconstruction; the polar angle measurement resolution is consistent with that found for measuring azimuthal angles, but is difficult to determine with the method used here. We find the

origin of the EMC shifted by -0.189 ± 0.006 cm in x and 0.054 ± 0.005 cm in y with respect to the drift chamber.

C.1 Introduction

At e^+e^- colliders, the two-body processes $e^+e^- \to e^+e^-$, $\mu^+\mu^-$ and $\gamma\gamma$ provide clean sources of charged and neutral particles with large and well-known cross sections. At *BABAR* (center of mass energy 10.58 GeV), the corresponding detected cross sections (within the lab-frame polar angle acceptance, $15.8^o \sim 141.8^o$) are $\sim$ 40 nb, 1.16 nb and 2 nb, respectively. The respective differential cross sections for these processes are shown in Fig. C.1.

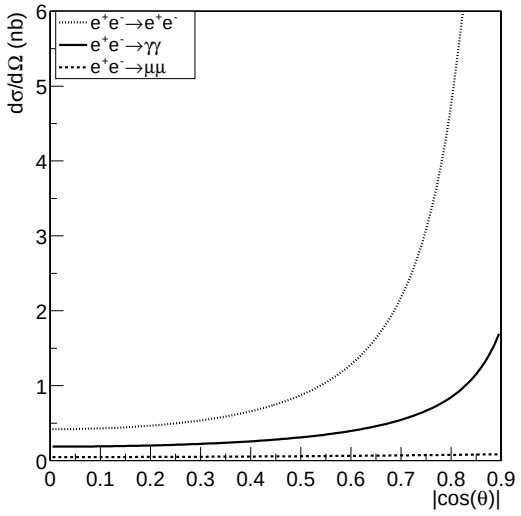

Figure C.1: Differential cross sections for $e^+e^- \to e^+e^-$, $\mu^+\mu^-$ and $\gamma\gamma$

By energy-momentum conservation, final state particles are mono-energetic

and collinear in the center of mass (CM) frame. Consequently, two-body processes are often used in detector monitoring, calibration and performance studies. Bhabha events ($e^+e^- \to e^+e^-$), for example, are used to calibrate the high energy scale of the *BABAR* electromagnetic calorimeter (EMC). In this study, we use $e^+e^- \to \gamma\gamma$ events to verify the Bhabha calibration. In addition, we measure the energy resolution and study the reconstruction of photon directions. The basic method is described next.

Two-body kinematics enables us to predict the lab energy of photons, $E_{\rm pred}$, in terms of their measured polar angle. The predicted lab-frame photon energy as a function of its CM frame polar angle, θ^*, is given by the following:

$$E_{\rm pred}(\theta^*) \equiv \frac{E_{\rm CM}}{2}\gamma(1+\beta\cos\theta^*), \tag{C.1}$$

where E_{CM} is the CM energy, β is the velocity of the CM system in units of speed of light and γ is $1/\sqrt{1-\beta^2}$. We define the relative energy difference between measured and predicted photon energies in the lab frame by the following:

$$\frac{\delta E}{E} \equiv \frac{E_{\rm meas} - E_{\rm pred}}{E_{\rm pred}}, \tag{C.2}$$

where $E_{\rm meas}$ is the measured photon energy. The mean of $\delta E/E$ is used to check energy calibration; its full width half max is a measure of the EMC energy resolution.

Similarly, the direction of one particle in the final state, $\vec{n}_1^{\rm pred}$, can be predicted if the energy-momentum 4-vector of the other particle, (E_2, $\vec{p_2}$), is

known:

$$\vec{n}_1^{\,\mathrm{pred}} = \frac{2\gamma^2(E_2 - \vec{\beta}\cdot\vec{p}_2)\vec{\beta} - \vec{p}_2}{|2\gamma^2(E_2 - \vec{\beta}\cdot\vec{p}_2)\vec{\beta} - \vec{p}_2|}. \tag{C.3}$$

Notice that for $e^+e^- \to \gamma\gamma$ events, only direction vectors are needed to describe photon kinematics.

We can compare the direction measured for a given photon with that predicted by the other photon in the event in order to study possible errors in reconstructing photon directions. The lab-frame polar and azimuthal angle differences between measured and predicted photon directions are defined by:

$$\delta\theta = \arccos\left(\vec{n}_1 \cdot \hat{z}\right) - \arccos\left(\vec{n}_1^{\,\mathrm{pred}} \cdot \hat{z}\right), \tag{C.4}$$

$$\delta\phi = \arctan\left(\frac{\vec{n}_1 \cdot \hat{y}}{\vec{n}_1 \cdot \hat{x}}\right) - \arctan\left(\frac{\vec{n}_1^{\,\mathrm{pred}} \cdot \hat{y}}{\vec{n}_1^{\,\mathrm{pred}} \cdot \hat{x}}\right), \tag{C.5}$$

where $\hat{z} = \vec{\beta}/|\vec{\beta}|$, $\hat{y}$ points in the vertical direction, $\hat{x} = \hat{y} \times \hat{z}$ and $\vec{n_1}$ is the measured direction vector of the photon being considerated.

The photon momentum, $\vec{p_\gamma}$, is reconstructed using the cluster position in the EMC, $\vec{x}_{\mathrm{EMC}}$, an origin or vertex position assumed for photons, $\vec{x}_{\mathrm{o}}$, and the measured energy of the cluster E_γ:

$$\vec{p_\gamma} = E_\gamma \cdot \frac{\vec{x}_{\mathrm{EMC}} - \vec{x}_{\mathrm{o}}}{|\vec{x}_{\mathrm{EMC}} - \vec{x}_{\mathrm{o}}|}. \tag{C.6}$$

We use the mean event vertex location measured from Bhabha and $e^+e^- \to \mu\mu$ events for each run—called here the interaction point (IP)—as the event vertex for *all* 2-photon events because the actual event vertex cannot be determined. Typical values of the IP location, the RMS spread in event

Parameters		Typical value
IP position	x (cm)	0.1
	y (cm)	0.3
	z (cm)	-0.9
RMS in event vertex	x (μm)	110
	y (μm)	3.3
	z (μm)	7100
$\vec{\beta}$	x	-0.01
	y	-0.0002
	z	0.4857

Table C.1: The typical values of the IP position, IP RMS size and the boost vector.

vertices and the components of CM boost vector, all in the standard *BABAR* coordinate system, are collected in Table C.1.

C.2 The data samples and event selection

The data used in this analysis are the `good runs` [1] in the ranges of run number between 25281 and 25382 (about 3 million events); these events are reconstructed with the `13.0.1` release. About 1 million Monte Carlo events are generated and reconstructed with the `13.0.1` release.

The selection criteria for the 2-photon events used in the present analysis are given in the following:

- To obtain $e^+e^- \to \gamma\gamma$ events having a standard detection efficiency, we use events that passed the Level 3 trigger under the `L3TGammaGammaFilter`. It requires:
  - zero tracks satisfying:
    - $|d_0^{\rm IP}| < 1.5$ cm, $|d_0^{\rm IP}|$ is the distance of closest approach to the IP in the x-y plane,
    - $z_0 < 10.0$ cm, z_0 is z coordinate of a track's point of closest approach to z axis
    - $p_T > 0.25$ GeV/c, p_T is the transverse momentum.
  - one pair of high energy clusters satisfying $E^*_\gamma/(E_{\rm CM}/2) > 0.7$,
  - $|\theta^*_1 + \theta^*_2| < 0.5$ rad, θ^* is polar angle of a photon in the CM frame,
  - $|\phi^*_1 - \phi^*_2 + \pi| < 0.5$ rad, ϕ^* is azimuthal angle of a photon in the CM frame.

[1] http://www.slac.stanford.edu/BFROOT/www/Physics/BaBarData/BaBarData.html

- From the events passing the Level 3 criteria, we select photons starting with all the local maxima of calorimeter energy deposits called "bumps". Then the following cuts are applied:
  - the bumps should not be matched with any tracks,[2]
  - E $>$ 30 MeV,
  - LAT (lateral moment) $<$ 0.8,
- The bumps with these cuts are saved in the list called `GoodPhotonLoose`. In events where there are more than two bumps or photons, the two having the highest energies are selected. Then the following two cuts are applied:
  - the two photons must be approximately collinear in the CM frame by requiring $\arccos(\vec{n_1} \cdot \vec{n_2}) < 0.03$ rad, where $\vec{n}$ is the direction vector of each photon,
  - $\theta_{lab} < 0.375$ rad, because of the poor energy resolution as shown in Fig. C.2.

  The acolinearity cut is imposed in order to reject events with significant initial-state radiation (ISR).

[2]We take the points where tracks intersect with the EMC, then compare azimuthal and polar angles with those of bumps. Using a double Gaussian model, a significance level is calculated. The bumps which are not matched with any tracks are those of which significance level is smaller than 1×10^{-6}.

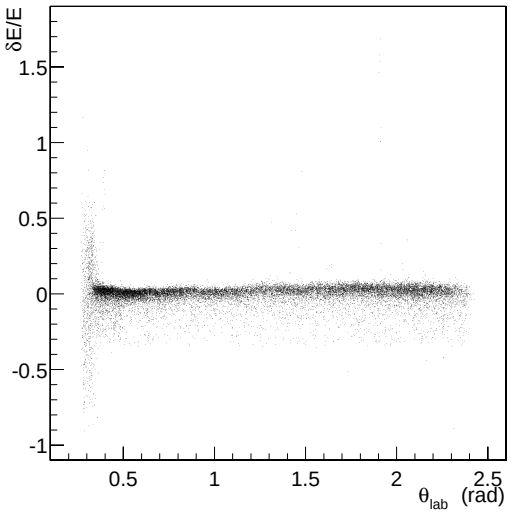

Figure C.2: The relative energy difference vs. θ_{lab}. The low theta (first three θ rings of crystals in the endcap area) region has poor energy resolution. This plot has only run 25281 and 25304, and $\delta E/E$ <2 is required so that the typical performance of most crystals outside the endcap region can be seen.

C.3 Angle errors and resolutions

In this section, the angle differences ($\delta\theta$ or $\delta\phi$) are studied as a function of polar angle θ and azimuthal angle ϕ. We do this for two basic reasons. First, systematic errors in angle measurements will affect the predicted photon energy and, hence, our understanding of the energy calibration. Second, angle measurements affect the measured *momentum* for photons, an important kinematic quantity. In the following, all angles are described in the lab frame.

C.3.1 Method

We represent the data in two dimensional histograms with one angle (θ or ϕ) as the horizontal axis and one angle difference ($\delta\theta$ or $\delta\phi$) as the vertical

axis. We fit the angle difference distribution for each bin with a Gaussian probability distribution function (pdf) and determine the corresponding mean and width. One example plot is shown in Fig. C.3. The mean and width of polar angle difference are called $\overline{\delta\theta}$ and $\sigma_{\Delta\theta}$, respectively. Those of azimuthal angle difference are called $\overline{\delta\phi}$ and $\sigma_{\Delta\phi}$, respectively. The relation between width and angular resolution is given by:

$$\sigma_\theta \equiv \sigma_{\Delta\theta}/\sqrt{2} \qquad \text{or} \qquad \sigma_\phi \equiv \sigma_{\Delta\phi}/\sqrt{2}. \tag{C.7}$$

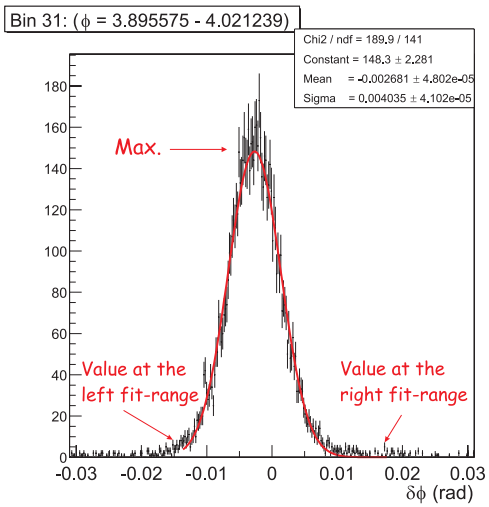

Figure C.3: One example (out of 50 such distributions) of azimuthal angle difference distribution with its Gaussian fit.

The fit-ranges are chosen to give the best χ^2/ndf under the condition that the fit-range ratio (the values of the fit function at the fit-ranges to the maximum value of it) to be less than 0.3. The fit-qualities of the angle difference distributions are summarized in Fig. C.21, in Section C.6.3.

C.3.2 Effects of misalignment on azimuthal angle distributions

If there is a misalignment of the EMC coordinate system relative to the nominal *BABAR* system, the true origin of the photons is shifted by $\Delta\vec{x}$ from the origin used in reconstruction, as shown in Fig. C.4. Therefore, the reconstruction of a photon's momentum should be corrected as in the following:

$$\vec{p}_\gamma = E_\gamma \cdot \frac{\vec{x}_{\rm EMC} - \vec{x}_{\rm o} - \Delta\vec{x}}{|\vec{x}_{\rm EMC} - \vec{x}_{\rm o} - \Delta\vec{x}|}, \tag{C.8}$$

where E_γ is the measured energy of the photon, $\vec{x}_{\rm EMC}$ is cluster position in the EMC and $\vec{x}_{\rm o}$ is origin of photons.

Photons produced parallel to $\Delta\vec{x}$ have no contribution from the misalignment; those perpendicular to $\Delta\vec{x}$ have maximum error. The mean of azimuthal angle difference is a sin function of ϕ, as shown in Fig. C.6.

$$\overline{\delta\phi} = A \cdot \sin(\phi + \phi_0), \tag{C.9}$$

$$\Delta\vec{x}_\gamma = (\Delta x_\gamma, \Delta y_\gamma) = A \cdot \frac{r_\gamma}{2} \cdot (\cos\phi_0, \sin\phi_0), \tag{C.10}$$

where A is a magnitude of the sin wave, ϕ_0 is a phase and r_γ is the distance from the IP to the EMC in the x-y plane of each photon.

The parameters A and ϕ_0 are extracted by fitting the mean of azimuthal angle difference as a function of ϕ for each run. Then, we take events in which both photons are detected in barrel region ($\theta_{lab} > 0.051$ for both photons), and calculate r_γ for each photon. Using these values and Eq. C.10, the misalignment $\Delta\vec{x}_\gamma$ is calculated for each per photon; the resulting distribution is shown in Fig. C.5. These data indicate there are probably two classes of

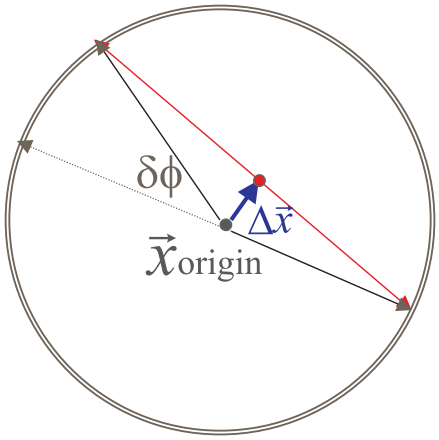

Figure C.4: Schematic diagram showing the effect of a misalignment, $\Delta\vec{x}$, between the DCH and the EMC for photon momentum reconstruction. The circle represents the EMC in the x-y plane. The red arrows are the true photon directions and the black arrows are the reconstructed photon directions using $\vec{x}_{\rm o}$.

runs with slightly different relative EMC-DCH alignments. In what follows, we assume a single misalignment for the entire data set given by the mean values indicated in Fig. C.5. The mean shift is:

$$\overline{\Delta\vec{x}_\gamma} \cong (-0.189 \pm 0.006,\, 0.054 \pm 0.005)\ \text{cm}. \tag{C.11}$$

To check this relative alignment hypothesis, we correct the photon directions by the mean EMC-DCH offset and re-evaluate the azimuthal differences. The blue points in Fig. C.6 are from reconstructing photon momenta assuming their origin is at the IP; black markers are following correction of the IP by $\overline{\Delta\vec{x}_\gamma}$, using Eq. C.8. Monte Carlo generated events, which use the IP as photons' origin, give the red markers. Both black and red curves show small remaining waves. A possible reason for this is a residual rotation of the EMC

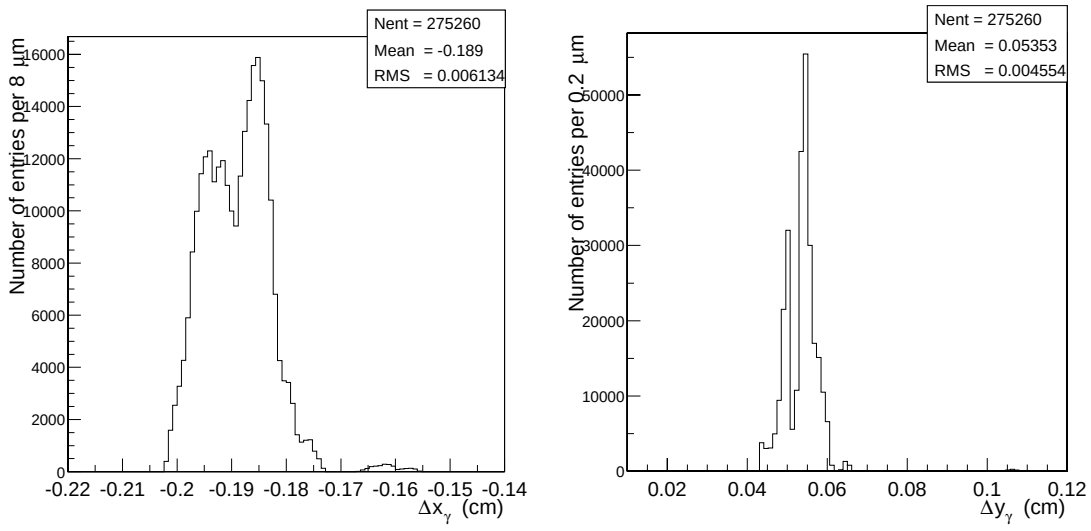

(a) (b)

Figure C.5: (a) The misalignment between the DCH and the EMC in x direction. (b) The same in y direction.

with respect to the DCH. We have not attempted to determine the parameters of such a rotation.

The mean of azimuthal angle difference as a function of polar angle is shown in Fig. C.7. Note that there are correlations between different values of θ in this kind of plot: when a photon falls in the endcap area (low θ), the other photon in the final state has a large value for θ. Therefore, the distribution is symmetric about $\pi/2$ in the CM frame, but with opposite sign. In addition, there is an asymmetry that arises from the $\theta_{\rm lab} < 0.375$ rad cut.

After corrections, the net azimuthal reconstruction error is less than 1 mrad over the full EMC acceptance.

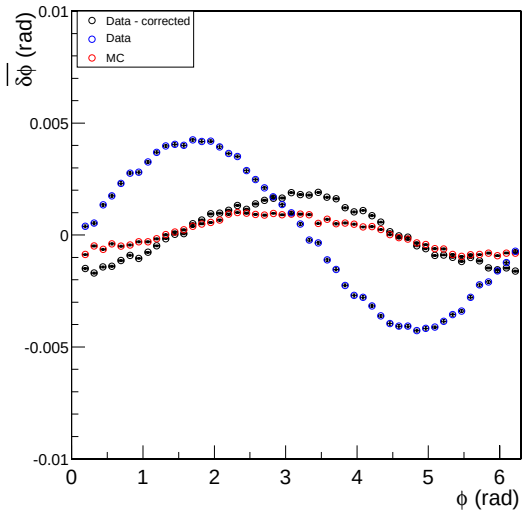

Figure C.6: The mean of azimuthal angle difference as a function of azimuthal angle. Blue markers are the data, using the normal IP in reconstruction. The black markers are after applying the misalignment correction. Red markers are for Monte Carlo simulated events.

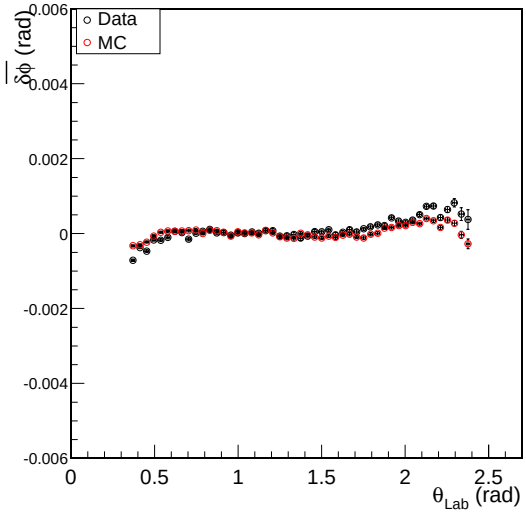

Figure C.7: The mean of azimuthal angle difference as a function of polar angle.

C.3.3 Polar angle

In the same way we analyzed the azimuthal distribution, the mean of the polar angle difference as a function of θ is shown in Fig. C.8. It shows a complex structure which comes about from systematic errors in reconstructing both "ends" of photon direction vectors: the origin and the cluster position. Systematic error in the z direction of the event will affect the mean of the polar angle difference distribution. Data show that the misalignment in z direction is small. Cluster position reconstruction issues and the basis for the "prediction"—black curve—are explained in Section C.6.1. The prediction indicated in Fig. C.8 is based on true cluster position at a fixed depth 16 cm in crystals, while 12.5 cm was used in the reconstruction code. Notice that Monte Carlo simulated events disagree with data and with the prediction. The Monte Carlo distribution shows the same structure as our prediction made for cluster position on the EMC crystal surface as shown in Fig. C.19 in Section C.6.2. The reason for this is not fully understood yet, but this result suggests inconsistencies in reconstructing Monte Carlo events compared to actual data. But we have found no obvious error in reconstruction code.

For reasons described above, polar angle correlations between the two photons lead to correlations in the structures seen in Fig. C.8. With a realistic model of shower depth, it is plausible that systematic errors in polar angle can be maintained below the 1 mrad level. However, the Monte Carlo events/data differences indicated here must be understood before we can have full confidence in the polar angle reconstruction.

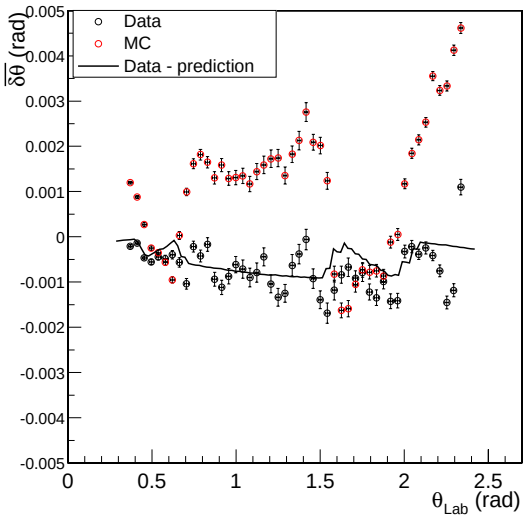

Figure C.8: The mean of polar angle difference as a function of polar angle.

C.3.4 Angular resolution

Angular resolutions are shown in Fig. C.9. The azimuthal angle resolution, 2.7 mrad, is extracted from a constant fit to data. The polar angle resolution peaks near 90 degrees because of the effect of the spread in longitudinal positions of the true event locations, which cannot be reconstructed on an event-by-event basis. To verify this, we take Monte Carlo generator-level tracks—which are generated at one point—and smear them with a Gaussian distribution function of mean 0 and width 0.79 cm in the z direction. After smearing, the shape of the data points (black and red markers in Fig. C.9(b)) is well reproduced. Because this effect of spread in event vertices is large compared to the expected polar angle resolution, it is not possible to extract a meaningful value for polar angle resolution; we expect it is consistent with

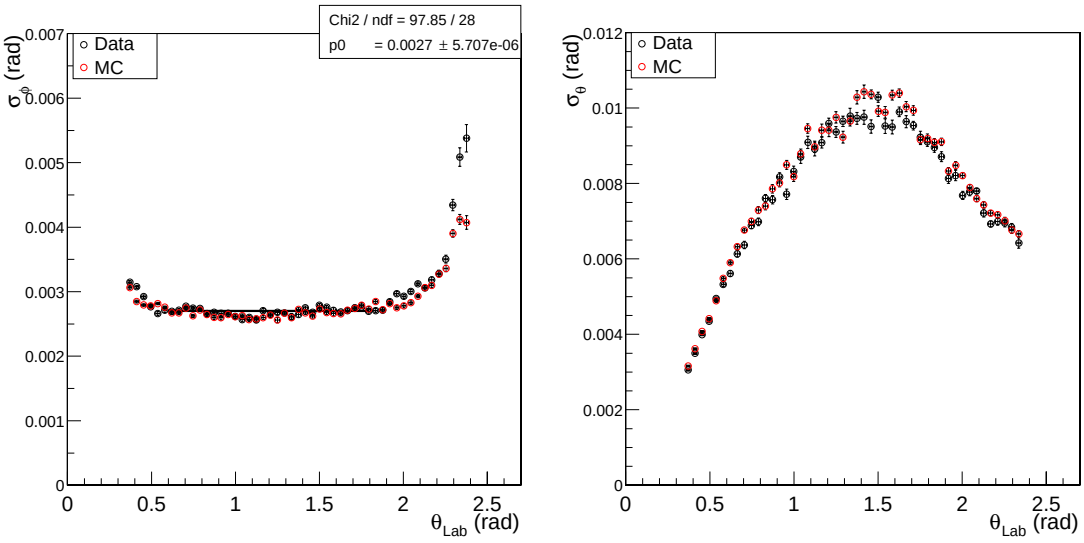

(a) (b)

Figure C.9: (a) Azimuthal angle resolution as a function of polar angle and its constant fit. (b) Polar angle resolution as a function of polar angle.

EMC crystal sizes and typical shower sizes as is the azimuthal resolution.

C.4 Energy bias and resolution

Because of two-body kinematics, it is possible to predict the energy of a photon from its measured polar angle. Our study of the relative energy difference between measured and predicted photon energies, $\delta E/E$, as a function of polar angle is described in this section.

C.4.1 Method

Again, we present data in two dimensional histograms with θ as horizontal axis and $\delta E/E$ as vertical axis. We fit $\delta E/E$ distribution for each bin with the so-called "Crystal Ball" function,

$$C(x) = \begin{cases} Ne^{-\frac{(x-x_0)^2}{2\sigma^2}} & \text{for } x > x_0 - \alpha\sigma, \\ N\frac{(n/\alpha)^n e^{-\frac{\alpha^2}{2}}}{[(x_0-x)/\sigma+n/\alpha-\alpha]^n} & \text{for } x \leq x_0 - \alpha\sigma, \end{cases} \tag{C.12}$$

with five free parameters (peak height N, peak position x_0, width σ, joint parameter α and power n). One example plot is shown in Fig. C.10. The mean of each fit is called $\overline{\delta E}/E$ and relative energy resolution, σ_E/E, is full width half max divided by 2.354.

We find that the Crystal Ball function doesn't completely describe the full fit-range properly. Therefore, care must be taken in order to find the best fit-ranges to describe the peak fit and to determine the resolution most reliably. The fit-ranges are chosen to give the best χ^2/ndf under the condition that the fit-range ratio (the values of the fit function at the fit-ranges to the maximum value of it) are less than 0.3. The fit-qualities of the relative energy difference distributions are summarized in Fig. C.22, in Section C.6.3.

C.4.2 Energy calibration bias and resolution

The mean of relative energy difference $\overline{\delta E}/E$, and relative energy resolution, σ_E/E, are shown in Fig. C.11. A constant fit to $\overline{\delta E}/E$ gives 0.84 % for data and -0.37 % for Monte Carlo events. A reasons for a negative value in the Monte Carlo distribution could be the use of an electron shower model in the acceptance correction for photons. The systematic difference between data and Monte Carlo events is 1.2 %. This difference is possibly due to the miscalibration of high energy photons. Furthermore, the energy resolution shows a step around $\theta \sim 1.2$ rad. A possible reason for the step is that different types of amplifiers are employed in the EMC at different polar-angle regions and crystal depths. A value for the energy resolution is fitted separately for each region in polar angle. The resulting energy resolution is 1.6 % at low θ and 2.1 % elsewhere.

C.4.3 Systematic errors

Two different possible sources of systematic errors have been studied. One is the resolution of the predicted energy. The other is the effect of errors in the measured polar angle which arise from the longitudinal distribution of beam vertices. We find both potential sources to be small.

C.4.3.1 Resolution of the predicted energy

To test that the resolution of the predicted energy is negligible compared to that of the measured energy, the energy of a photon from the generator

level Monte Carlo, we compute the difference between the generated energy, $E_{\rm gen}$, and the predicted energy, $E_{\rm pred}$. The relative energy difference between predicted and generated energies, $(E_{\rm gen} - E_{\rm pred})/E_{\rm gen}$, is plotted for the full θ range in Fig. C.12. A Crystal Ball function fit gives 0.3 % for resolution of the predicted energy; the systematic error of the measured energy.

C.4.3.2 Resolution of the polar angle

The unknown longitudinal vertex position distribution is the dominant contribution to the resolution of the polar angle. We can eliminate this contribution and estimate the systematic error in the predicted energy due to the polar angle measurement error, by choosing the vertex position for each event that makes the two photons back-to-back in the CM frame, instead of using the IP which is an average for each run. A histogram of the difference between the nominal longitudinal position and the position that forces the photons to be back-to-back, Δz, is shown in Fig. C.13. The RMS of Δz, 0.79 cm, is close to that measured for vertices in events with charged tracks, 0.71 cm, which arise from the longitudinal extents of the colliding beams.

Because photons are forced to be back-to-back in this analysis, we need only one polar angle $\theta^*_{\rm event}$ to describe the event. We calculate a test predicted energy, $E^{\rm test}_{\rm pred}$, with $\theta^*_{\rm event}$, and a test variable $(\delta E/E)_{\rm test}$ according to:

$$E^{\rm test}_{\rm pred} \equiv \frac{E_{\rm CM}}{2}\gamma(1+\beta\cos\theta^*_{\rm event}), \tag{C.13}$$

$$\left(\frac{\delta E}{E}\right)_{\rm test} \equiv \frac{E_{\rm meas} - E^{\rm test}_{\rm pred}}{E^{\rm test}_{\rm pred}}. \tag{C.14}$$

The mean of relative energy difference and the energy resolution from this method are shown in Fig. C.14. These agree with our results where the nominal IP was used for all event vertices.

The difference of $\delta E/E$ and of energy resolution between the "default" method and the "forced-back-to-back test" method is histogramed in Fig. C.15. The RMS gives the systematic error of $\overline{\delta E}/E$, 0.2 %, and of the energy resolution, 0.1 %.

The combined systematic error is 0.3 % for relative energy difference and 0.3 % for energy resolution.

C.4.4 Result: energy calibration bias and resolution

As a summary, photon energies are reconstructed systematically 1.2 ± 0.3 % higher than what is predicted by kinematics. The energy resolution is 1.6 ± 0.3 % for smaller polar angles and 2.1 ± 0.3 % for larger polar angles.

Our results for the EMC energy resolution (black markers in Fig. C.11(b)) is overlaid with energy resolutions from other analyses, as shown in Fig. C.16. We find the energy resolution of high energy photons to be the same or better than that determined using Bhabha events.

C.5 Summary

The means and resolutions, of angle differences and of relative energy difference, are studied using $e^+e^- \to \gamma\gamma$ events. The mean of the azimuthal

angle difference distribution shows the importance of using the correct origin for reconstructing photon momenta. It also indicates a misalignment between the DCH and the EMC: -0.189 ± 0.006 cm in x, 0.054 ± 0.005 cm in y. Systematic errors in azimuthal reconstruction are less than about 1 mrad and the ϕ resolution is 2.7 mrad. The mean polar angle difference distribution is strongly affected by the cluster position reconstruction algorithm. The θ resolution distribution is dominated by the spread of the interaction point in the z direction. The longitudinal distribution of event vertices can be measured by forcing the photons to be back-to-back in the CM frame. The resulting longitudinal distribution agrees with vertex distributions in events with charged tracks where the event location can be measured directly.

High energy photons appear to be miscalibrated by 1.2 %. The energy resolution derived from $e^+e^- \to \gamma\gamma$ events is 1.6 % at low θ and 2.1 % elsewhere. This is approximately the same as or better than the energy resolution measured with Bhabha events.

C.6 Appendix

C.6.1 Cluster position reconstruction and prediction

A typical electromagnetic shower spreads over many adjacent crystals, forming a cluster of energy deposits.

In release-10, the position of these energy deposits are assumed to be at the center of the front face of the crystals. From the polar and azimuthal angles of these positions, the angles of the cluster position is calculated using

a center-of-gravity method with logarithmic weights. The cluster position is defined as the intersection of the front face of the crystals with a line from the origin in the direction given by the cluster angles.

A systematic bias of the calculated polar angle originates from the non-projectivity of the crystals. This bias is corrected by a simple offset of -2.6 mrad for $\theta > 90^\circ$ and $+2.6$ mrad for $\theta < 90^\circ$. This correction δ_{R10} is calculated by the following equation:

$$\delta_{\mathrm{R10}} = \frac{0.0026 \cdot (1 - \exp(-61 \cdot \cos\theta))}{1 + \exp(-61 \cdot \cos\theta)}, \tag{C.15}$$

as shown in Fig. C.17 (black line).

The maximum longitudinal shower development of a 6 GeV photon-induced cascade in the EMC is about 12.5 cm. To take this depth into account, we move the position of the energy deposit $\vec{x}_{\mathrm{f}}$ toward the middle of the crystals by the depth d along the crystal axis $\hat{n}_\alpha$, as shown in Fig. C.18. The vector of the new position $\vec{x}_{\mathrm{hit}}$ is given as following:

$$\vec{x}_{\mathrm{hit}} = \vec{x}_{\mathrm{f}} + d \cdot \hat{n}_\alpha - \vec{x}_{\mathrm{IP}}, \tag{C.16}$$

where $\vec{x}_{\mathrm{IP}}$ is the vector to the IP from the origin. In the reconstruction code, the origin instead of the IP is used: $\vec{x}_{\mathrm{IP}} \equiv 0$. The polar angle difference δ is given as $\theta_{\mathrm{hit}} - \theta_{\mathrm{f}}$. Its predicted distribution from the EMC geometry is shown in Fig. C.17 (bluer marker).

Since the positions of the energy deposits are not saved in the dataset, we use the cluster positions instead of the energy deposit positions to predict

the systematic error of the angle difference in the $e^+e^- \to \gamma\gamma$ events. It is possible if we assume the errors of those are the same for all energy deposits in the cluster. The predicted angle difference made with the depth $d = 12.5$ cm and the longitudinal IP position $z_{\rm IP}$ (0 cm for data and 1.5 mm for Monte Carlo events) is overlayed in Fig. C.19. Monte Carlo distribution does not agree well with the prediction for reasons not understood yet. The fact that our prediction for Monte Carlo distribution with $z_{\rm IP} = 1.5$ cm agrees better might be a hint for a geometry problem in the EMC.

In the release-13 code, the shower depth $d = 12.5$ cm is used for the positions of the energy deposits. Thus the simple correction $\delta_{\rm R10}$ is removed. By this change, the gross distortions apparent under the release-10 code are largely eliminated.

We estimate the systematic error that would be associated with a different actual shower depth $d_{\rm true}$ and $z_{\rm IP}$. We overlay the systematic error estimated for $d_{\rm true} = 16$ cm in Fig. C.8. The magnitudes of remaining structure in the data, as well as some of the peaks and dips are approximately represented by the present estimate but there is additional structure in the data. The fact that the phase of the wiggle in the curve seems to agree with the data implies that the true depth of the photon hit in these crystals is somewhat greater than that assumed by the reconstruction algorithm.

C.6.2 Analysis with Release-10

The same analysis with data and Monte Carlo events as describe in the main text has been done with release-10 reconstruction code. We present only the results which show difference.

Mean of polar angle difference as a function of polar angle are discussed in Appendix C.6.1. Mean of relative energy difference and the energy resolution are shown in Fig. C.20. These results show impact of the improvements made to the cluster position reconstruction that have been first implemented in release-13.

C.6.3 Fit qualities

The quality of Gaussian fit to the azimuthal angle and Crystal Ball function fit to the relative energy difference are shown in Fig. C.21 and in Fig. C.22.

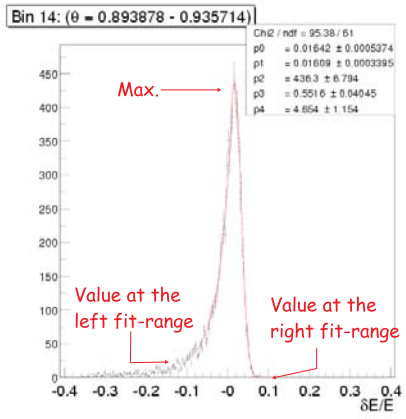

Figure C.10: One example (out of 50 such distributions) of relative energy difference distribution with its Crystal Ball function fit.

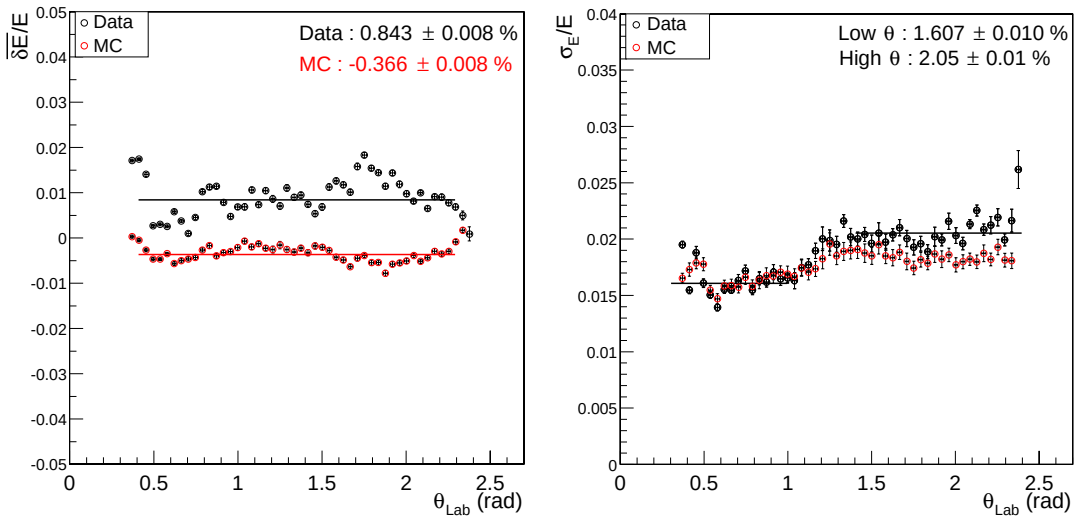

(a) (b)

Figure C.11: (a) The mean of relative energy difference as a function of polar angle and their constant fits. (b) Relative energy resolution as a function of polar angle and their constant fits.

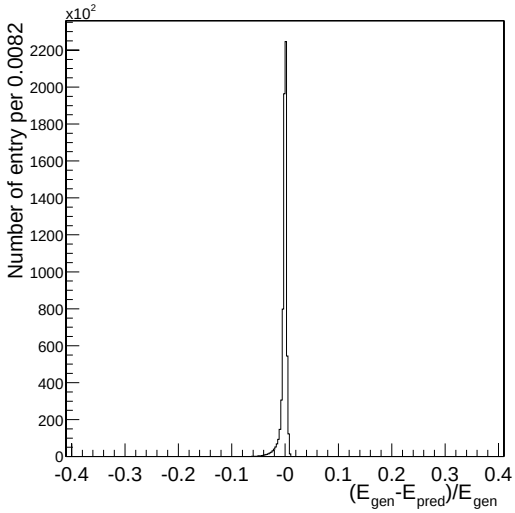

Figure C.12: The relative energy difference between predicted and generated energies.

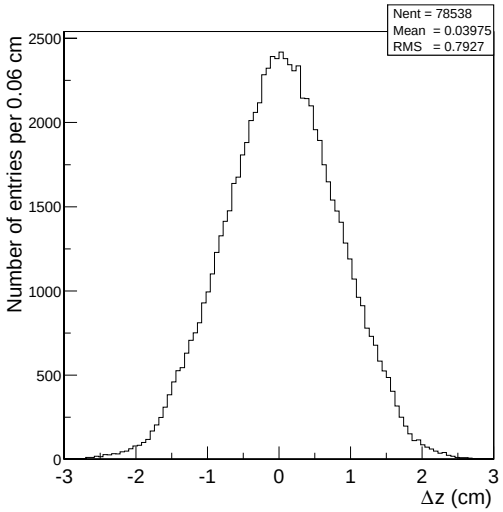

Figure C.13: Distance between event vertex and the IP. The RMS size is close to the RMS size of event vertices in z direction.

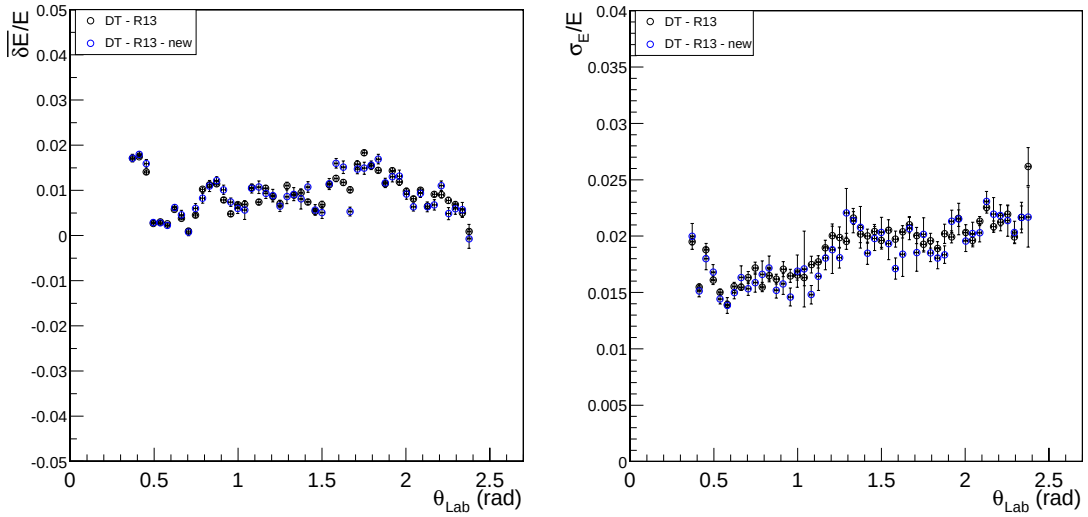

(a) (b)

Figure C.14: (a) The mean relative energy difference. (b) Relative energy resolution. The black markers are from Fig. C.11 and the blue markers with the "forced-back-to-back test" method.

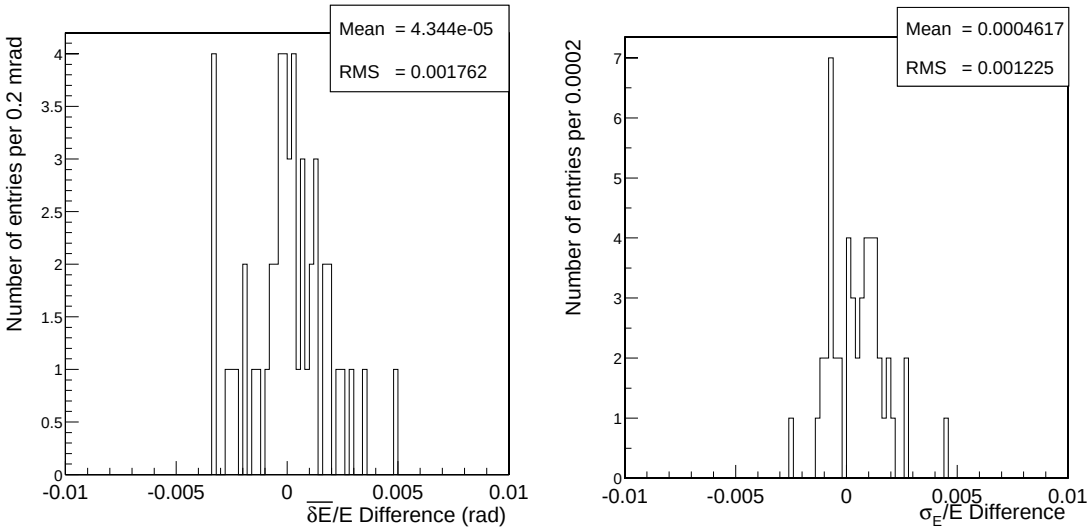

(a) (b)

Figure C.15: (a) The difference of mean relative energy differencefrom two methods. (b) The difference of relative energy resolution from two methods.

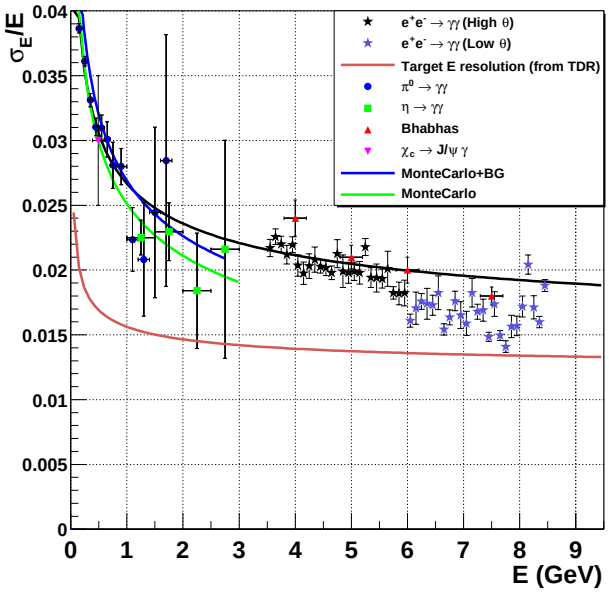

Figure C.16: Relative energy resolution with that from other analyses.

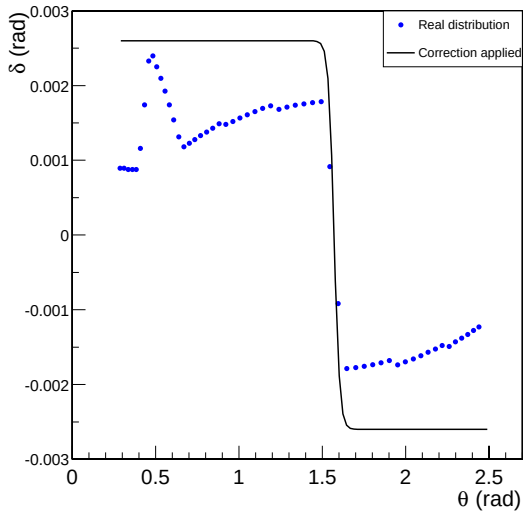

Figure C.17: The error on θ angle, from the cluster position reconstruction using digi positions at the front face of crystals (release-10). The blue markers are the calculated real distribution of the error, the black line is the correction applied.

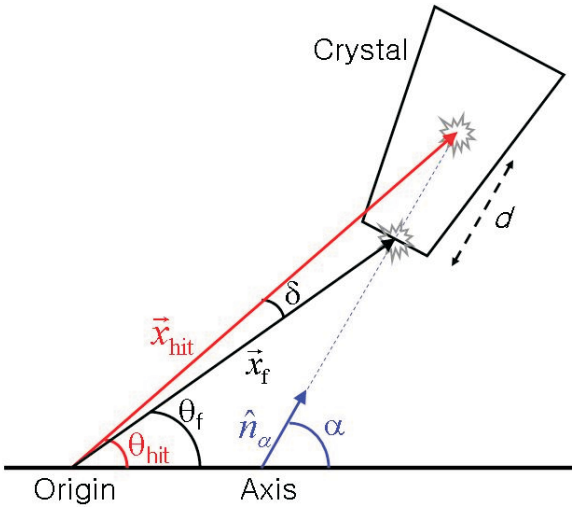

Figure C.18: The position of the energy deposit and non projectivity. $\vec{x}_f$ is the position of the energy deposit on the front face of the crystal and $\vec{x}_{hit}$ is that moved into the crystal with a depth d along the crystal axis. θ_f and θ_{hit} are according polar angles. $\hat{n}_\alpha$ is the unit vector in the crystal axis direction. This drawing is not to scale.

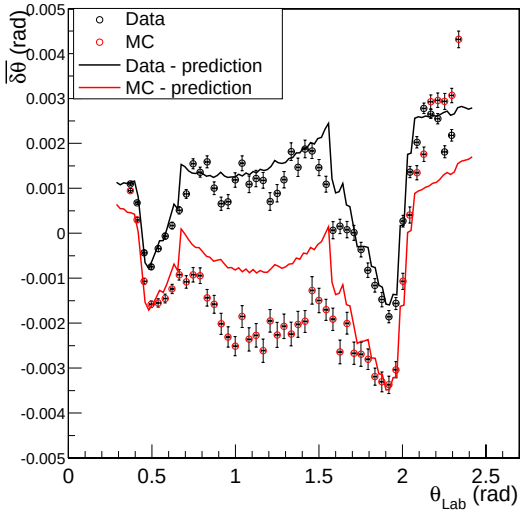

Figure C.19: M

ean of polar angle difference as a function of polar angle and its prediction.][Release-10] Mean of polar angle difference as a function of polar angle and its prediction. The prediction for data uses no shift in the IP in the z axis and that for the Monte Carlo events uses 1.5 mm shift.

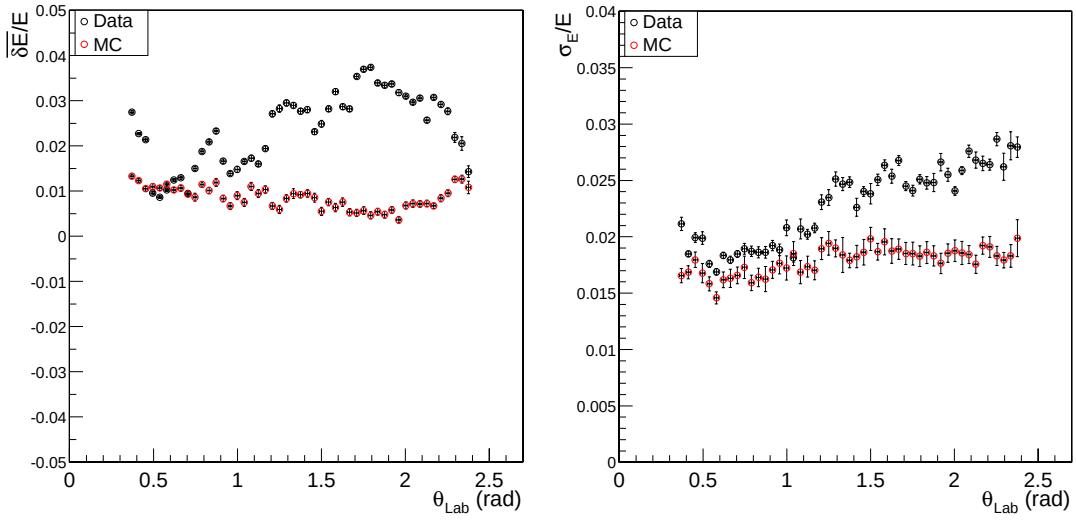

Figure C.20: [Release-10] (a) Mean of relative energy difference. (b) Relative Energy resolution as a function of polar angle.

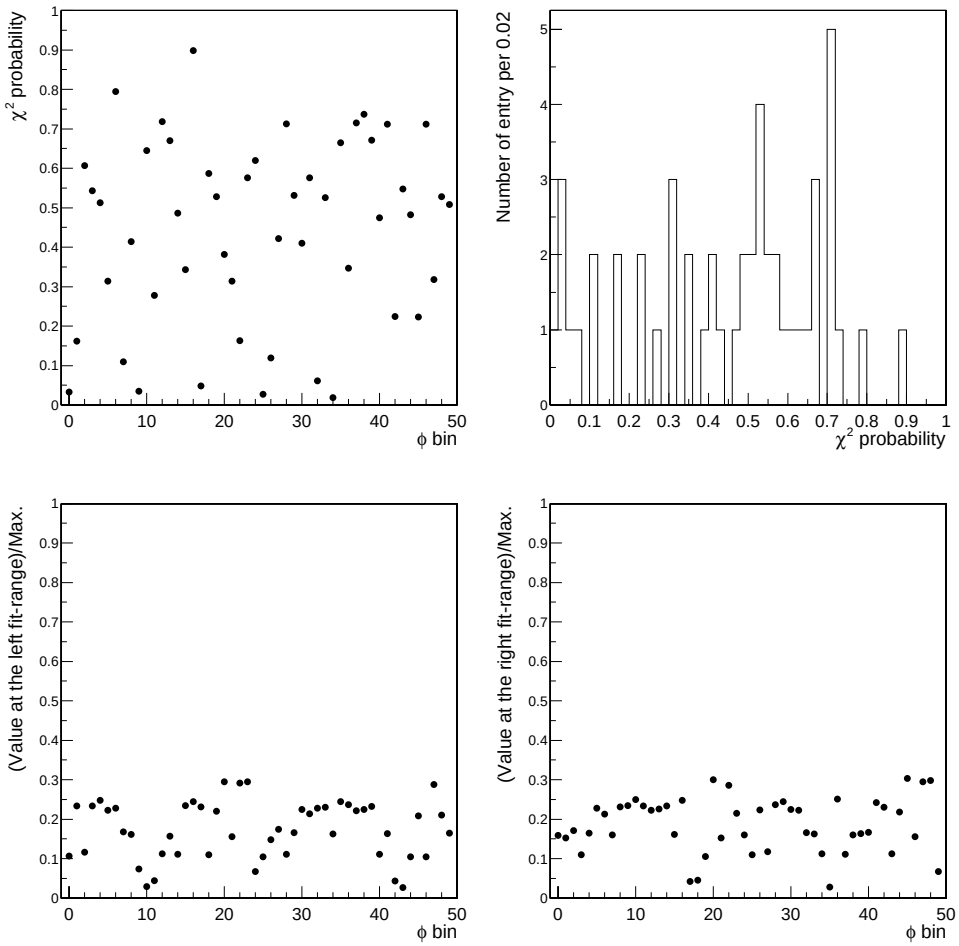

Figure C.21: The quality of the angle difference fit as a function of ϕ. The top left is the χ^2 probability vs. ϕ bin, the top right is the χ^2 probability histogram. The bottom left is the ratio (fit function value at the left fit-range)/(maximum value of the fit function), the bottom right is the same for the right fit-range. Notice this ratio is always smaller than 0.3.

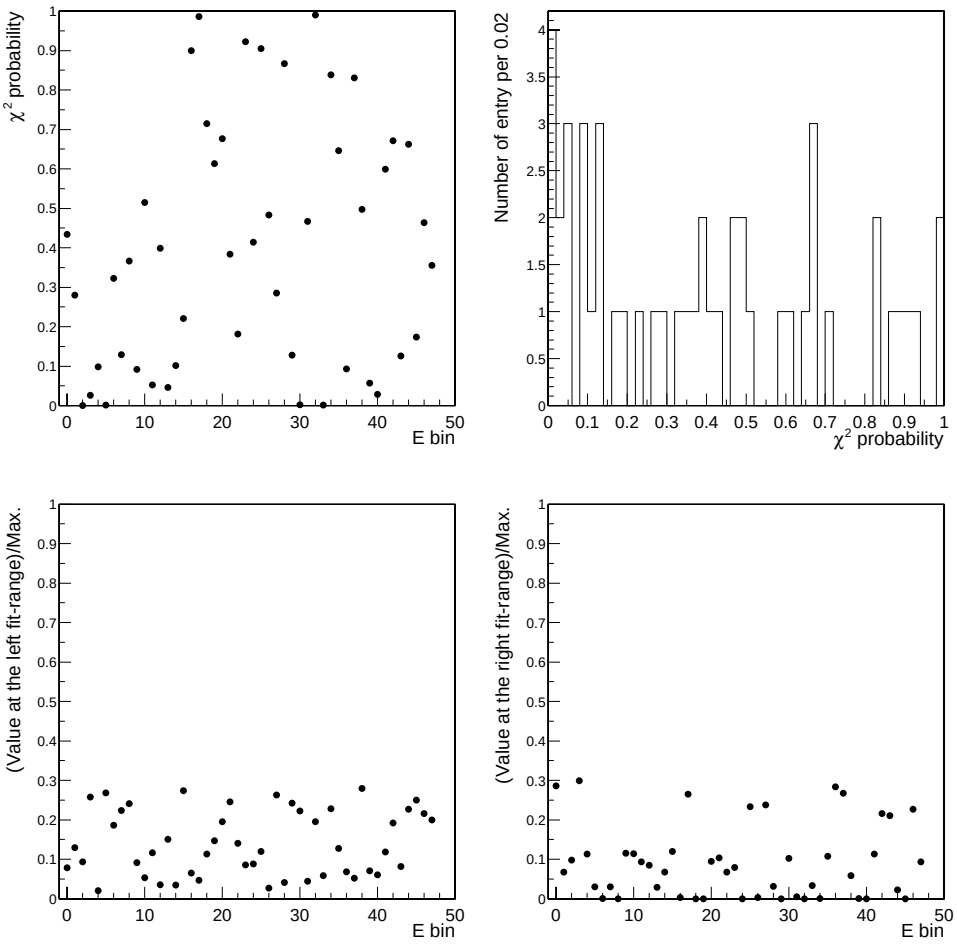

Figure C.22: The quality of relative energy difference fit as a function of θ. The top left is the χ^2 probability as a function of E bin, the top right is the χ^2 probability histogram. The bottom left is the ratio (fit function value at the left fit-range)/(maximum value of the fit function), the bottom right is the same for the right fit-range. The ratio is smaller than 0.3 at all times.

Bibliography

[1] N. Cabibbo. *Phys. Rev. Lett.*, 10:531, 1963.

[2] M. Neubert. Subleading shape functions and the determination of V_{ub}. *hep-ex/0207002*.

[3] A. Bornheim and et al. [The CLEO Collaboration]. *Phys. Rev. Lett.*, 88:231803, 2002.

[4] D. H. Perkins. *Introduction to High Energy Physics*. Cambridge University Press, New York, 2000.

[5] S. L. Glashow. *Nucl. Phys.*, 22:579, 1961.

[6] S.L. Glashow, J. Iliopoulos, and L. Maiani. *Phys. Rev. D*, 2:1285, 1970.

[7] J.H. Christenson and et al. *Phys. Rev. Lett.*, 13:138, 1964.

[8] L. Wolfenstein. *Phys. Rev. Lett.*, 51:1945, 1983.

[9] H. Leutwyler and M. Roos. *Z. Phys. C*, 25:91, 1984.

[10] S. Eidelman and et al. [Particle Data Group]. *Phys. Rev. D*, 592:1, 2004.

[11] A. Bornheim and et al. [The CLEO Collaboration]. *Phys. Rev. Lett.*, 88:231803, 2002.

[12] B. Aubert and et al. [The *BABAR* Collaboration]. *hep-ex/0207081*.

[13] K. Abe and at al. [The Belle Collaboration]. *BELLE-CONF-0325*, 2003.

[14] C. Schwanda (for the Belle Collaboration). to appear in the "proceedings of the international europhysics conference on high energy physics–eps 2003", aachen, germany. 2003.

[15] B. Aubert and et al. [The *BABAR* Collaboration]. *hep-ex/0307062*.

[16] V. Berger, C.S. Kim, and R.J.N. Phillips. *Phys. Lett. B*, 251:629, 1990.

[17] B. Aubert and et al. [The *BABAR* Collaboration]. *hep-ex/0408075*.

[18] E.V. Shuryak. *Phys. Lett. B*, 93:134, 1980.

[19] J.E. Paschalis and G.J. Gounaris. *Nucl. Phys. B*, 222:473, 1983.

[20] E. Eichten and B. Hill. *Phys. Lett. B*, 234:511, 1990.

[21] H. Georgi. *Phys. Lett. B*, 240:447, 1990.

[22] M. Shifman. Quark-hadron duality. *UMN-TH-1920/00*, 2000.

[23] I.I. Bigi, N.G. Uraltsev, and A.I. Vainshtein. *Phys. Lett. B*, 293:430, 1992.

[24] B. Blok and M. Shifman. *Nucl. Phys. B*, 399:441, 1993.

[25] T. Mannel and M. Neubert. *Phys. Rev. D*, 50:2037, 1976.

[26] B. Aubert and et al. [The *BABAR* Collaboration]. *Phys. Rev. Lett.*, 93:11803, 2004.

[27] B. Aubert and et al. [The *BABAR* Collaboration]. Measurement of the inclusive electron spectrum in charmless semileptonic b decays near the kinematic endpoint and determination of V_{ub}. *hep-ex/0408075*.

[28] A.H. Hoang, Z. Ligeti, and A.V. Manohar. *Phys. Lett. D*, 59:74017, 1999.

[29] P. Oddone. In D. Stork, editor, *Proceedings of the UCLA Workshop: Linear Collider $B\overline{B}$ Factory Conceptual Design*, page 243. World Scientific, 1987.

[30] B. Aubert and et al. [The *BABAR* Collaboration]. The *BABAR* detector. *Nucl. Instr. Meth. A*, 479:1–116, 2002.

[31] B. Aubert and et al. [The *BABAR* Collaboration]. Technical design report. *SLAC-REP-372*, 1995.

[32] *BABAR Physics Book*. `http://www.slac.stanford.edu/pubs/slacreports/slac-r-504.html`.

[33] C. Bozzi and et al. [The *BABAR* SVT Collaboration]. The *BABAR* silicon vertex tracker. *Nucl. Instr. Meth. A*, 453:78–83, 2000.

[34] G. Sciolla and et al. [The *BABAR* Drift Chamber Collaboration]. The *BABAR* drift chamber. *Nucl. Instr. Meth. A*, 419:310–314, 1998.

[35] I. Adam and et al. [The *BABAR* DIRC Collaboration]. The dirc detector at *BABAR*. *Nucl. Instr. Meth. A*, 433:121–127, 1999.

[36] `http://www.slac.stanford.edu/BFROOT/www/Physics/Analysis/AWG/Luminosity`.

[37] R. Bartoldus and et al. Trigger and filter documentation for run1. *BABAR Analysis Document #194*, 2002.

[38] G. Fox and S. Wolfram. Observables for the analysis of event shapes in e^+e^- annihilation and other processes. *Phys. Rev. Lett.*, 41(23):1581, 1978.

[39] `http://www.slac.stanford.edu/~lange/EvtGen/`.

[40] *Nucl. Instr. Meth. A*, 506:250–303, 2003.

[41] N. Isgur, D. Scora, B. Grinstein, and M.B. Wise. *Phys. Rev. D*, 39:799, 1989.

[42] D. Scora and N. Isgur. *Phys. Rev. D*, 52:2783, 1995.

[43] I.I. Bigi, M. Shifman, and N.G. Uraltsev. *Ann. Rev. Nucl. Part. Sci.*, 47:591, 1997.

[44] J.L. Goity and W. Roberts. *Phys. Rev. D*, 51:3459, 1995.

[45] B. Aubert and et al. [The *BABAR* Collaboration]. *Phys. Rev. D*, 67:031101, 2003.

[46] G. Mancinelli and S. Spanier. Kaon selection at the *BABAR* experiment. *BABAR Analysis Document #116*, 2001.

[47] M. Bona and et al. Report of the tracking efficiency task force for 2001. *BABAR Analysis Document #321*, 2002.

[48] `http://www.slac.stanford.edu/BFROOT/www/Physics/Tools/Pid/PidOnMc/pidonmc%.html`.

[49] T. Brandt. *Electron Identification and Measurement of the Inclusive Semileptonic Branching Fraction of B mesons at the BABAR Experiment.* PhD thesis, Technical University Dresden, November 2001.

This document does not include the vita page from the original.